Available online at www.sciencedirect.com

ScienceDirect

Geochimica et Cosmochimica Acta 254 (2019) 192–230

Geochimica et Cosmochimica Acta

www.elsevier.com/locate/gca

Extended Deep Earth Water Model for predicting major element mantle metasomatism

Fang Huang *, Dimitri A. Sverjensky

Department of Earth & Planetary Sciences, Johns Hopkins University, 3400 North Charles Street, Baltimore, MD 21218, USA

Received 14 June 2018; accepted in revised form 21 March 2019; Available online 04 April 2019

Abstract

Fluids in the deep crust and upper mantle appear to have played roles in the long-term evolution of the subcratonic lithospheric mantle and the stabilities of the continents, in the geochemical cycles of the elements from subduction zones to Earth's surface environment, and in the formation of diamonds. Much evidence of the chemistry of deep fluids has accumulated from studies of fluid inclusions in diamonds and xenoliths. But the origins of the fluids and their behavior are still unclear. In part, this is due to the lack of a comprehensive theoretical model of aqueous, high-pressure fluids. Traditional models have used a C-O-H-type of model, which contains no major rock-forming elements or aqueous ions or metal-complexes.

In the present study, we use experimentally measured solubility data for multicomponent K-free eclogite, K-free peridotite and K-bearing peridotite rocks at upper mantle conditions from the literature to construct aqueous speciation solubility models that enabled calibration of the thermodynamic properties of ions and metal-complex species involving the elements Na, K, Mg, Ca, Fe, Al, Si, and C in an extended Deep Earth Water (DEW) model. New equilibrium constants were retrieved for the aqueous bisilicate anion, a silica trimer, silicate complexes of Ca, Fe, and Al, a silicate complex of Mg and bicarbonate, and formate complexes of Fe and Ca. The aqueous speciation and solubility model also took account of decreases in the activity of water and aqueous activity coefficients of neutral dissolved gases and included consideration of $H_2CO_3^0$. Based on the temperature and pressure dependences of the equilibrium constants, and supporting data covering a wide range of conditions, we then developed aqueous equation of state characterizations of the ions and metal-complex species. Overall, the results form a basis for modeling fluid-rock interactions under upper mantle conditions consistent with experimental solubility measurements.

Keywords: Thermodynamic modeling; Mantle metasomatism; Deep fluids; DEW model

1. INTRODUCTION

Melts and fluids in the upper mantle are the mobile phases that facilitate the deep Earth geochemical cycles of the elements and provide the physical link to Earth's surface environment (Dasgupta, 2013; Galvez et al., 2016). Of the two mobile phases, fluids are the more enigmatic: melts ultimately crystallize, with or without eruption, but fluids are only sampled directly in fluid inclusions (Frezzotti and Ferrando, 2015). The passage of fluids is indirectly recorded in isotopic, chemical, or mineralogical alteration. Both melts and fluids are thought to cause metasomatic changes in the upper mantle and it is from these changes that the relative contributions of the two are discussed in the literature (Carlson et al., 2005). At great enough depths in the upper mantle, the physical distinction between melts and fluids disappears (Kessel et al., 2005).

Mantle metasomatism refers to the general process whereby melts or fluids modify their environment in the mantle. It is thought to play an important role in the

* Corresponding author at: Rensselaer Polytechnic Institute, 110 8th St., Winslow Building, Troy, NY 12180, USA.
E-mail address: fanghuang007@gmail.com (F. Huang).

https://doi.org/10.1016/j.gca.2019.03.027
0016-7037/

modification and destruction of the oceanic mantle (Galvez et al., 2016; Keller et al., 2016; Weiss et al., 2016), the subcontinental lithospheric mantle (Padrón-Navarta et al., 2011; Wang et al., 2015, 2016; Weiss et al., 2016; Tumiati et al., 2017; Regier et al., 2018; Tiraboschi et al., 2018), the evolution of specific igneous rock suites (Menzies and Murthy, 1980; Pilet et al., 2008; Ammannati et al., 2016; Weiss et al., 2016), and the formation of diamonds (Stachel and Harris, 2008; Shirey et al., 2013; Pearson and Wittig, 2014; Sverjensky and Huang, 2015; Weiss et al., 2016; Garber et al., 2018). Though the relative ratio of primary and metasomatized lithospheric mantle rocks is not clear, it is very likely there is little primary rock left due to repeated metasomatic events over billions of years (O'Reilly and Griffin, 2013). Metasomatic events affecting the peridotitic environment fall into three categories: (1) modal metasomatism – involving the addition of non-primary mineral phases; (2) cryptic metasomatism – involving changes in the mineral compositions, especially trace elements, without introducing new mineral phases; and (3) stealth metasomatism – involving the addition of new mineral phases that are indistinguishable from normal peridotitic minerals (Harte, 1983; Andersen et al., 1984; Dawson, 1984; Gréau et al., 2011; O'Reilly and Griffin, 2013). The main proxies in rocks reflecting mantle metasomatism are the major and trace element compositions (Menzies and Hawkesworth, 1986; O'Reilly and Griffin, 1988; Simon et al., 2007) and the isotopic compositions (O'Reilly and Griffin, 1988; Li et al., 2016; Deng et al., 2017) in the mantle wall-rock usually brought up to the surface by magmas as xenoliths or xenocrysts.

Here we focus on fluids in the upper mantle. The most direct samples of metasomatic fluids are trapped as fluid inclusions in diamonds or other xenocrysts (Frezzotti et al., 2011; Weiss et al., 2015). The fluid compositions vary from saline, to silicic, and to carbonatitic (Tomlinson et al., 2006; Shirey et al., 2013), or they might be rich in CO_2 (Frezzotti and Ferrando, 2015; Li, 2017) or hydrocarbon species (Sverjensky et al., 2014b; Huang et al., 2017). Fluids migrate in the deep Earth via cracks in rocks or along grain boundaries (O'Reilly and Griffin, 2013). One major source of deep Earth fluids is thought to result from the breakdown of minerals in subducting slabs (Frost and McCammon, 2008; Weiss et al., 2015). However, the origins of deep fluids are poorly constrained. Furthermore, traditional models of fluid chemistry cannot directly model the potential role of fluids in mantle metasomatic processes such as those discussed above.

Traditional models of water-rich fluids in the upper mantle, known as C-O-H fluids, only consider dissolved gas molecules such as CH_4, C_2H_6, CO, CO_2, H_2O, H_2 and O_2 (Zhang and Duan, 2009). Variants of the C-O-H fluid model have been widely used and shown to be very useful in studying metamorphic processes in the crust, where the fluids are dilute with respect to solutes other than dissolved volatile species (Manning, 2004). However, the fluid inclusion data cited above clearly show that deep crustal and upper mantle fluids can contain large amounts of solutes (e.g. Mg, Ca, Fe, Si, Al) in addition to volatile species. Furthermore, decades of experimental studies of mineral solubilities (Manning, 1994; Newton and Manning, 2000, 2002a, 2002b, 2006, 2010; Hunt et al., 2011), rock solubilities (Kessel et al., 2005; Dvir et al., 2011; Hermann et al., 2013; Adam et al., 2014; Kessel et al., 2015; Tsay et al., 2016; Tsay et al., 2017; Elazar et al., 2019), and aqueous speciation studies at high temperatures and pressures (Frantz et al., 1994; Zotov and Keppler, 2000, 2002; Martinez et al., 2004; Jahn and Schmidt, 2010; Mysen and Yamashita, 2010; Spiekermann et al., 2012; Louvel et al., 2013; Mysen et al., 2013; Louvel et al., 2014; Schmidt, 2014; Watenphul et al., 2014; Facq et al., 2014, 2016; Schmidt and Manning, 2017) have established that aqueous fluids at upper mantle pressures can contain more than 45 wt.% solutes of the rock-forming elements in the form of aqueous ions, complexes, and neutral species.

In order to begin to account for the complexity of deep Earth fluids and enable the development of quantitative models of deep crustal and upper mantle metasomatic reactions, the Deep Earth Water (DEW) model was developed (Sverjensky et al., 2014a; Sverjensky, 2019). The model was calibrated using aqueous speciation data derived from Raman spectroscopic studies for bicarbonate and carbonate species (Facq et al., 2014, 2016), sulfate species (Frantz et al., 1994), and the silica monomer and dimer species (Mysen, 2010), together with solubility data for single minerals including quartz (Manning, 1994 and earlier studies) and corundum (Tropper and Manning, 2007; Becker et al., 1983) or pairs of minerals, for example, forsterite plus enstatite (Newton and Manning, 2002b). However, none of the solubility measurements that were used extended beyond 2.0 GPa nor did they include solubility data on chemical systems more complex than one or two pure minerals. Consequently, without further calibration, calculations of chemical mass transfer could only predict minimal values for most of the rock-forming chemical elements (Sverjensky and Huang, 2015; Galvez et al., 2016; Debret and Sverjensky, 2017).

The main focus of the present study is to build on the established foundations of the DEW model using experimental solubility data for multicomponent systems from the literature extending to pressures beyond 2.0 GPa. A preliminary study of this type was published for a single temperature and pressure (Sverjensky and Huang, 2015). Here, we used experimental solubilities for synthetic, K-free eclogite (Kessel et al., 2005), K-free peridotite (Dvir et al., 2011), and K-bearing peridotite (Kessel et al., 2015) in the system Na_2O-K_2O-MgO-CaO-Al_2O_3-SiO_2-FeO-H_2O-CO_2-H_2 at 700–1000 °C and 4.0–5.0 GPa to calibrate the thermodynamic properties of aqueous metal complexes that could account for the high measured solubilities of these rocks. The bulk compositions of the synthetic eclogite and peridotites represent approximations to the compositions of mafic and ultramafic environments, respectively, in subduction zones and in the peridotite of the convecting upper mantle.

Using the equilibrium constants for metal-OH, metal-Si and metal-C complexes retrieved from fitting the experimental solubility data, we have developed an equation of state representation of each complex. The equation of state representation allows extrapolation of behaviors over a

wide range of pressures and temperatures, and demonstrates consistency with low temperature and pressure data where these are available in the literature. A new addition to the model involved expanding the activity-composition relationships for aqueous ions using previously developed theory (Helgeson et al., 1981), for aqueous CO_2, and for the solvent H_2O by transforming a previously built C-O-H fluid model (Duan and Zhang, 2006), so that predictions could be made over a much wider range of fluid compositions than previously possible. In addition, we have included a preliminary model for the abundance of the aqueous species $H_2CO_3^0$ (see below). In this way, the DEW model and associated aqueous speciation, solubility and chemical mass transfer codes are no longer restricted to water-rich compositions. As a result, it is now possible to compute predictive models of upper mantle metasomatism and diamond formation involving a wide range of fluid compositions (Huang, 2017).

2. METHODS

2.1. Theoretical models, assumptions, and uncertainties

2.1.1. The Deep Earth Water (DEW) model

The DEW model uses the Helgeson-Kirkham-Flowers (HKF) equations of state for aqueous species (Helgeson et al., 1981; Shock and Helgeson, 1988, 1990; Tanger and Helgeson, 1988; Shock et al., 1989; Shock et al., 1992, 1997; Plyasunov and Shock, 2001), together with revised predictive correlations between the equation of state coefficients and the standard partial molal properties of aqueous species (Facq et al., 2014; Sverjensky et al., 2014a; Sverjensky, 2019) to calculate the apparent standard partial molal Gibbs free energies of aqueous species at high pressures and temperatures. It was designed to be consistent with the basis for SUPCRT92 by using the same equations of state for aqueous species and by merging at 2.0 kb with the equations for the volume and dielectric constant of water. The calculated apparent standard partial molal Gibbs free energies of aqueous species are used to calculate equilibrium constants for the reactions of interest. The HKF approach was previously limited to an upper pressure of 0.5 GPa due to a lack of knowledge of the dielectric constant of water at higher pressures (Shock et al., 1992), but now the approach has been extended to 6.0 GPa and 1200 °C owing to recent theoretical and experimental advances (Facq et al., 2014; Pan et al., 2013; Sverjensky et al., 2014a). A summary of the DEW model and its revised predictive correlations for equation of state coefficients of aqueous species is given in Sverjensky (2019).

2.1.2. Aqueous speciation and solubility models

For the chemical system investigated here, involving the components Na_2O-K_2O-MgO-CaO-Al_2O_3-SiO_2-FeO-H_2O-CO_2-H_2, the existing DEW model species based on previously published data and predictive correlations are shown in Table 1. It should be noted that chloride, sulfur, nitrogen, and transition metal species other than those of iron are not included in Table 1 as they are not part of the chemical system investigated in the present study. However, these species can be added as needed (Mikhail and Sverjensky, 2014; Sverjensky et al., 2014b; Mikhail et al., 2017). As discussed below, the species in Table 1 provide a basis for predictions, but additional aqueous complexes and ionic species are needed to fit the experimental solubilities.

For computational purposes, the aqueous speciation and solubility model used in the present study can be envisioned in two steps. First, the basic aqueous model consists of a set of primary chemical species with known standard Gibbs free energies that suffice to represent the link between the aqueous model and the mineral components. Second, combinations of the primary species can be used to define complex aqueous species that increase the solubility of one or more chemical elements in the fluid. As an example, we give below the species and equations used in the present study for a preliminary speciation and solubility model for a mafic K-free eclogite experiment.

The primary chemical species from the list in Table 1 are H_2O, H^+, Na^+, Ca^{2+}, Mg^{2+}, Al^{3+}, $Si(OH)_4^0$, Fe^{2+}, and CO_3^{2-}, to which we add $O_{2(g)}$ for redox reactions. These ten, primary species are used in equilibria with chemical components of the eclogitic minerals clinopyroxene, garnet, coesite, and diamond in the experiments according to the following seven reactions with known standard Gibbs free energies:

$$CaMgSi_2O_6 + 4H^+ = Ca^{2+} + Mg^{2+} + Si(OH)_4^0 \quad (1)$$

$$NaAlSi_2O_6 + 4H^+ = Na^+ + Al^{3+} + Si(OH)_4^0 \quad (2)$$

$$Mg_3Al_2Si_3O_{12} + 12H^+ = 3Mg^{2+} + 2Al^{3+} + 3Si(OH)_4^0 \quad (3)$$

$$Fe_3Al_2Si_3O_{12} + 12H^+ = 3Fe^{2+} + 2Al^{3+} + 3Si(OH)_4^0 \quad (4)$$

$$Ca_3Al_2Si_3O_{12} + 12H^+ = 3Ca^{2+} + 2Al^{3+} + 3Si(OH)_4^0 \quad (5)$$

$$SiO_{2,coesite} + 2H_2O = Si(OH)_4^0 \quad (6)$$

$$C_{diamond} + O_{2,(g)} + H_2O = CO_3^{2-} + 2H^+ \quad (7)$$

It should be noted that not all the chemical components of the eclogitic minerals are needed to determine the fluid chemistry. For example, the hedenbergite component was not used to constrain the fluid chemistry, but instead the final computed state of saturation of the fluid with respect to hedenbergite was used as a check on the accuracy of the model (see below).

An eighth equation relates the concentrations of these species to achieve charge balance in the fluid:

$$\sum iC_m^{i+} = \sum jC_n^{j-} \quad (8)$$

where C_m^{i+} represents the concentration of positively charged ion m and C_n^{j-} is the concentration of negatively charged ion n in the model fluid, including charged complexes.

A ninth equation expresses the activity of water in terms of the mole fraction of water, which expresses the amount of water relative to the concentrations of all the solute species:

$$a_{H_2O} = X_{H_2O} \quad (9)$$

The remaining variable to be specified is the fugacity of oxygen (f_{O2}) which is a fit parameter for the model.

Table 1
DEW model aqueous species previously studied (see text). These are the species used to make the solubility predictions in Fig. 1.

ELEMENT	SPECIES
H	H_2O, H^+, OH^-, H_2^0
Na	Na^+, $Na(OH)^0$
K	K^+, $K(OH)^0$
Ca	Ca^{2+}, $Ca(OH)^+$, $CaCO_3^0$
Mg	Mg^{2+}, $Mg(OH)^+$, $MgHCO_3^+$, $MgCO_3^0$, $MgOSi(OH)_3^+$
Al	Al^{3+}, $Al(OH)_3^0$, $AlOH)_4^-$
Si	$Si(OH)_4^0$, $Si_2O(OH)_6^0$
Fe	Fe^{2+}, $Fe(OH)^+$, $Fe(OH)_2^0$, $Fe(OH)_3^-$
C	CO_2^0, HCO_3^-, CO_3^{2-}, $HCOOH^0$, $HCOO^-$ CH_3COOH^0, CH_3COO^-, CH_4^0

In summary, mass action expressions corresponding to Eqs. (1)–(7), Eqs. (8) and (9), and the f_{O2}, provide ten constraints enabling knowledge of the concentrations of the ten principal model species H_2O, H^+, Na^+, Ca^{2+}, Mg^{2+}, Al^{3+}, $Si(OH)_4^0$, Fe^{2+}, CO_3^{2-}, and $O_{2(g)}$ (provided that aqueous activity coefficients are accounted for, see below). If these were the only species in the model, their concentrations alone would define the solubility of the eclogite in terms of Na, Ca, Mg, Al, Si, Fe, and C. However, in practice, additional known aqueous species, including some metal complexes, were included in a preliminary model as shown in Table 1.

The additional thirty-one aqueous species listed in Table 1 can all be expressed as combinations of the principal species given above according to the equilibria,

$$H_2^0 + 0.5O_{2,(g)} = H_2O \quad (10)$$

$$OH^- + H^+ = H_2O \quad (11)$$

$$Na(OH)^0 + H^+ = Na^+ + H_2O \quad (12)$$

$$Ca(OH)^+ + H^+ = Ca^{2+} + H_2O \quad (13)$$

$$Ca(CO_3)^0 = Ca^{2+} + CO_3^{2-} \quad (14)$$

$$Mg(OH)^+ + H^+ = Mg^{2+} + H_2O \quad (15)$$

$$Mg(HCO_3)^+ = Mg^{2+} + H^+ + CO_3^{2-} \quad (16)$$

$$Mg(CO_3)^0 = Mg^{2+} + CO_3^{2-} \quad (17)$$

$$Mg(H_3SiO_4)^+ + H^+ = Mg^{2+} + H_4SiO_4(aq) \quad (18)$$

$$Fe(OH)^+ + H^+ = Fe^{2+} + H_2O \quad (19)$$

$$Fe(OH)_2^0 + 2H^+ = Fe^{2+} + 2H_2O \quad (20)$$

$$Fe(OH)_3^- + 3H^+ = Fe^{2+} + 3H_2O \quad (21)$$

$$Al(OH)_3^0 + 3H^+ = Al^{3+} + 3H_2O \quad (22)$$

$$Al(OH)_4^- + 4H^+ = Al^{3+} + 4H_2O \quad (23)$$

$$Si_2O(OH)_6{}^0 + H_2O = 2Si(OH)_4{}^0 \quad (24)$$

$$CO_2^0 + H_2O = 2H^+ + CO_3^{2-} \quad (25)$$

$$HCO_3^- = H^+ + CO_3^{2-} \quad (26)$$

$$HCOOH^0 + 0.5O_2 = 2H^+ + CO_3^{2-} \quad (27)$$

$$HCOO^- + 0.5O_2 = H^+ + CO_3^{2-} \quad (28)$$

$$CH_3COOH^0 + 2O_2 = 4H^+ + 2CO_3^{2-} \quad (29)$$

$$CH_3COO^- + 2O_2 = 3H^+ + 2CO_3^{2-} \quad (30)$$

$$CH_4^0 + 2O_2 = 2H^+ + CO_3^{2-} + H_2O \quad (31)$$

i.e. every additional species has an additional equilibrium constant that is used to constrain it. In addition, all the new charged ions or complexes in Eqs. (10)–(31) must be included in the charge balance equation (Eq. (8)). All the mass action expressions corresponding to the equilibria listed above have equilibrium constants that can be calculated with the DEW model. This is the basis of the preliminary model of the present study used to make the initial solubility predictions shown in Fig. 1. The predicted solubilities come from knowledge of the concentrations of all the above aqueous species and the mass balance equations for Na, Ca, Mg, Al, Si, Fe, and C given below:

$$m_{t,Na} = Na^+ + Na(OH)^0 \quad (32)$$

$$m_{t,Ca} = Ca^{2+} + Ca(OH)^+ + Ca(CO_3)^0 \quad (33)$$

$$m_{t,Mg} = Mg^{2+} + Mg(OH)^+ + Mg(HCO_3)^+ + Mg(CO_3)^0 + Mg(H_3SiO_4)^+ \quad (34)$$

$$m_{t,Fe} = Fe^{2+} + Fe(OH)^+ + Fe(OH)_2^0 + Fe(OH)_3^- \quad (35)$$

$$m_{t,Al} = Al^{3+} + Al(OH)_3^0 + Al(OH)_4^- \quad (36)$$

$$m_{t,Si} = Si(OH)_4{}^0 + 2Si_2O(OH)_6{}^0 \quad (37)$$

$$m_{t,C} = CO_2^0 + HCO_3^- + CO_3^{2-} + HCOOH^0 + HCOO^- + 2CH_3COOH^0 + 2CH_3COO^- + CH_4^0 \quad (38)$$

where $m_{t,Na}, m_{t,Ca}$, $m_{t,Mg}$ $m_{t,Fe}$, $m_{t,Al}$, $m_{t,Si}$, and $m_{t,C}$ represent the total dissolved molalities that can be compared with the experimentally measured concentrations of Na, Ca, Mg, Al, Si, and Fe as discussed below (C was not measured experimentally).

In practice, the equilibrium constants discussed above were calculated with the DEW model and incorporated in the Fortran code EQ3NR (Wolery, 1992) used in the present study for computing aqueous speciation and solubility models. The code was modified in order to perform calculations at high pressures up to 6.0 GPa and temperatures up to 1000 °C. The EQ3 code computes the equilibrium aqueous speciation of a fluid based on equilibrium with the given solid-solution components at specified temperatures, pressures, and oxygen fugacities as described in the above equations. The speciation model determines the total dissolved concentrations of each element and the state of saturation of the fluid with respect to all other minerals in the chemical system of interest that were not specified as input constraints. By comparing the model results against measured solubilities, additional new equilibrium constants of the main complexes responsible for the solubility can be determined. The activity coefficient models for ions and neutral species, and the solvent are discussed next.

2.1.3. Activity-concentration models for aqueous ions and neutral species, water, and minerals.

The individual ionic activity coefficients ($\bar{\gamma}_{j,P,T}$) of the jth aqueous species at elevated temperatures and pressures

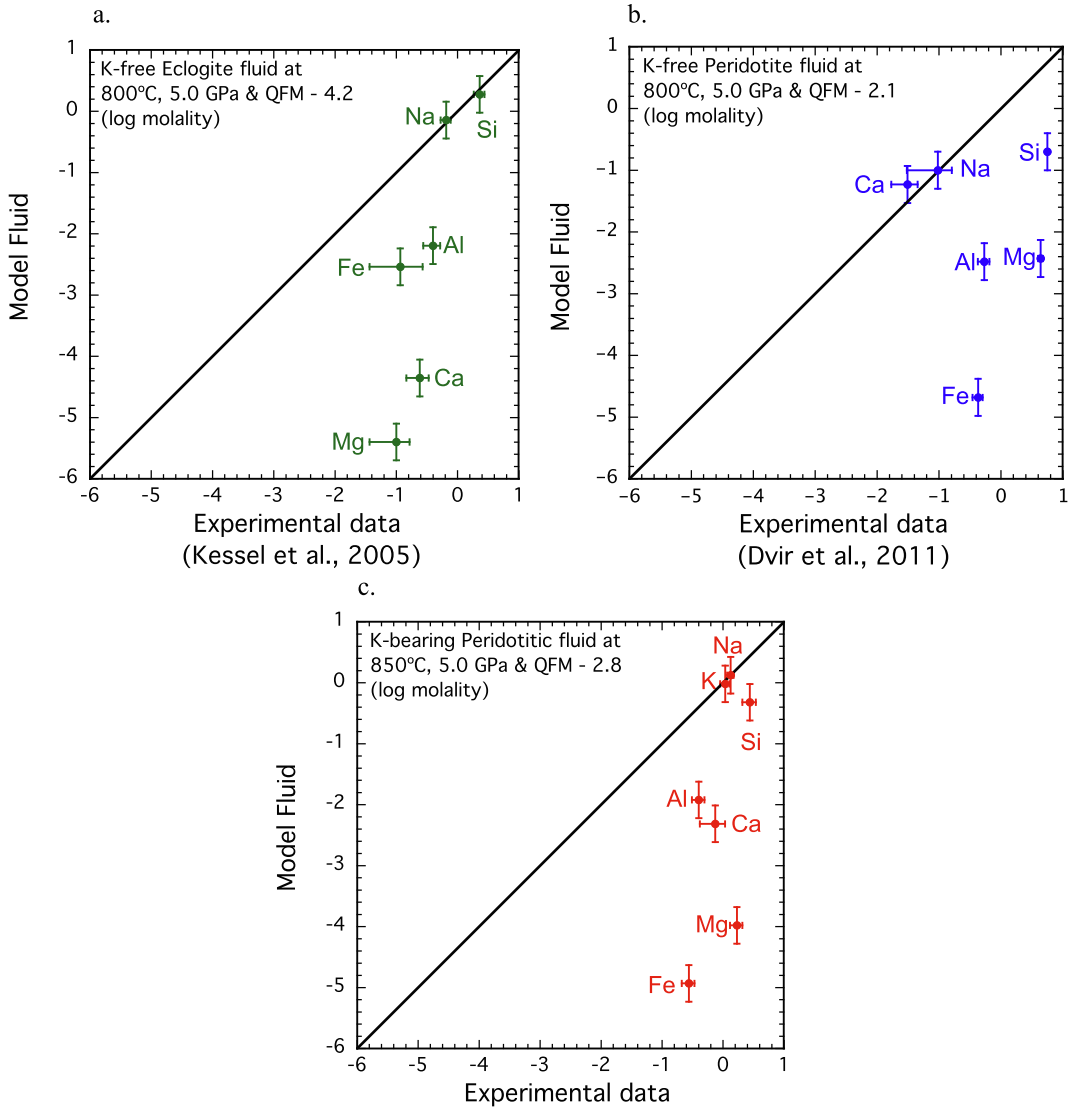

Fig. 1. The predictions made by the DEW model using the species and parameters given in Table 1. Solubility data of (a) K-free eclogite at 800 °C and 5 GPa (Kessel et al., 2005), (b) K-free peridotite at 800 °C and 5 GPa (Dvir et al., 2010) and (c) K-bearing peridotite at 850 °C and 5 GPa (Kessel et al., 2015). Error bars on X-axis are 1 standard deviation reported by experimental studies and Y-axis are overall estimated uncertainties of the model.

were calculated using the following equation (Helgeson et al., 1981):

$$\log\bar{\gamma}_{j;P,T} = \frac{A_\gamma Z_j^2 \bar{I}^{0.5}}{1 + a_k B_\gamma \bar{I}^{0.5}} + b_{\gamma,k}\,\bar{I} + \Gamma_\gamma \quad (39)$$

In Eq. (39), the first term on the right hand side is the Debye-Hückel term, which takes into account the long-range electrostatic interactions between ions: A_γ and B_γ are functions of temperature, and the density and dielectric constant of pure water; Z_j refers to the charge of the aqueous ion j; the ionic strength, $\bar{I} = \frac{1}{2}\sum_i m_i Z_i^2$, where m_i is the molality of the ith species; a_k represents an ion-size parameter for the kth salt in solution; $b_{\gamma,k}$ is an extended-term parameter for the kth electrolyte that takes into account the solvation dependence on ionic strength and the short-range interactions of ions as a function of pressure and temperature, and $\Gamma_\gamma = -(0.0180153)\log(1 + m^*)$, where m^* refers to the sum of molalities of all aqueous species in the solution (Helgeson et al., 1981). The extended-term parameter $b_{\gamma,NaCl}$ has been evaluated for temperatures and pressures up to 800 °C and 0.5 GPa (Oelkers and Helgeson, 1990) and showed trends with increasing pressure indicating that $b_{\gamma,NaCl}$ approaches zero at 0.5 GPa. Currently in our model $b_{\gamma,k}$ is assumed to be zero due to a lack of experimental data describing solvation as a function of ionic strength at temperatures and pressures greater than 800 °C and 0.5 GPa. This assumption is supported by previous discussions of solubility measurements (Manning, 2013).

For the activity coefficients of neutral species ($\log\bar{\gamma}_{n;P,T}$), because the formal charge on the species (Z_j) is zero, Eq. (39) can be replaced by

$$\log\bar{\gamma}_{n;P,T} = b_{\gamma,n} + \Gamma_{\gamma} \quad (40)$$

where Γ_{γ} is the same as in Eq. (39), and $b_{\gamma,n}$ is a function of temperature (°C) and pressure. For neutral species consisting of complexes such as $NaCl^0$ it was assumed that $\log\bar{\gamma}_{n;P,T}$ is equal to zero. Despite the paucity of data for the non-ideality of such species at elevated temperatures and pressures, our assumption is consistent with an evaluation of $b_{\gamma,NaCl^0}$ for temperatures and pressures up to 800 °C and 0.5 GPa indicated that $b_{\gamma,NaCl^0}$ approaches zero at pressures of 0.5 GPa (Oelkers and Helgeson, 1991). For the neutral silica species, Eq. (40) was used with $b_{\gamma,n} = 0.0$ and Γ_{γ} calculated from the total dissolved solute in the fluid. This effect is important in the present study only in coesite-saturated eclogitic fluids at 5.0 GPa and 900 and 1000 °C. However, for neutral dissolved gases, specifically CO_2^0 and CH_4^0, it can be expected that $b_{\gamma,n}$ will not be zero based on the extensive literature on metamorphic CO_2-H_2O fluid-mixing relations.

In the present study, we transformed the C-O-H fluid model activities of CO_2 (Duan and Zhang, 2006) from the pure fluid standard state for CO_2 to the hypothetical 1.0 m standard state of the aqueous species CO_2^0. As a first approximation, we then used empirical polynomial fits to the aqueous standard state activities as functions of pressure and temperature from 600 to 1000 °C at 4.0 and 5.0 GPa up to mole fractions of CO_2 of about 0.6 to obtain

$$b_{\gamma,CO_2} = -6.0803 + 0.012754T - 4.5714 \times 10^{-6}T^2 \ (4.0\ \text{GPa}) \quad (41)$$

$$b_{\gamma,CO_2} = -8.4495 + 0.01775T - 7.5004 \times 10^{-6}T^2 \ (5.0\ \text{GPa}) \quad (42)$$

All other neutral dissolved gas species were assumed to have the same activity coefficients as CO_2^0. The approximations represented by Eqs. (41) and (42) relate the large calculated model activities of dissolved gases such as CO_2^0 that result from using standard Gibbs free energies of formation referring to the hypothetical 1.0 m standard state to geologically reasonable concentrations of CO_2^0. An alternate approach (Galvez et al., 2016), uses the dielectric constant of mixed CO_2^0-H_2O fluids. However, the present approach keeps the non-ideality of such fluids in the extended term of the Debye-Hückel equation, which is the most appropriate place given the hypothetical 1.0 molal standard state used here.

As an additional complication for COH-fluid models, it should be noted that recent *ab initio* molecular dynamics calculations predict that CO_2^0 is a very minor species compared with $H_2CO_3^0$ at 727 °C and 10.0 GPa (Pan and Galli, 2016). No experimental geochemical studies at elevated temperatures and pressures have yet taken this transition into account, but the *ab initio* calculations indicate its importance. There should be regions of temperature-pressure space where CO_2^0, $H_2CO_3^0$, and H_2O will co-exist in a fluid phase. In the present study, as a first approximation, we have used a preliminary equation of state fit to the *ab initio* ratios of CO_2^0 and $H_2CO_3^0$ from Pan and Galli (2016) together with data referring to 5–45 °C (Wissbrun et al., 1954). The equilibrium constants and equation of state coefficients are summarized below with other complexes studied here. The effect of including $H_2CO_3^0$ in the present regressions of solubility data is minor: it raises the total dissolved oxidized carbon species at a given fugacity of oxygen, depending on the activity of water. However, it can be expected that under more oxidizing conditions than investigated in the present study, the inclusion of this species will significantly boost the total carbon carried by high temperature-pressure fluids.

The activity model of water in the present study assumed ideal mixing, calculated from the mole fraction of water relative to all the solutes. For example, on a molality basis, one kilogram of water has 55.51 moles, and if we assume the sum of all the solutes is 15.0 moles per kg H_2O, the activity of water is calculated to be $\frac{55.51}{55.51+15.0} = 0.787$. Because only one fluid phase is considered in the model, all dissolved gas and neutral organic species are treated without considering immiscibility.

The activities of the mineral components in the solid solutions from the experiments were calculated from the reported chemical analyses assuming ideal-site mixing. Although this assumption is not adequate for the purposes of geothermometry and geobarometry, because such calculations are sensitive to the non-ideality of solid solutions, the goal of the present study is the characterization of mineral solubilities in terms of aqueous complexes. In the present study, where the temperatures and pressures are known from the experimental conditions, by far the largest source of uncertainty lies in the identity and the standard free energies of the aqueous complexes. Consequently, ideal-site mixing is a reasonable first approximation. In the data files of the EQ3 code, the assumption of ideal site-mixing was achieved by expressing the formulae of each endmember mineral normalized to one cation per mixing site. For example, the olivine solid solution, $(Mg, Fe)_2SiO_4$, is treated as $(Mg, Fe)Si_{0.5}O_2$. The standard Gibbs free energies of formation of the end-member mineral components were calculated with the modified Berman thermodynamic database (Berman, 1988; Sverjensky et al., 1991) because it is more closely consistent with measured mineral solubilities from the literature (e.g. Sverjensky et al., 1991). The overall approach of the present study is supported by the applicability of the results to the chemistry of fluid inclusions in natural diamonds (Sverjensky and Huang, 2015; Huang, 2017).

2.2. Experimental mineral and fluid compositions used in the present study

As indicated above, the main purpose of this paper is to use high temperature and pressure experimental solubility data for multicomponent systems from the literature to calibrate the properties of aqueous species in the DEW model. We focused on the solubility measurements of a K-free eclogite (Kessel et al., 2005), a K-free peridotite (Dvir et al., 2011), and a K-bearing peridotite (Kessel et al., 2015). For convenience, these are referred to as KFE, KFP, and KBP, respectively. The eclogite has a mafic bulk

composition and the peridotites have a lherzolite composition. Detailed bulk compositions of the starting materials in the experiments can be found in the corresponding papers. The experiments were performed with a rocking, multi-anvil apparatus using the diamond trap technique, where the aqueous fluids are frozen and trapped after quenching. For each experiment, the fluids were analyzed by laser ablation into an inductively-coupled-plasma mass-spectrometer (ICP-MS). The solid products were identified using a scanning electron microscope (SEM) and the chemical compositions were measured with an electron microprobe. The mineral compositions used to constrain the fluid chemistry in our models are summarized in Appendix A according to the following assumptions:

(1) All Fe in the minerals is treated as Fe^{2+} in the solid solutions.
(2) Garnets are treated as solid solutions of pyrope, almandine, and grossular.
(3) Clinopyroxene compositions in the eclogite bulk composition are treated as solid solutions of diopside, hedenbergite, and jadeite.
(4) Clinopyroxene compositions in the two peridotitic bulk compositions are treated as solid solutions of diopside, hedenbergite, and clinoenstatite.

The fluid compositions measured in the experiments are summarized in Appendix B. The original chemical analyses of the fluids that were reported as weight percent of oxides and the measured mass of water by Kessel and co-workers were used calculate total dissolved elemental concentrations in molalities, which are more appropriate for aqueous speciation models.

2.3. Overall modeling approach and uncertainties in the thermodynamic models

The solubilities of the seven chemical elements Na, K, Mg, Ca, Fe, Al, and Si reported by Kessel and co-workers for the three different bulk rock compositions in water vary significantly. In many cases, dramatic differences in solubility were observed. Overall, it can be expected that the fluid chemistry, particularly the pH, and the aqueous speciation, should be very different for different bulk compositions of rock plus fluid. Therefore, the solubilities should also be different. In the present study, we take advantage of this to calibrate a variety of different aqueous complexes, the relative importance of which differ for the three different bulk compositions. For example, in the case of the eclogite (KFE) plus water, coesite is part of the experimental equilibrium mineral assemblage which results in relatively high concentrations of silica. Therefore metal-silicate complexes tend to be more important in the KFE fluids than in the KFP or KBP fluids.

Given experimental solubilities involving three different fluid chemistries, it follows that a maximum of three different complexes for each chemical element could be obtained by regression of the solubility data, i.e. a maximum of $3 \times 7 = 21$ complexes. In practice, only one or two new complexes for Na, Ca, Mg, Fe, Al, and Si were needed. In total, twelve new species were needed to fit the solubility data (Table 2).

Repeated trial regression calculations were made to fit the solubility data in attempts to minimize the number of complexes that were needed. The choice of complex was dictated by consideration of the likely major ligands available in the fluids, and consistency with published equilibrium constants for complexes or solubilities at lower temperatures and pressures. In the systems investigated here, possible ligands could include hydroxide, silicate, bicarbonate, carbonate, and organic carbon-bearing anions. The C-bearing species were considered here because preliminary calculations failed to account for the differences in fluid chemistry between the three different bulk compositions with only hydroxide or silicate complexes. It was inferred that C-species must be entering the fluids by equilibration with the very fine-grained diamond powder used in the diamond trap experiments, although it should be emphasized that there are no direct measurements of the carbon contents of the fluids in these experiments. According to Kessel et al. (2015), the total carbon in the fluid should correspond to an approximate upper limit of about $X_{CO_2} < 0.1$, which would correspond to a total C concentration in the fluid of less than 6.2 molal. By assuming that the fluids were in chemical equilibrium with diamond, it was possible to include aqueous C-speciation and solubility in our models. This, in turn, meant that the $logf_{O_2}$ of each experiment was important. Because the oxidation states were not controlled by a buffer in the experiments, a best fit value of $logf_{O_2}$ for each experiment was included as an additional variable in the regression procedure. It can be seen in Table 3 and Appendix C that model C concentrations in the present study are less than 6.2 molal in nine out of the thirteen experiments, but range from 8.0 to 18.0 m for four of the peridotite experiments. Although the latter are higher than the approximate upper limit suggested by Kessel and co-workers, the overall agreement is reasonable if we consider uncertainties in the $logf_{O_2}$ of the models and in the $CO_2 - CH_4 - H_2O$ activity-concentration relations. More recently, experiments have been reported with C added to the peridotite system (Dvir and Kessel, 2017). Such experiments can be used in the future to define the model C-activity-concentration ratios more precisely.

Several additional constraints were placed on the regression procedure:

(1) The calculated model solubilities were required to vary smoothly with temperature and pressure where sufficient data were available. For example, the experimental solubilities of the KFE at 5.0 GPa show some scatter with temperature from 700 to 1000 °C which was smoothed out during the regression procedure (see below).

(2) The equilibrium constants retrieved from the solubility data for different rock compositions at the same temperature and pressure were weighted to be as close as possible in numerical value. With very few exceptions this was typically achieved.

(3) The equilibrium constants obtained by fitting the solubility data should vary smoothly with temperature and pressure. This is a reasonable requirement as true thermo-

Table 2
New *logK* values of hydrated complexes in Eqs. (43)–(54) determined in the present study by fitting the experimental solubility data in Figs. 2–4 supplemented by independently predicted values. The *logK* values in bold represent regression of solubility data, whereas values in italics were estimated by calculation using the equations of state fitted to the values in bold when sufficient experimental data were not available (see text and Table 3). Values in plain text were taken from the regression results of either the K-free eclogite solubility experiments (KFE) or the K-free peridotite solubility experiments (KFP) or the K-bearing peridotite solubility experiments (KBP) when experimental data were available for any two rock types at the same temperature and pressure. For the silica trimer only two regression results could be obtained, the others are predicted from an equation of state fit.

Complex in Eqs. (43)–(54)	5.0 GPa & 700 °C			5.0 GPa & 800 °C			5.0 GPa & 850 °C			5.0 GPa & 900 °C			5.0 GPa & 1000 °C		
	KFE	KFP	KBP	KFE	KFP	KBP	KFE	KFP	KBP	KFE	KFP	KBP	KFE	KFP	KBP
$H_2CO_3^0$	*−0.87*			*−0.96*	*−0.96*				*−1.01*	*−1.04*			*−1.12*		*−1.12*
$Na(HCO_3)^0$	*−1.51*			*−2.10*	*−2.10*				*−2.09*	*−2.28*			**−2.5**		−2.8
$Ca(HCO_3)^+$	*−3.79*			*−4.34*	*−4.34*				*−4.60*	*−4.86*			*−5.37*		*−5.37*
$CaOSi(OH)_3^+$	**1.9**			**1.5**	1.5				*1.12*	**0.90**			**0.20**		0.2
$Ca(HCOO)^+$	*−3.72*			*−4.24*	*−4.24*				**−4.7**	*−4.76*			−4.7		**−4.7**
$MgOSi(OH)_2(HCO_3)^+$	**−7.3**			**−7.6**	**−8.0**				**−8.1**	**−8.0**			−8.5		**−8.5**
$Mg(OH)_2^0$	*5.21*			*4.82*	*4.82*				*4.67*	*4.55*			**4.4**		4.4
$FeOSi(OH)_3^+$	**−0.50**			**−0.7**	−0.7				*−0.95*	*−1.17*			**−1.7**		−1.7
$Fe(HCOO)^+$	*−6.66*			−7.4	**−7.4**				**−7.6**	**−7.8**			−8.1		**−8.1**
$Al(OH)_3OSi(OH)_3^-$	**2.8**			**2.0**	**1.6**				**1.6**	**1.6**			**1.1**		1.1
$SiO(OH)_3^-$	**−5.0**			**−5.2**	**−4.8**				**−5.1**	**−5.2**			*−5.70*		*−5.70*
$Si_3O_2(OH)_8^0$	*1.61*			*1.25*	*1.25*				*1.08*	**1.04**			**0.60**		0.60

Complex	4.0 GPa & 700 °C			4.0 GPa & 800 °C			4.0 GPa & 850 °C			4.0 GPa & 900 °C		
	KFE	KFP	KBP	KFE	KFP	KBP	KFE	KFP	KBP	KFE	KFP	KBP
$H_2CO_3^0$	*−0.71*	*−0.71*		*−0.81*	*−0.81*				*−0.85*			*−0.89*
$Na(HCO_3)^0$	**−1.80**	−1.8		*−2.14*	*−2.14*				*−2.17*			*−2.36*
$Ca(HCO_3)^+$	−4.0	**−4.0**		*−4.54*	*−4.54*				*−4.81*			*−5.07*
$CaOSi(OH)_3^+$	**1.2**	1.2		**1.0**	1.0				*0.87*			*0.63*
$Ca(HCOO)^+$	*−3.86*	*−3.86*		−4.2	**−4.2**				*−4.66*			*−4.91*
$MgOSi(OH)_2(HCO_3)^+$	**−7.65**	−7.65		−8.1	**−8.1**				**−8.2**			**−8.5**
$Mg(OH)_2^0$	5.0	**5.0**		**4.6**	4.6				*4.50*			*4.38*
$FeOSi(OH)_3^+$	**−1.0**	−1.0		**−1.2**	−1.2				*−1.45*			*−1.64*
$Fe(HCOO)^+$	−7.5	**−7.5**		−8.4	**−8.4**				**−8.3**			**−8.5**
$Al(OH)_3OSi(OH)_3^-$	**2.5**	**2.8**		**1.9**	1.7				**1.8**			**1.3**
$SiO(OH)_3^-$	**−5.4**	−5.4		*−5.66*	*−5.66*				**−5.70**			**−5.8**
$Si_3O_2(OH)_8^0$	*1.53*	*1.53*		*1.24*	*1.24*				*1.00*			*0.85*

Table 3
Comparison of predominant speciation in models of eclogitic and peridotitic fluids. Numbers in parentheses represent the percentage of the species out of the total dissolved element in the first column (see Appendix C for total dissolved concentrations).

	5.0 GPa, 800 °C		5.0 GPa, 1000 °C	
ELEMENT	K-free eclogitic fluid	K-free peridotitic fluid	K-free eclogitic fluid	K-bearing peridotitic fluid
Na	Na^+(93), $Na(OH)^0$(4), Na^+(3)	$NaHCO_3^0$(78), Na^+(19), $Na(OH)^0$(3)	Na^+(76),$NaHCO_3^0$(14), $Na(OH)^0$(10)	$NaHCO_3^0$(68), Na^+(26), $Na(OH)^0$(6)
K	–	–	–	K^+(76), $K(OH)^0$(24)
Ca	$CaOSi(OH)_3^+$(67), $Ca(HCOO)^+$(31), $Ca(HCO_3)^+$(1)	$Ca(HCOO)^+$(80), $Ca(HCO_3)^+$(13) $CaOSi(OH)_3^+$(6)	$CaOSi(OH)_3^+$(91), $Ca(HCOO)^+$(8)	$Ca(HCOO)^+$(59), $CaOSi(OH)_3^+$(33), $Ca(HCO_3)^+$(8)
Mg	$MgOSi(OH)_2(HCO_3)^+$(81), $Mg(OH)_2^0$(18)	$MgOSi(OH)_2(HCO_3)^+$(89), $Mg(OH)_2^0$(10)	$MgOSi(OH)_2(HCO_3)^+$(94), $Mg(OH)_2^0$(5)	$MgOSi(OH)_2(HCO_3)^+$(91), $Mg(OH)_2^0$(9)
Al	$Al(OH)_3OSi(OH)_3^-$(98), $Al(OH)_4^-$(1), $Al(OH)_3^0$(1)	$Al(OH)_3OSi(OH)_3^-$(96), $Al(OH)_4^-$(4)	$Al(OH)_3OSi(OH)_3^-$(97), $Al(OH)_4^-$(2), $Al(OH)_3^0$(1)	$Al(OH)_3OSi(OH)_3^-$(90), $Al(OH)_4^-$(8), $Al(OH)_3^0$(2)
Si	$Si(OH)_4^0$(41), $Si_2O(OH)_6^0$(17), $Al(OH)_3OSi(OH)_3^-$(14), $SiO(OH)_3^-$(12), $Si_3O_2(OH)_8^0$(4)	$MgOSi(OH)_2(HCO_3)^+$(77), $SiO(OH)_3^-$(12), $Al(OH)_3OSi(OH)_3^-$(8), $Si(OH)_4^0$(2)	$Si_3O_2(OH)_8^0$(48), $Si(OH)_4^0$(17), $Al(OH)_3OSi(OH)_3^-$(10), $CaOSi(OH)_3^+$(9), $Si_2O(OH)_6^0$(8), $SiO(OH)_3^-$(6)	$MgOSi(OH)_2(HCO_3)^+$(69), $Al(OH)_3OSi(OH)_3^-$(9), $CaOSi(OH)_3^+$(8) $SiO(OH)_3^-$(7), $Si(OH)_4^0$(6)
Fe	$Fe(HCOO)^+$(81), $FeOSi(OH)_3^+$(19)	$Fe(HCOO)^+$(100) $FeOSi(OH)_3^+$(<1)	$Fe(HCOO)^+$(74), $FeOSi(OH)_3^+$(26)	$Fe(HCOO)^+$(98), $FeOSi(OH)_3^+$(2)
C	CH_4^0(34), $MgOSi(OH)_2(HCO_3)^+$(18), $Fe(HCOO)^+$(14), $Ca(HCOO)^+$(10)	$MgOSi(OH)_2(HCO_3)^+$(47), $HCOO^-$(17), $H_2CO_3^0$(16) $Ca(HCOO)^+$(7), CO_3^{2-} (4) $Fe(HCOO)^+$(3)	$H_2CO_3^0$(41), CH_4^0(15), $HCOO^-$(12), $MgOSi(OH)_2(HCO_3)^+$(11), $NaHCO_3^0$(7), $Fe(HCOO)^+$(5), $Ca(HCOO)^+$(3)	$H_2CO_3^0$(54), $HCOO^-$(15), $MgOSi(OH)_2(HCO_3)^+$(14), $NaHCO_3^0$(6), $Ca(HCOO)^+$(3), $Fe(HCOO)^+$(4)
$logf_{O_2}$	−13.6	−12.1	−10.7	−9.8
ΔQFM	−3.1	−1.6	−3.3	−2.4
pH	4.45	5.18	4.81	5.27
a_{H_2O}	0.94	0.83	0.83	0.81

dynamic equilibrium constants can only depend on temperature and pressure, given the standard states used.

(4) The equilibrium constants obtained were expected to extrapolate to lower and higher temperatures consistent with previously determined equilibrium constants where these were available.

The overall uncertainties of this approach are difficult to estimate directly, considering error propagations from experiments, theoretical assumptions, and correlations. However, by comparing predicted solubilities with experimental results, it is estimated that the calculated equilibrium constants of aqueous species at high pressures and temperatures have overall uncertainties of ±0.3 log units (Sverjensky et al., 2014a), shown in the figures as error bars.

3. RESULTS

3.1. Preliminary model predictions without new complexes

Firstly, the experimentally measured mineral compositions were used to predict the fluid compositions using only the aqueous species given in Table 1 and constraints using Eqs. (1)–(42), i.e. without any additional metal complexes. This approach can be informative of the need for additional complexes, particularly in the absence of spectroscopic data on speciation (Manning, 2007; Wohlers and Manning, 2009; Manning et al., 2010; Cruz and Manning, 2015). Representative results can be seen for 800 °C and 0.5 GPa for each of the three rock types (Fig. 1). The predicted model fluid concentrations are plotted versus the experimentally measured fluid concentrations in terms of the logarithms of the molalities. The solid line on each plot represents perfect agreement between the predicted and measured solubilities. Clearly, the large scatter of the data below the solid line in each plot indicates that the species in Table 1 are, in general, inadequate to provide high enough solubilities in the model. However, the discrepancies are informative.

For example, for the eclogitic fluid (Fig. 1a), although the predicted Na and Si agree well with the experimental data, the predicted concentrations of Al, Mg, Fe, and Ca are 1.0 to 6.0 log units too low. The agreement of the model prediction for Na suggests that the predicted predominant model species, i.e. Na^+, is accurate. In the case of Si, the agreement represents a successful extrapolation of the properties of the silica monomer, $Si(OH)_4^0$, and dimer, $Si_2O(OH)_6^0$, that were previously calibrated with quartz solubilities referring to less than 2.0 GPa. However, the low model concentrations predicted for Fe and Al, and the extremely low values for Mg and Ca strongly suggest that additional complexes of these elements are needed in the model. Furthermore, the fact that Fe and Mg behave so differently in Fig. 1a suggests that the complexing for the two elements is different.

For both peridotitic fluids (Fig. 1b and c), the Na and K values lie on the 1:1 line because the experimental values were used in the model. These elements could not be constrained by a mineral solid solution in the peridotitic mineral assemblages. But in the cases of the other elements, it can be seen in Fig. 1b that the predicted model Si, Al, Mg, and Fe fall progressively below the 1:1 line. Here, again, Mg and Fe behave very differently, but this time, instead of Mg having the worst discrepancy, Fe has the worst. Again, this points to the possibility that the main complexes of Mg and Fe in the fluid are different. In contrast, in Fig. 1c, it can be seen that both Mg and Fe have the largest discrepancies between experiment and model. Interestingly, in all three fluids, only Al is systematically low with about the same discrepancy.

Overall, the results shown in Fig. 1a–c thus strongly suggest that additional metal complexes must be present in the fluids and should be added to the model to increase the calculated solubilities. Also, it is apparent in the figures that the elements with the greatest discrepancies between predicted and measured concentrations are different for the three different rock types. For example, the very low model values of Fe in the peridotitic fluids compared compared to the eclogitic fluid. Such differences suggest that more than one species of the Fe is an important contributor to the overall solubility. However, in the case of Al, the discrepancies are so similar it can be expected that it has the simplest speciation, i.e. involving only one major complex. Particularly intriguing are the very large experimental solubilities of Mg in the peridotitic fluids. Mg solubilities greater than 1.0 m under upper mantle temperatures and pressures are an enormous contrast to the known behavior of Mg in crustal hydrothermal systems, such as the mid-ocean ridge hydrothermal systems, where Mg is so insoluble it behaves as a trace element in the fluids.

3.2. Model calculations with new ions, neutral species, and metal-complexes

In the absence of direct experimental evidence of the speciation under these very high temperatures and pressures, deciding which metal-complexes to include in the model is clearly subject to considerable uncertainty. Until definitive evidence of the speciation in these fluids at elevated temperatures and pressures is available, we have developed a speciation model by taking the following approach. First, we consider for the chemical systems of interest here what are the most likely ligands to complex with the elements Mg, Ca, Fe, and Al. Possibilities include silicate, hydroxide, or oxidized/reduced carbon species such as organic acid anions (Sverjensky et al., 2014b). Second, the variety of experimental fluid chemistries offers an opportunity to calibrate a model that must be able to account for all three fluid chemistries imposed by the different bulk compositions. Finally, a useful guide is the available information on metal complexes in the literature. For example, the dissociation constant of the aqueous silica monomer has been studied previously as a function of temperature (Busey and Mesmer, 1977; Seward, 1974) and extrapolated theoretically with pressure (Sverjensky et al., 1997). Based on such studies, it can be expected that the dissociation of the aqueous silica monomer, $Si(OH)_4^0$, increases markedly with pressure, which implies that the silicate anion, $SiO(OH)_3^-$, might become a significant ligand in high pressure fluids, depending on the pH and total silica concentration. Interestingly, at temperatures up to 300 °C and low pressures, two different Al-silicate complexes have

been established in acidic and in alkaline solutions, respectively, based on solubility studies of boehmite and on NMR spectra at ambient conditions (Tagirov and Schott, 2001). Furthermore, at 800 °C and 10 kb, experimental measurement of the solubility of the assemblage corundum and kyanite provides further direct evidence of Al-silicate complexing, interpreted as $HAlSiO_4^0$(Manning, 2007). However, it should be noted that the pH values of fluids in equilibrium with corundum and kyanite are lower than those of the present study, which resulted in our choice of the negatively charged Al-silicate complex (i.e. deprotonated) determined by Tagirov and Schott (2001). In the cases of Mg- and Ca-silicate complexes, logK values of positively charged complexes have previously been quantified at 25 °C and 1.0 bar (Santschi and Schindler, 1974). These considerations enable us to refine estimates of the silicate anion stability and to establish preliminary estimates of the equilibrium constants of silicate complexes for Al, Mg, Ca, and Fe by fitting the experimental solubilities.

In the eclogitic fluids, at temperatures of 900 and 1000 °C at 5.0 GPa, the very high Si concentrations were accounted for by calibrating the equilibrium constant of a silica trimer previously quantified in studies of quartz solubility (Cruz and Manning, 2015; Hunt and Manning, 2012), and also suggested from Raman studies of fluids in equilibrium with coesite (Mysen et al., 2013). In the peridotitic fluids of the present study, the concentration of the trimer was found to be negligable, consistent with previous findings for forsterite plus enstatite (Mysen et al., 2013). However, in the peridotitic fluids (KFP and KBP), silicate complexes contributed a major part of the solubility, but the fluid chemistry of each is sufficiently different from each other and from the KFE system that additional complexes are required to fit the experimental data. In particular, the very high concentrations of Mg and Si in the peridotitic fluids, and the drop in the concentrations of these elements from the KFP to the KBP (Fig. 1b and c) required the presence in the model of a charged Mg-silicate-bicarbonate complex.

The new complexes quantified in the present study are discussed in more detail below. They are listed as hydrated species, e.g. $SiO(OH)_3^-$. The final list of twelve equilibria involving metal complexes, the aqueous silicate anion, the aqueous silica trimer, and carbonic acid includes the following:

$$H_2O + CO_{2,aq} = H_2CO_{3,aq} \quad (43)$$

$$NaHCO_3^0 = Na^+ + HCO_3^- \quad (44)$$

$$Ca(HCO_3)^+ = Ca^{2+} + HCO_3^- \quad (45)$$

$$CaOSi(OH)_3^+ + H^+ = Ca^{2+} + Si(OH)_4^0 \quad (46)$$

$$Ca(HCOO)^+ = Ca^{2+} + HCOO^- \quad (47)$$

$$MgOSi(OH)_2(HCO_3)^+ + H_2O = Mg^{2+} + Si(OH)_4^0 + HCO_3^- \quad (48)$$

$$Mg(OH)_2^0 + 2H^+ = Mg^{2+} + 2H_2O \quad (49)$$

$$FeOSi(OH)_3^+ + H^+ = Fe^{2+} + Si(OH)_4^0 \quad (50)$$

$$Fe(HCOO)^+ = Fe^{2+} + HCOO^- \quad (51)$$

$$Al(OH)_3OSi(OH)_3^- + 4H^+ = Al^{3+} + 3H_2O + Si(OH)_4^0 \quad (52)$$

$$Si(OH)_4^0 = H^+ + SiO(OH)_3^- \quad (53)$$

$$Si_3O_2(OH)_8^0 + 2H_2O = 3Si(OH)_4^0 \quad (54)$$

It should be noted that the above equilibria are written in terms of the hydrated silicate anion and hydrated metal-silicate and hydroxide complexes, and that it is these equilibria that are included in the regression model. As a consequence, the equilibrium constants obtained by regression have values that depend on the activity model used for the solutes and water. The values of $logK$ for the twelve complexes and other species that were retrieved by fitting the experimental solubilities are given in Table 2. The calculated concentrations of all the elements in the three different fluids corresponding to these equilibrium constants are plotted versus the measured values in Figs. 2–6 and listed in Appendix C together with the model values of $logf_{O_2}$, ΔQFM, pH, and a_{H_2O}. A comparison of the model fluid speciation results for all three rock types is given in Table 3. Particular efforts were taken to avoid overfitting the experimental data in terms of too many complexes. For example, it is explicitly noted in Table 2 that where two rock compositions were studied at the same temperature and pressure, e.g. KFE and KFP at 800 °C and 5.0 GPa, a maximum of only two equilibrium constants for a given chemical element were established by regression of the solubility data. The solubility results for each bulk rock composition are discussed in detail below.

3.3. The K-free eclogite (KFE) solubility

Garnet and clinopyroxene are the two principal mineral phases in all the K-free eclogite experiments. Minor amounts of coesite, kyanite, and rutile (less than about 3%) were reported for some but apparently not all the experiments, mostly as inclusions (Kessel et al., 2005). We assumed the fluid was in equilibrium with garnet, clinopyroxene, coesite, and diamond. The compositions of these minerals are more than sufficient to constrain the fluid composition in the model (Eqs. (1)–(7)). On this basis, all the fluid models gave a sensible result in that they were predicted to be slightly under-saturated with respect to kyanite. It is possible that the minor amounts of kyanite detected in the run products represent a quench phase. We did not include aqueous Ti species in our model. Therefore, we did not consider rutile. Inclusion of the speciation of aqueous Ti could be an extension of the current study by taking advantage of independent measurements of rutile solubility in the literature.

The grossular and pyrope components of garnet reported by Kessel et al. (2005) increase from 0.27 to 0.32 and 0.33 to 0.36, respectively, and almandine decreases from 0.40 to 0.32 with increasing temperature at 5.0 GPa (Appendix A). Similar trends with temperature occur at 4.0 GPa (Appendix A). The diopside, jadeite and hedenbergite components of the clinopyroxene do not change with temperature significantly, but the diopside component at 4.0 GPa is higher than that at 5.0 GPa (Appendix A).

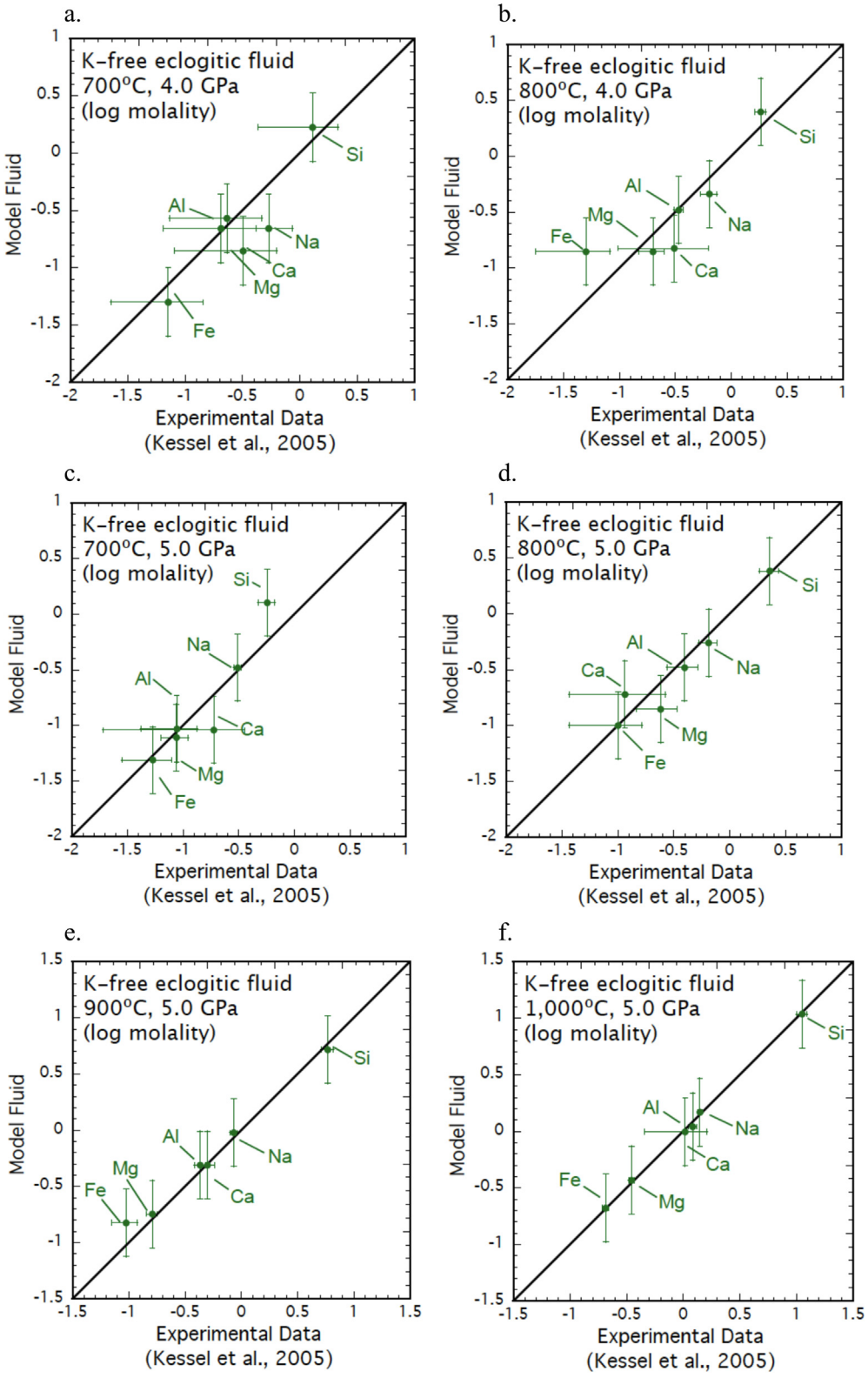

Fig. 2. Calculated solubilities of the elements versus the experimentally measured concentrations for the K-free eclogite in water (log molality): (a) and (b) refer to 4.0 GPa at 700 and 800 °C; (c)–(f) refer to 5.0 GPa from 700 to 1000 °C. Error bar information the same as Fig. 1. Fitted logKs and complexes are listed in Table 2.

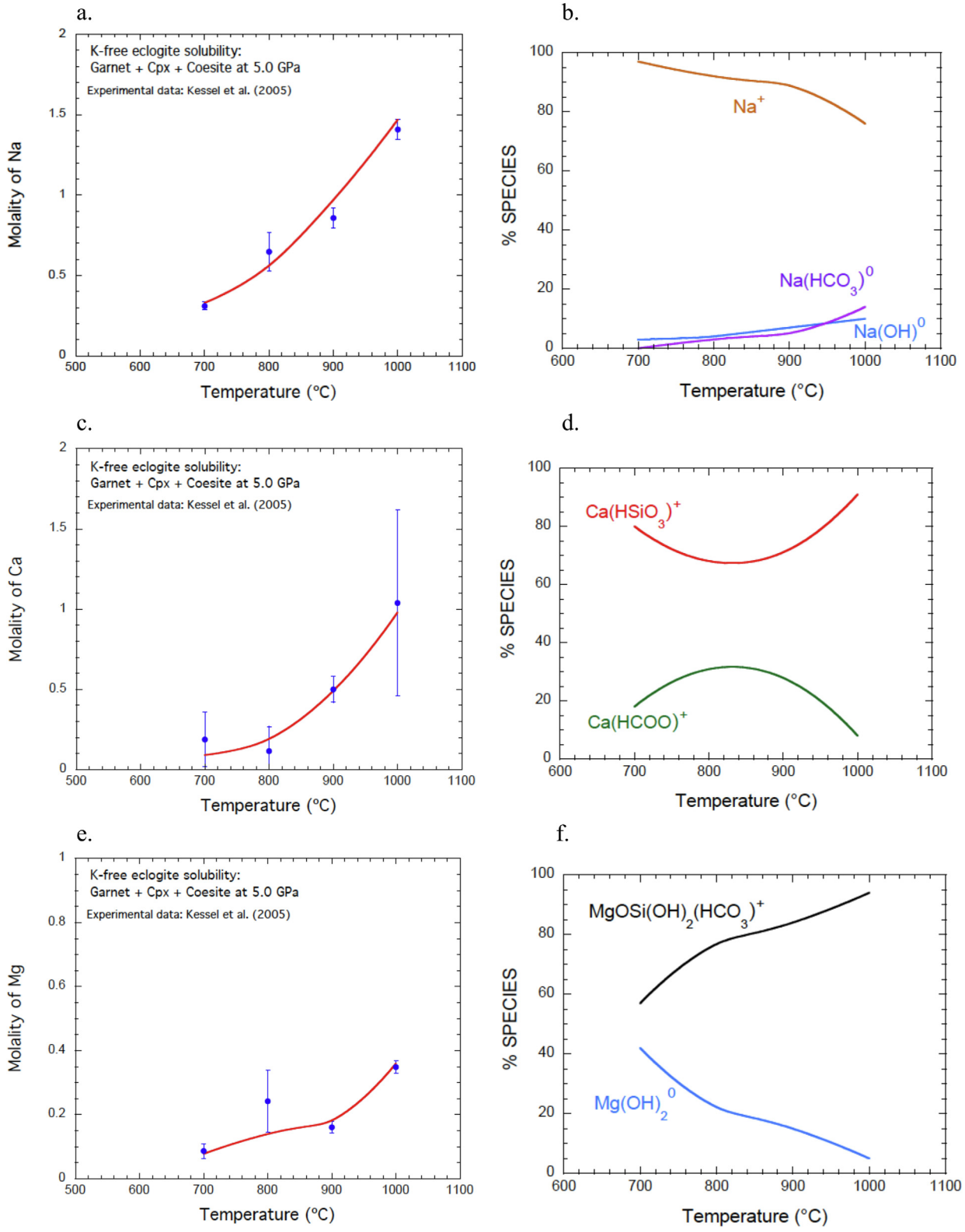

Fig. 3. Calculated versus experimental solubilities of the elements and their model speciation for the K-free eclogite in water from 700 to 1000 °C at 5.0 GPa: (a), (b) Na; (c), (d) Ca, (e), (f) Mg. Error bars as in Fig. 1.

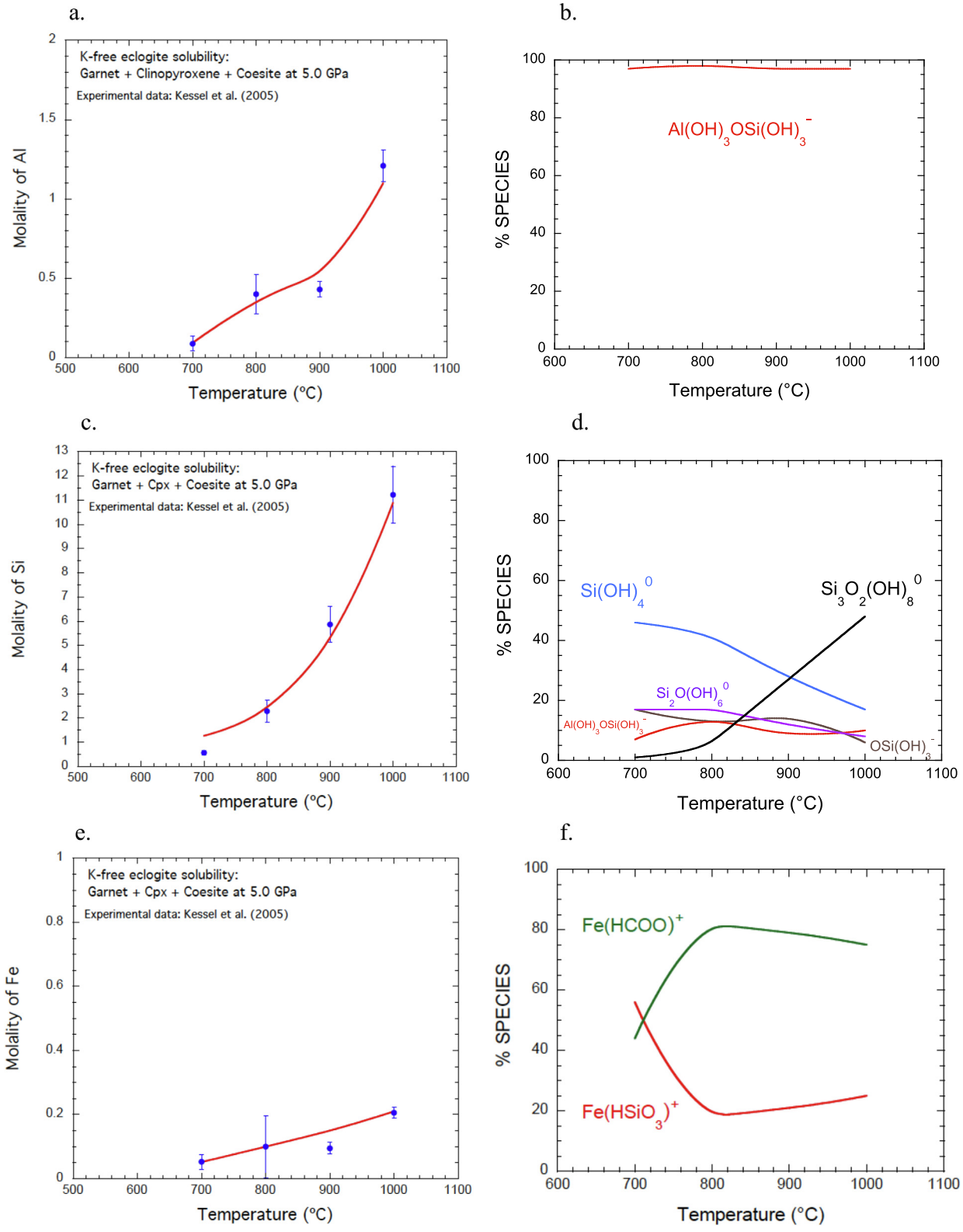

Fig. 4. Calculated versus experimental solubilities of the elements and their model speciation for the K-free eclogite in water from 700 to 1000 °C at 5.0 GPa: (a), (b) Al; (c), (d) Si, (e), (f) Fe. Error bars as in Fig. 1.

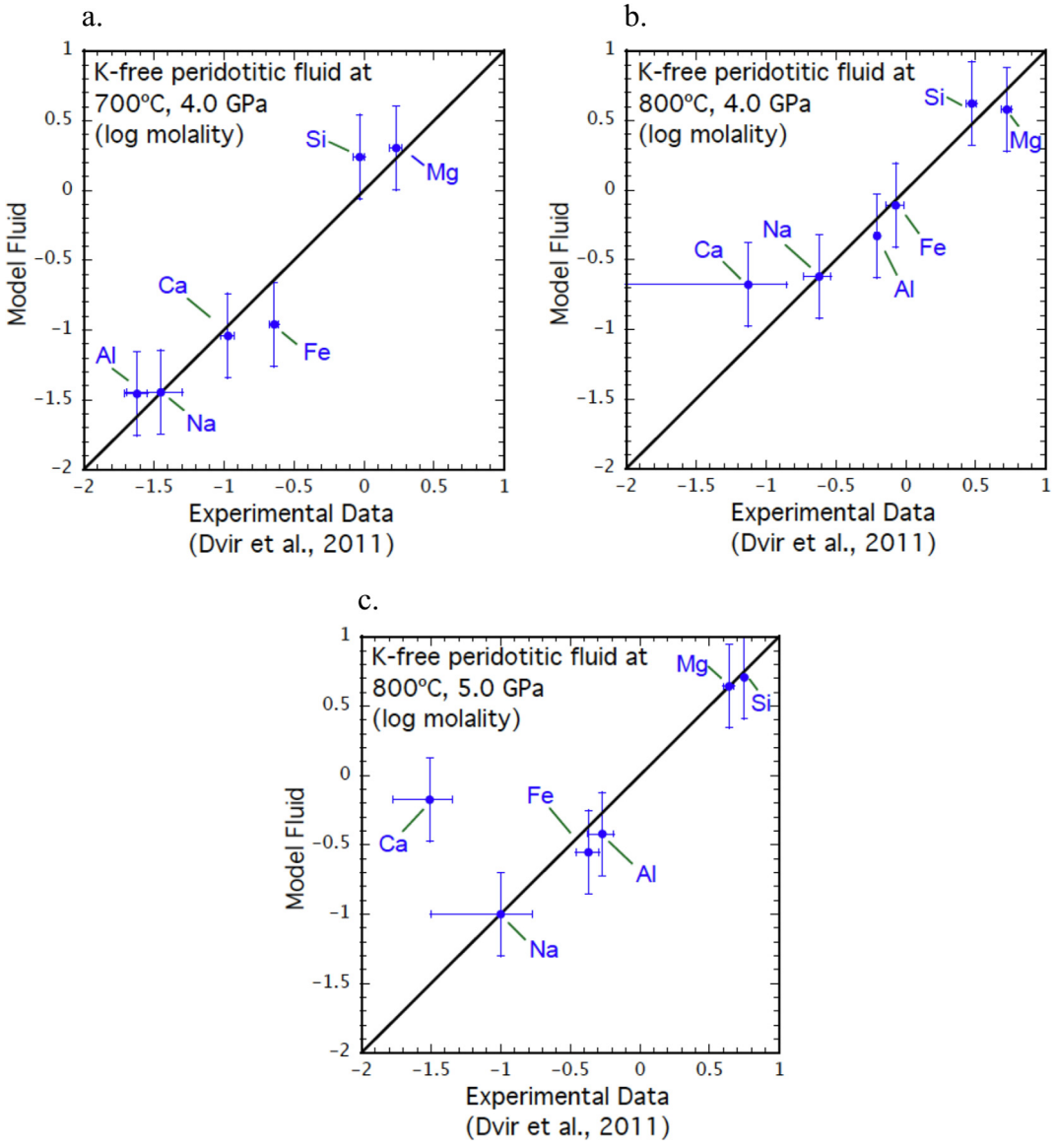

Fig. 5. Calculated solubilities of the elements versus the experimentally measured concentrations for the K-free peridotite in water (log molality): (a) and (b) refer to 4.0 GPa at 700 and 800 °C; (c) refers to 5.0 GPa at 800 °C. Error bar information the same as Fig. 1. Fitted logKs and complexes are listed in Table 2.

The eclogite solubility data are the most extensive in terms of a range of temperatures at a given pressure (Appendix B). For example, at 5.0 GPa, experiments were reported for 700 to 1000 °C. At higher temperatures melting occurred, which is outside the scope of our study. Much smaller ranges of temperature are available for the peridotites at either 4.0 or 5.0 GPa. All the eclogite data we have analyzed are reported as log–log plots in Fig. 2 in a manner analogous to the presentation in Fig. 1, i.e. the log of model fluid concentrations vs. the log of experimental data. However, in order to make optimal use of the extensive temperature range for the eclogite fluid chemistry at 5.0 GPa, and to ensure that the model solubilities of each element change smoothly with temperature, we have also plotted the measured molalities of each element as a function of temperature in Figs. 3 and 4, together with the relative abundances of the principal aqueous species of each chemical element.

It can be seen in Fig. 2a - f that, with a couple of exceptions, the model concentrations of all the elements agree very well with the measured experimental values within the uncertainties of the experiments and the model. At 5.0 GPa and 700 °C, the Si concentration is overestimated, but this is the only such instance for Si that lies outside the estimates of uncertainties. It is possible that our assumption that all the fluids were in equilibrium with coesite is not correct for this particular temperature and pressure. A second discrepancy between model and experiment involves Fe at 800 °C and 4.0 GPa (Fig. 2b), but the model value is close to being within uncertainty of the data.

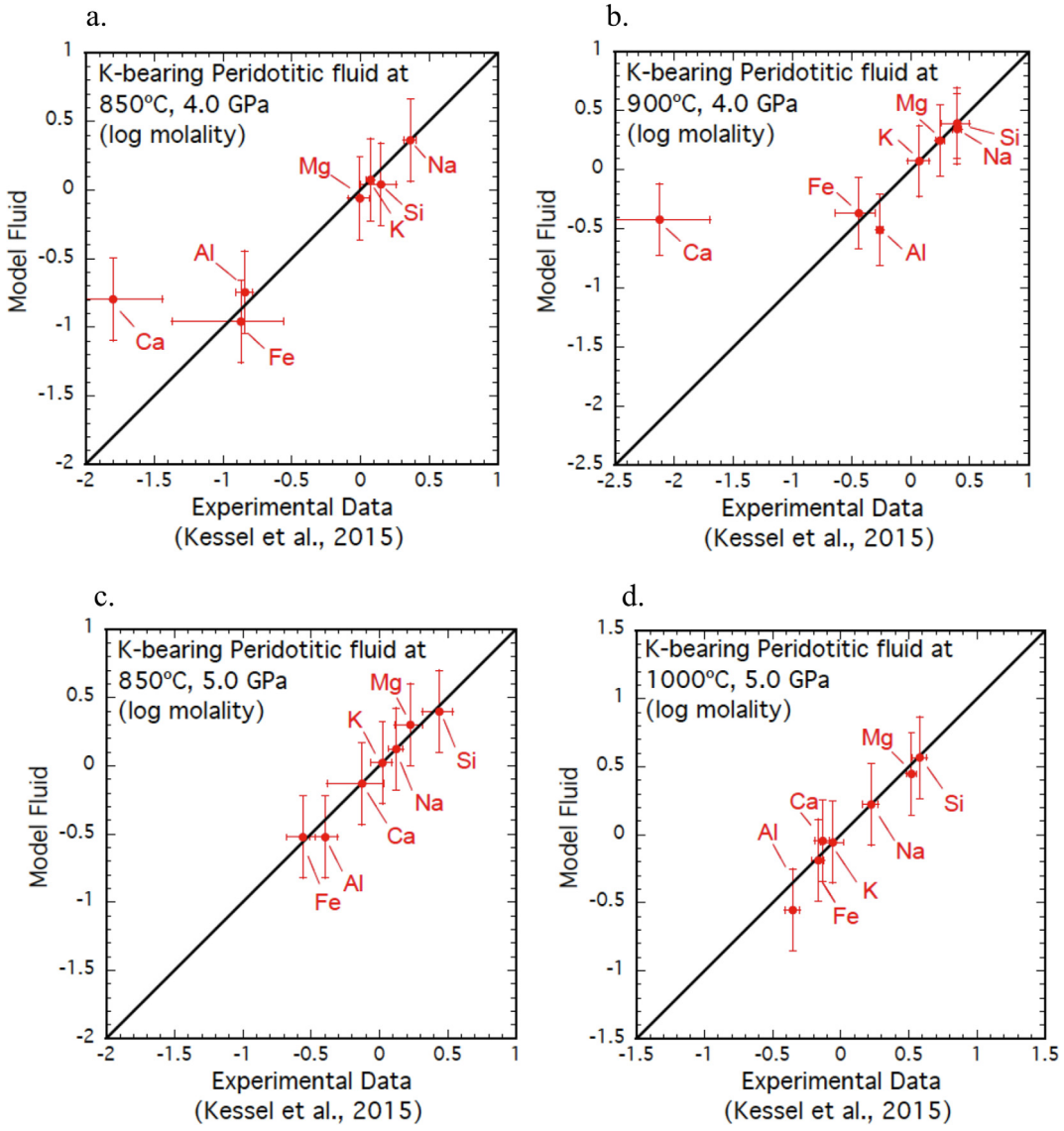

Fig. 6. Calculated solubilities of the elements versus the experimentally measured concentrations for the K-bearing peridotite in water (log molality): (a) and (b) refer to 4.0 GPa at 850 and 900 °C; (c) and (d) refer to 5.0 GPa at 850 and 1000 °C. Error bar information the same as Fig. 1. Fitted logKs and complexes are listed in Table 2.

The model trends of solubility for each element as a function of temperature at 5.0 GPa shown in Figs. 3 and 4 were deliberately chosen to smooth out scatter in the experimental data. For the most part, the model results agree closely with the experimental data. Overall, the solubilities of Na, Ca, Mg, Al, Si, and Fe all increase with increasing temperature, and increase rapidly as the melting temperature of the rock is approached (between 1000 and 1050 °C at 5.0 GPa, Kessel et al., 2005). This behavior is most dramatically shown for Na, Al, and Si. The Si concentrations of the KFE fluids become extremely high. Specifically, at 1000 °C and 5.0 GPa, the Si concentration reaches 11.2 molal – much higher than any measurement in the other two rock systems. The high measured silica solubilities at 900 and 1000 °C and 5.0 GPa required introduction of an additional silica species in the aqueous speciation and solubility model. We used a silica trimer ($H_8Si_3O_{10}$) because such species, or higher-order polymers of silica, have been thought to be important at these temperatures (Cruz and Manning, 2015; Hunt and Manning, 2012; Mysen et al., 2013). Even the solubility of Al, which has traditionally been regarded as an immobile element with respect to fluids under most crustal conditions, reaches concentrations of more than 1.0 molal at 1000 °C. In marked contrast, although Mg and Fe solubilities increase with temperature, they only reach about 0.2 to 0.4 molal at 1000 °C. Calcium has a behavior that is intermediate between Mg and Fe versus Al and Si. Trends in the model speciation of the major species for each chemical element are also shown in Figs. 3 and 4. These trends will be discussed below.

3.4. The K-free peridotite (KFP) solubility

Olivine, orthopyroxene, clinopyroxene, and either chlorite, a 10-$\mathring{A}$ phase, or garnet were the main minerals reported in the K-free peridotite system. Owing to a lack of thermodynamic data for the 10-$\mathring{A}$ phase, we only used experiments where the 10-$\mathring{A}$ phase was not detected. At experimental conditions of 700–850 °C and 4.0–5.0 GPa, the olivine was composed of forsterite (0.90 to 0.91) and fayalite (0.10 to 0.09), and the orthopyroxene was composed of enstatite (0.91 to 0.92) and ferrosilite (0.09 to 0.08) (Appendix A). Both are stable through all pressure and temperature conditions considered in the experiments. As noted above, the clinopyroxene compositions were approximated by diopside (0.47 to 0.62), hedenbergite (0.09), and clinoenstatite (0.29 to 0.42). The chlorite was represented by clinochlore (0.94) and chamosite (0.06). At 5.0 GPa and 800 °C, the chlorite was replaced by garnet composed of pyrope (0.62), almandine (0.19) and grossular (0.19).

All the KFP solubility data we have analyzed are reported as log-log plots in Fig. 5a–c in a manner analogous to the presentations above. Compared with the KFE fluids in Fig. 2a–f, Si is also abundant in the KFP fluids, but so is Mg. These fluids are Mg-Si-rich fluids. In fact, when compared at the same temperature and pressure, e.g. 800 °C and 5.0 GPa, the KFP fluids in equilibrium with ultramafic rock have even higher Si contents than the KFE fluids in equilibrium with mafic, coesite-saturated rock. In the models, this is accounted for by differences in speciation (Table 3). Different proportions of the Mg-Si-C complex vs. the $Mg(OH)_2$ complex and the silica trimer are predicted. The latter is predicted to be completely unimportant in the ultramafic fluids.

Only Ca shows major discrepancies between measured and model concentrations in Fig. 5. Although Ca at 700 °C and 4.0 GPa shows good agreement within the stated uncertainties (Fig. 5a), large discrepancies are apparent in Fig. 5b and c. The reason for the discrepancies in the Ca concentrations at these conditions might well be due to inappropriate Ca-complexes in the model. However, the good agreement of the Ca results at 5.0 GPa for the K-bearing peridotite (see below) suggests that possibly the experimental data for Ca are anomalously low, perhaps because of a phase formed during quench, or that possibly the solid-solution models involving Ca and Mg in the pyroxenes are insufficiently accurate. In contrast, the results for model Fe and Al solubilities in Fig. 5a – c agree extremely well with the experimental data with only one complex accounting for more than 90% of each of the dissolved Fe and Al (Table 3).

3.5. The K-bearing peridotite (KBP) solubility

The experiments here refer to a K-bearing lherzolitic rock chemistry. Olivine, clinopyroxene, orthopyroxene and garnet were the main minerals in this system. Olivine was composed of forsterite (0.93) and fayalite (0.07); clinopyroxene has a diopside component from 0.76 to 0.83, hedenbergite 0.06 to 0.07 and clinoenstatite 0.11 to 0.17; orthopyroxene was composed of enstatite (0.93 to 0.94) and ferrosilite (0.07 to 0.06); garnet was composed of pyrope (0.66 to 0.74), almandine (0.13 to 0.15) and grossular (0.18 to 0.19) (Appendix A). The main mineralogical consequence of including K in the peridotitic composition is the possibility of the precipitation of phlogopite. However, no phlogopite was detected in the experimental run products, possibly because of the relatively high water content in the experiments (16 wt%). Our calculations indicated supersaturation with respect to phlogopite at 4.0 GPa and 850 and 900 °C (log Q/K values of 0.7 and 0.4, respectively). Disequilibrium seems unlikely in experiments at these elevated temperatures, where great care was taken to rock the apparatus to ensure fluid mixing throughout the capsule. However, at 5.0 GPa and 850 and 1000 °C, the model fluids were calculated to be much closer to equilibrium with phlogopite (log Q/K values of 0.24 and of −0.29, respectively). It is possible that our results at 4.0 GPa are insufficiently accurate owing to the lack of K-bearing aqueous species additional to K^+ and $K(OH)^0$ currently in the model (Table 4), e.g. a species such as $KAlO_2^0$ (Wohlers and Manning, 2009). If so, such additional species does not appear to be important at 5.0 GPa, which would imply an unusually large pressure dependence for the equilibrium constant compared to the other complexes quantified in the present study.

All the KBP solubility data we have analyzed are reported as log–log plots in Fig. 6a–d in a manner analogous to the presentations above. As in the case of the KFP fluids, the regression concentrations of all the elements for the KBP fluids agree with the measurements within the stated uncertainties with the exception of the Ca at 850 and 900 °C and 4.0 GPa (Fig. 6a and b), where no reasonable equilibrium constants for Ca-complexes in the model could account for the extremely low experimental Ca concentrations. The reason for these discrepancies between model and experiment for the Ca concentrations at 4.0 GPa is again unclear. However, the experimental data for Ca in KBP fluids at 4.0 GPa appear to be anomalously low compared to the experimental data at 850 and 1000 °C and 5.0 GPa (Fig. 6a and b relative to 6c and d).

3.6. Equation of state representation of equilibrium constants of new metal-complexes and other aqueous species retrieved from the solubility measurements

The values of the equilibrium constants at 700–1000 °C and 4.0–5.0 GPa, established in the present study (Table 2), are depicted in Figs. 7–9 together with equilibrium constants referring to lower temperatures and pressures from the literature or obtained in the present study. In a few instances in Table 2, two values of the same equilibrium constant at a given temperature and pressure are listed. In these cases, the average of the two values is depicted in Figs. 7–9. The solid curves in the figures represent regression of the data points shown. Data points at low pressure and temperature were obtained from previous experiments, and the high pressure and temperature ones were retrieved by fitting the experimental data from Kessel et al. It should be noted that in these figures the anhydrous aqueous silicate

Table 4
Standard partial molal properties at 25 °C and 1.0 bar and quation of state coefficients for aqueous species based on regression of the equilibrium constants involving hydrated species (Table 2) retrieved from experimental solubilities (Figs. 2–4), independent predictions, and previously published correlations (see text). Note that the equilibrium constants for the hydrated and dehydrated reactions are identical (Appendix D). In this table, the individual dehydrated species are tabulated in order to express their standard partial molal properties and equation of state coefficients without conventional water properties.

SPECIES	ΔG_f^0 [a]	ΔH_f^0 [a]	S^0 [b]	C_P^0 [b]	V^0 [c]	$a_1 \times 10$ [d]	$a_2 \times 10^{-2}$ [a,i]	a_3 [c,j]	$a_4 \times 10^{-4}$ [f]	c_1 [b]	$c_2 \times 10^{-4}$ [f]	$\omega \times 10^{-5}$ [a]
$H_2CO_3^0$ [i]	−145,400	−164,229	43.0	86.5	46.0	10.3102	5.5332	0.1986	−3.0077	54.0971	14.5855	−0.3
$NaHCO_3^0$	−203,100	−219,552	32.0	62.0	39.0	9.4783	4.7412	0.8627	−2.9750	49.8727	9.5948	0.80
$Ca(HCO_3)^+$	−273,830	−294,350.	26.0	51.0	30.0	7.4225	2.7838	2.5039	−2.8941	37.5110	7.3541	0.1580
$Ca(HSiO_3)^+$	−376,299	−397,525	16.8	72.0	36.0	8.6546	3.9569	1.5204	−2.9426	51.1018	11.6318	0.2973
$Ca(HCOO)^+$	−217,930	–232,236	11.0	68	17.5	5.1038	0.5762	4.3550	−2.8028	49.5668	10.8170	0.3851
$MgSiC^+$ [g]	−454,300	−479,123	53.5	78.5	53.0	11.8226	6.9770	−1.0120	−3.0674	50.5582	12.9559	−0.1752
MgO_{aq}^0	−137,500	−139,804	24.6	−24.5	6.2	2.8684	−1.5521	6.1396	−2.7148	−5.4281	−8.0253	0.3000
$Fe(HSiO_3)^+$	−277,500	−298,539	14.0	77.0	38.2	9.1022	4.3830	1.1630	−2.9602	55.4228	12.6503	0.3397
$Fe(HCOO)^+$	−111,800	−112,263	59.0	30.0	27.0	6.6001	2.0008	3.1604	−2.8617	20.5995	3.0764	−0.3418
$AlO_2(SiO_2)^-$	−403,500	−440,456	4.0	32.0	34.8	9.0313	4.3155	1.2196	−2.9574	39.3711	3.4838	1.5685
$HSiO_3^-$	−242,855	−276,479	−3.5	16.0	21.2	6.4445	1.8526	3.2847	−2.8556	31.0405	0.2246	1.6821
$Si_3O_6^0$ [h]	−590,200	−656,130	13.0	119.0	67.7	15.1481	10.1393	−3.6636	−3.1982	85.1208	21.2057	1.0

[a] cal $mole^{-1}$.
[b] cal $mole^{-1}$ K^{-1}.
[c] cm^{-3} $mole^{-1}$.
[d] cal $mole^{-1}$.bar^{-1}.
[e] cal K $mole^{-1}$ bar^{-1}.
[f] cal K $mole^{-1}$.
[g] Abbreviation for the species $Mg(SiO_2)(HCO_3)^+$.
[h] Equation of state fit to the logK values in Table 2 for KFE at 900 and 1000 °C at 5.0 GPa as well as logK values of 0.79, 0.50, and 0.612 obtained by fitting the solubility of quartz at 800 and 900 °C and 1.0 GPa and 900 °C at 2.0 GPa, respectively. Solubilities were reported by Manning (1994) and Hunt & Manning (2012). The logK values here were corrected using Eq. (40), see text and plotted in Fig. 7c.
[i] Equation of state fit to the logK values ratios of H_2CO_3 and CO_2 reported by Wissbrun et al. (1954) and Pan and Galli (2016) shown in Fig. 7d.

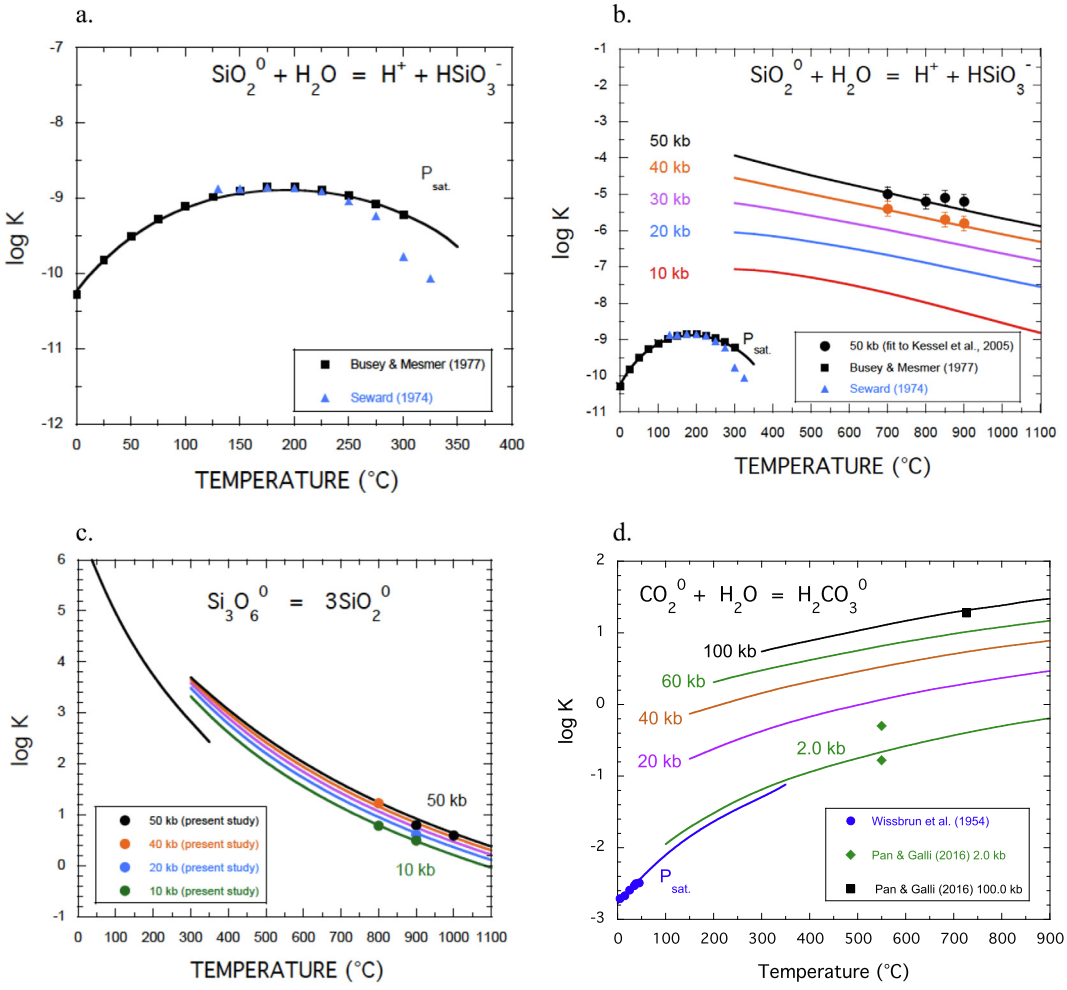

Fig. 7. Regression and extrapolation of the log K values of aqueous bisilicate, the silica trimer, and carbonic acid over a wide range of pressure and temperatures. Symbols at 4.0 and 5.0 GPa in a. - c represent equilibrium constants retrieved in the present study from the experimental solubilities of eclogite and peridotite (Table 2). Symbols at 1.0 and 2.0 GPa for the silica trimer represent regression quartz solubility data from Manning (1994) and Hunt and Manning (2012), see Table 4. The curves in Fig. 7d. represent a preliminary regression of published experimental and ab initio calculations (see text).

and metal-silicate and hydroxide complexes are depicted, i.e. waters of hydration have been removed. For example, the bisilicate anion $SiO(OH)_3^-$ is represented by $HSiO_3^-$. This makes no difference to the numerical values of the equilibrium constants in a balanced reaction because the water appears on both sides of the reaction. This approach was developed in a series of papers by Shock and co-workers (Shock and Helgeson, 1988, 1990; Shock et al., 1989; Shock et al., 1997; Sverjensky et al., 1997; Sverjensky et al., 2014a). Using the dehydrated species has the advantage that their standard partial molal properties at 25 °C and 0.1 MPa and HKF equation of state coefficients are consistent with linear correlations that can be used for predictive purposes, as discussed next.

Regression of the experimentally derived equilibrium constants shown in Figs. 7–9 as a function of temperature and pressure was carried out as described previously (Sverjensky et al., 1997; Facq et al., 2014, 2016; Sverjensky et al., 2014a) by taking advantage of correlations developed between the equation of state coefficients of the species of interest and the standard partial molal properties at 25 °C and 0.1 MPa. In the regression, the variables are the $\overline{S^0}$, $\overline{C_p{}^0}$, and $\overline{V^0}$ of the species referring to 25 °C and 0.1 MPa. The values of $\overline{S^0}$ and $\overline{C_p{}^0}$, are determined by the temperature dependence of the data, and the value of $\overline{V^0}$ is determined by the pressure dependence of the data. Ideally, this approach requires data referring to a wide range of temperatures (at least 300 °C) and at least two pressures differing by at least 1.0 GPa. It is also assumed that there is an experimentally derived value, or an estimate, of the $logK$ at 25 °C and 0.1 MPa. If such a value is not available, then the standard Gibbs free energy of formation ($\Delta\overline{G_f{}^0}$) of the species at 25 °C and 0.1 MPa also becomes a regression parameter, which adds to the uncertainty in determining the equation of state representation of a complex.

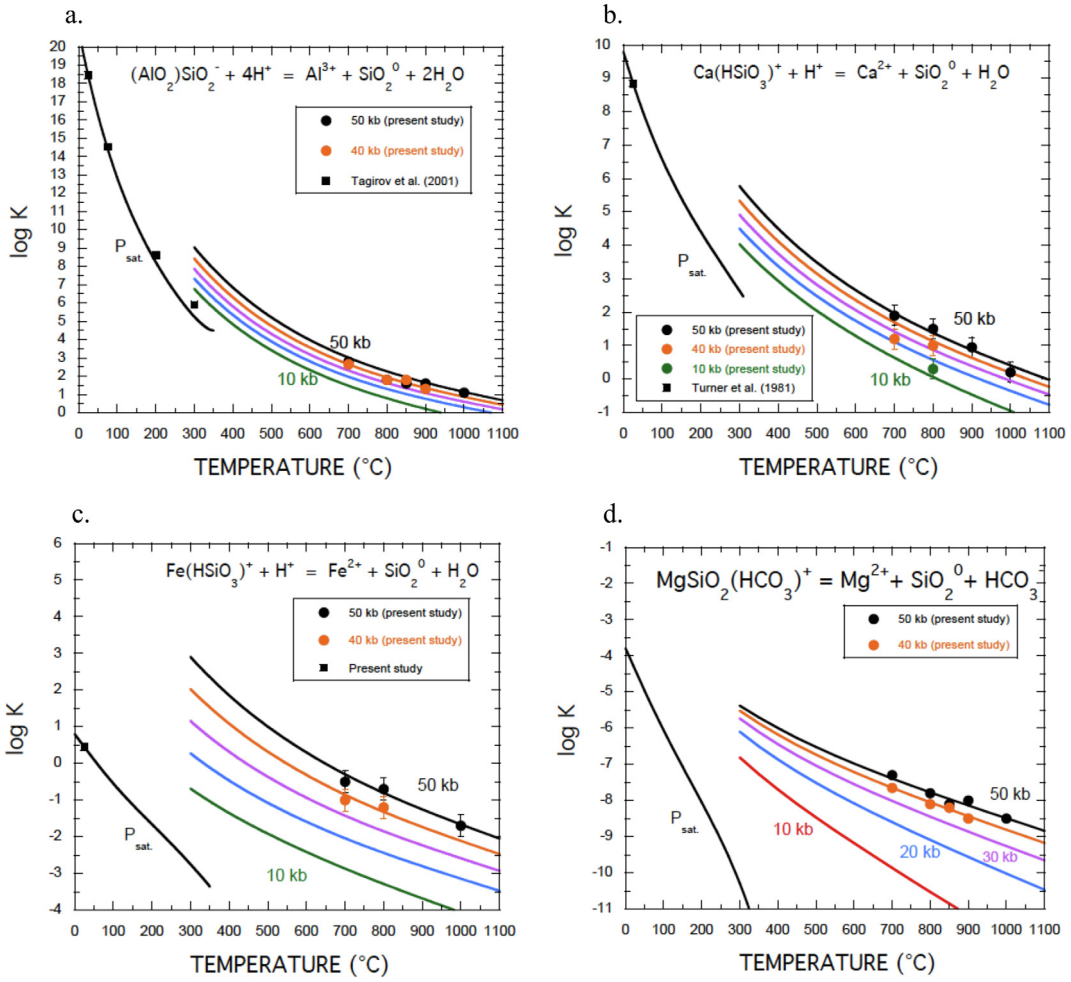

Fig. 8. Regression and extrapolation of the log K values of aqueous metal silicate complexes over a wide range of pressure and temperatures. Symbols at 4.0 and 5.0 GPa represent equilibrium constants retrieved in the present study from the experimental solubilities of eclogite and peridotite (Table 2).

The results of the regression calculations are represented by the curves in Figs. 7–9 and the parameters given in Table 4. Calculated values of *logK* for each complex over a wide range of temperatures and pressures are given in Appendix D. The curves in Figs. 7–9 show overall an excellent agreement with the experimentally derived data points in the figures. The advantage of using the HKF equation of state is that interpolations and predictions can be made over very wide ranges of temperature and pressure, up to 1100 °C in the figures. In some cases, the new high pressure experimentally-derived data points enabled a choice to be made between previously measured data that were inconsistent with each other. For example, in Fig. 7a and b, the temperature dependence of the dissociation of aqueous silica previously measured by Busey and Mesmer (1977) up to 300° C at Psat (pressure of liquid water–vapor saturation) is more closely consistent with the equilibrium constants obtained in the present study than the trend of the equilibrium constants reported by Seward (1974). This result, together with the discussion in Busey and Mesmer (1977), strongly suggests that the dissociation constants for $NaOSi(OH)_3^0$ reported in Seward (1974) are in error. In any case, the very strong pressure dependence of the dissociation of aqueous silica shown in Fig. 5, emphasized by the experimentally derived *logK* values at Psat and at 5.0 GPa, is an important new feature of the present study. It indicates that the bisilicate anion should be expected to be a major anion in silica-rich fluids at lower crustal and upper mantle conditions. As a result, metal-bisilicate complexes under these conditions should enable increased solubility and transport of the rock-forming elements, and perhaps many trace elements as well.

In Fig. 7c are preliminary regression curves for the silica trimer. In the case of the silica trimer, *logK* values derived from the eclogite solubility data at 800 °C and 4.0 GPa and 900 and 1000 °C at 5.0 GPa were regressed together with equilibrium constants obtained in the present study (Table 2) by regression of quartz solubility data referring to 800 and 900 °C and 1.0 GPa and 900 °C and 2.0 GPa (Manning, 1994, Hunt and Manning, 2012). The apparent

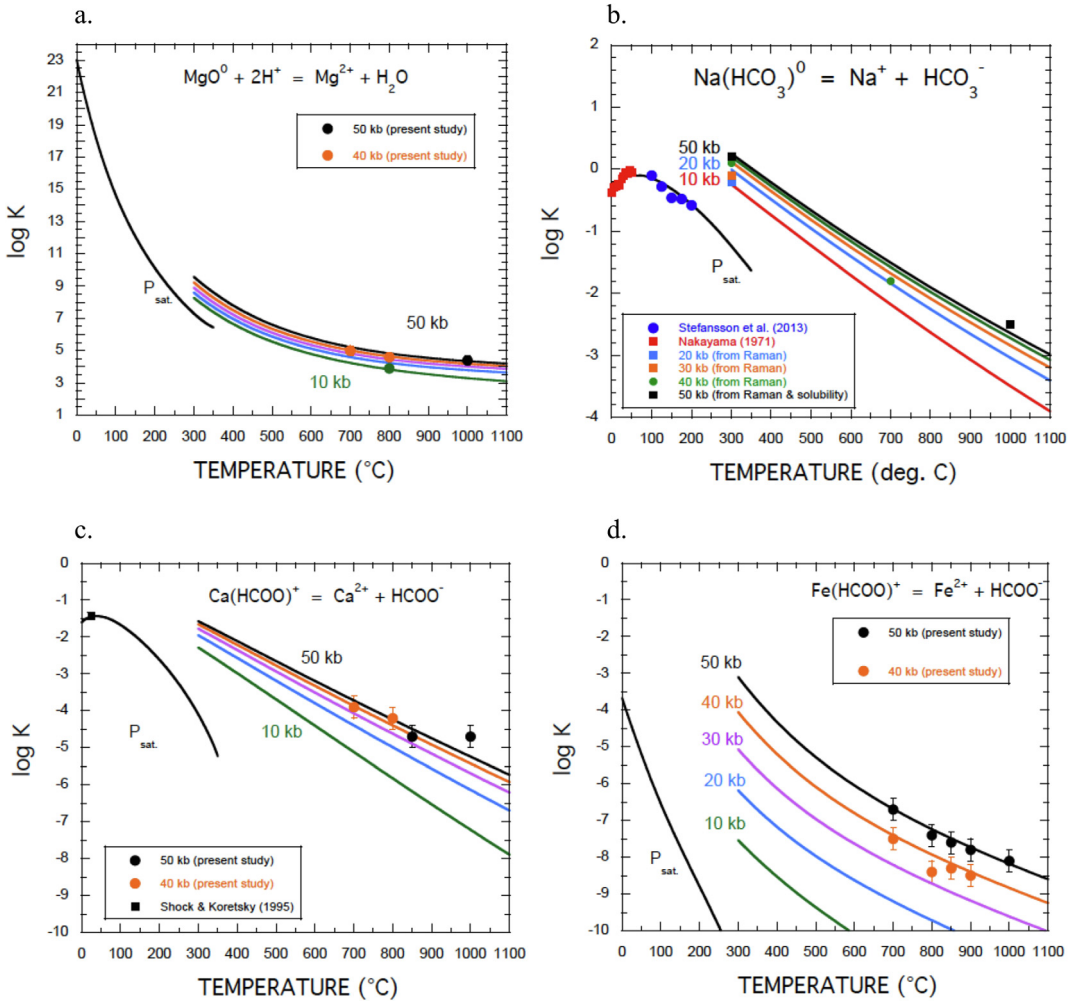

Fig. 9. Regression and extrapolation of the log K values of aqueous metal hydroxide, bicarbonate, and formate complexes over a wide range of pressure and temperatures. Symbols at 4.0 and 5.0 GPa represent equilibrium constants retrieved in the present study from the experimental solubilities of eclogite and peridotites (Table 2).

compatibility of all these equilibrium constants derived from single mineral solubilities and multiphase assemblages provides supports for the model. The same equilibrium constants predict negligable quantities of the trimer in peridotitic fluids.

In contrast to the solubility constraints on the equilibrium constants for the silica trimer, the calculated *logK* curves for carbonic acid association shown in Fig. 7d represent a preliminary representation of low temperature and pressure experimental data (Wissbrun et al., 1954) and the results of *ab initio* molecular dynamics calculations (Pan and Galli, 2016). Although very preliminary, the results strongly suggest that $H_2CO_3^0$ will predominate over CO_2^0 in fluids at geologically important conditions. for example, at pressures greater than about 2.0 GPa and temperatures greater than about 500 °C.

Metal-silicate complexes are an important new feature of the present study (Fig. 8). The bisilicate complexes of Al, Ca, and Fe, and the mixed Mg-bisilicate-bicarbonate complex all appear to play significant roles in the high-pressure fluids investigated in the present study (Table 3). The Al-bisilicate anion shown in Fig. 8a is a thoroughly studied metal-bisilicate complex at temperatures greater than ambient. The data points from 25 to 300 °C at Psat were derived from regression of the solubilities of *AlOOH* (Salvi et al., 1998; Tagirov and Schott, 2001) and, with the exception of 300 °C, are closely consistent with the data obtained in the present study from the eclogite and peridotite solubilities. It is interesting that this one Al-bisilicate complex was virtually the only important aqueous Al-species under the conditions investigated here. The $AlO(OH)^0$ and AlO_2^- species (Table 1), which are important in the solubility of corundum in water and in the NaOH-water system (Sverjensky et al., 2014a) are predicted to be minor species in the more complex chemical systems studied here. It is surprising because the aqueous chemistry of Al is much more complex at ambient and shallow crustal conditions.

In contrast to the Al-bisilicate species, the Ca- and Fe-bisilicate complexes and the Mg-bisilicate-bicarbonate complex shown in Fig. 8b – d have been much less studied previously. The equilibrium dissociation constant of the $Ca(H_3SiO_4)^+$ species was established at 25 °C and 0.1 MPa (Santschi and Schindler, 1974). This provides the lowest temperature constraint in Fig. 8b. An additional constraint is provided by an equilibrium constant at 800 °C and 1.0 GPa retrieved in the present study from the experimentally measured solubility of wollastonite in water (Newton and Manning, 2006). It can be seen in Fig. 8b that the *logK* at 800 °C and 1.0 GPa is consistent with the equilibrium constants retrieved in the present study at 4.0 and 5.0 GPa, which provides strong support for the results of the present study. However, no previous studies have reported the $Fe(H_3SiO_4)^+$ complex and the Mg-bisilicate-bicarbonate complex species shown in Fig. 6c and d. Consequently, the regression calculations represented by the smooth curves in these two figures are only a first approximation to characterizing these species.

The equilibrium constants for the hydroxide complex $Mg(OH)_2^0$, depicted in Fig. 9a as MgO^0, also represent just a first approximation to the properties of this species. However, it can be seen in Fig. 9a that the *logK* values at 4.0 and 5.0 GPa obtained in the present study are consistent with a value at 800 °C and 1.0 GPa obtained by regression of the solubility of forsterite + enstatite + graphite in water (Tiraboschi et al., 2018; Tumiati et al., 2017). The value of *logK* at 25 °C and 0.1 MPa for $Mg(OH)_2^0$ is similar to but smaller than estimates by analogy with data for $Sr(OH)_2^0$ and $Sr(OH)^+$ (Arcis et al., 2014) relative to $Mg(OH)^+$.

Finally, the equation of state representation of the equilibrium constants for the $Ca(HCOO)^+$ and $Fe(HCOO)^+$ complexes depicted in Fig. 9c and d represent a first approximation to regression of the equilibrium constants at high temperatures and pressures. Much more experimental data is needed to test the viability of these and other complexes proposed in the present study.

4. DISCUSSION

The results summarized above represent the first attempt to produce a detailed speciation model of fluids in equilibrium with multicomponent mineral assemblages at upper mantle conditions. None of this would be possible without the experimental data for the solubilities of K-free eclogite, K-free peridotite, and K-bearing peridotite (Kessel et al., 2005; Dvir et al., 2011; Kessel et al., 2015). A novel feature of the experimental data is the very high solubilities of the rock-forming elements under upper mantle conditions at 700–1000 °C and 4.0–5.0 GPa. As a consequence, the main task in developing the speciation models was the characterization of aqueous metal-complexes that could account for these high solubilities, and for the dramatic differences between the fluid chemistries in equilibrium with different bulk rock compositions.

Broad differences between the mafic eclogitic fluids and the ultramafic peridotitic fluids are clear from the solubility data themselves (Figs. 2, 5 and 6). In the eclogitic fluids, Mg and Fe have comparable solubilities and are almost always the least soluble elements. In contrast, in the peridotitic fluids, Mg typically has solubilities about ten times that of Fe. Furthermore, Mg and Si are the most abundant non-alkali elements in the fluids. This is a remarkable change in the behavior of Mg relative to Fe in particular. It is all the more remarkable if we recall that in crustal hydrothermal fluids, e.g. in the mid-ocean ridge systems, Mg is just a trace constituent and Fe is actually much greater in abundance (Von Damm, 1990). Of course, in the mid-ocean ridge systems, Cl^- is an important ligand for metals, particularly Fe above about 300 °C, which greatly enhances the solubility of Fe relative to Mg (Von Damm, 1990). It should be remembered that all the experimental data analyzed in the present manuscript refer to Cl^--free fluids. The effects of metal-chloride complexes at upper mantle conditions are still poorly known from an experimental standpoint.

The main difference between the two peridotitic fluids, i.e. KFP and KBP fluids, is that the Mg and Si concentrations in the fluids in equilibrium with KFP are significantly higher than in the KBP system. KBP fluids have intermediate Si concentrations between KFP and KFE fluids (compare Figs. 2, 5 and 6). Mg and Si are still two of the most abundant elements in the KBP fluids, and they become the most abundant by 1000 °C and 5.0 GPa. These differences between the two peridotitic fluids are well-accounted for by the model calculations. Another significant difference between the two peridotitic fluids is that the elements Al and Fe are much lower in solubility than Mg and Si in the KFP, whereas they are much closer in solubility in the KBP fluid. These differences between the two peridotitic fluids are also well-accounted for by the model calculations and illustrate the complexities of solubilities in fluids in equilibrium with rock types with different bulk compositions at upper mantle conditions.

The dramatic changes in fluid chemistry at high pressures become understandable if we recognize several important features of the model speciation of the high-pressure fluids (Figs. 3 and 4 and Table 3). One major feature of deep crustal and upper mantle fluids appears to be the strong dissociation of the aqueous silica monomer at high pressures (e.g. > 2.0 GPa). Consequently, in the absence of Cl^-, metal-silicate complexes become an important contributor to the overall elemental solubilities in Si-rich fluids. The elements Mg, Ca, Al, and Fe are all affected by such complexes. A second feature is that equilibrium aqueous speciation models predict the co-existence of a wide range of aqueous C-species in different oxidation states (Sverjensky et al., 2014b). These include not only CO_2^0, HCO_3^-, CO_3^{2-}, CO^0, and CH_4^0, but also $H_2CO_3^0$ and the organic acid anions such as formate, acetate, and propionate (Table 1). Therefore, in addition to metal-silicate complexes, high concentrations of organic acid anions such as formate lead to metal-formate species becoming important contributors to the overall elemental solubilities. The elements Ca and Fe form metal-formate complexes in the present study. Finally, a charged Mg-silicate-bicarbonate complex was used in the present study to help account for

the differences in chemistry between the two peridotitic fluids.

A detailed depiction of the predominant aqueous speciation in the eclogitic fluids at 5.0 GPa as a function of temperature can be seen in Figs. 3 and 4. In these fluids, Mg and Fe have low and similar concentrations dominated by the $MgOSi(OH)_2(HCO_3)^+$ and the Fe-formate and Fe-silicate complexes. The aqueous C-bearing complexes contain carbon in relatively oxidized states (+IV and + II, respectively), but these species are kept low and comparable in abundances by the low $logf_{O_2}$ values of the systems (ΔQFM of −2.5 to −3.3, Appendix C) which decreases the importance of the HCO_3^- and $HCOO^-$ complexes. However, in the peridotitic fluids at 5.0 GPa the Mg solubility is much greater than that of Fe, and correlates with high Si because the higher $logf_{O_2}$ (ΔQFM of −1.4 to −2.3, Appendix C) strongly favors the $MgOSi(OH)_2(HCO_3)^+$ complex which enhances the solubility of both Mg and Si relative to Fe. The $logf_{O_2}$ values for the eclogitic fluids obtained by regression in the present study are only about 1.0 unit lower than those measured directly using a metal sensor for the eclogite-H_2O-CO_2 system (Elazar et al., 2019). In the latter experiments, C as carbonate was added to the starting materials resulted in the total dissolved C being significantly higher than calculated in the present study, which can be expected to result in higher $logf_{O_2}$ values in equilibrium with diamond.

The different Mg and Si concentrations between the two peridotitic fluids is also primarily a function of the $logf_{O_2}$ difference between the KFP and the KBP fluids. At 5.0 GPa, the KFE fluid has ΔQFM of −2.2, which strongly favors the $MgOSi(OH)_2(HCO_3)^+$ complex, whereas the KBP fluid has −2.6 to −2.9, which weakens the relative importance of this complex. Furthermore, the effect of the high K^+ species concentration in the KBP fluid tends to suppress the $MgOSi(OH)_2(HCO_3)^+$ which itself is also positively charged. Overall, these two effects result in lower concentrations of Mg and Si in the KBP fluids relative to the KFP fluids, but Mg and Si are still the most abundant non-alkali elements in both fluids.

The complexities of Mg-Si-C speciation in the peridotitic fluids which are a function of temperature, pressure, oxidation state, and bulk rock composition form a stark contrast to the remarkably simple predicted model Al speciation in all the fluids studied here. It can be seen in Figs. 4 and 5 and Table 4 that more than 90% of the dissolved Al in all the fluids under all conditions is contributed by a single species, the $Al(OH)_3OSi(OH)_3^-$ complex. The Al-hydroxide complexes $Al(OH)_3^0$ and $Al(OH)_4^-$ are predicted to be very minor species. Furthermore, no additional Al-complexes appear to be necessary for the ranges of temperature, pressure, and bulk composition studied here. This is a surprising result, because a number of studies of mineral solubility involving much simpler chemical systems than the ones studied here provide indications of additional aqueous species not needed in the present study (Manning et al., 2010). Further experimental data on both solubility and speciation are needed to help understand this result.

5. CONCLUSIONS

The experimental solubilities of K-free eclogite, K-free peridotite, and K-bearing peridotite (Kessel et al., 2005; Dvir et al., 2011; Kessel et al., 2015) at 4.0–5.0 GPa and 700–1000 °C were analyzed to help understand the controls on solubilities of Na, K, Mg, Ca, Fe, Al, Si, and C in complex fluids at upper mantle temperatures and pressures. Aqueous speciation and solubility models were developed based on predicted equilibrium constants for a number of species and the retrieval of the dissociation equilibrium constants for twelve new species. The new species included the association of H_2O and CO_2 to form H_2CO_3, the dissociation of aqueous silica to $H_3SiO_4^-$, a silica trimer ($Si_3O_2(OH)_8^0$), Al- Ca- and Fe-silicate complexes, a silicate complex of Mg and bicarbonate ($MgOSi(OH)_2(HCO_3)^+$), and Mg-hydroxide, and Ca- and Fe-formate complexes. The dissociation constants were fitted with equations of state over wide ranges of temperature and pressure. The constants were consistent with available dissociation constant data at lower pressures and temperatures and are consistent with predictive correlations between the standard partial molal properties and equation of state coefficients. The results enable widespread prediction of equilibrium constants and therefore solubilities and aqueous speciation. Some interesting conclusions that can be drawn include the following:

(1) The dissociation of the aqueous silica monomer at pressures greater than about 2.0 GPa results in the bisilicate anion becoming an important ligand in Cl-free fluids under lower crustal and upper mantle conditions.
(2) Metal silicate complexes become an important means of transport of the rock-forming elements Mg, Ca, Fe, and Al in Cl-free fluids under lower crustal and upper mantle conditions. However, no evidence of Na- or K-bisilicate complexes was found.
(3) The speciation of Na and K in deep fluids may be quite simple. The Na^+ and K^+ ions appear to play important roles in water–rock interactions because they strongly affect the electrical charge balance in water. For example, the introduction of K in the peridotitic system (KFP vs KBP) severely decreases the Mg, Si and Al concentrations and increases the Ca and Na concentrations, possibly because K can change the charge balance and/or the pH of the fluids.
(4) The solubilities of upper mantle rocks increase strongly with increasing temperature under subsolidus conditions. At temperatures approaching 1000 °C, the KFE system is highly enriched in Si (up to about 11 molal) but Mg and Fe are the lowest abundance elements with similar concentrations. In contrast, the KFP and KBP fluids become highly enriched in Mg and/or Si with increasing temperature and Fe is more than a factor of ten lower in abundance than Mg.

(5) The pHs of the model upper mantle fluids increase with increasing temperature, which results in higher concentrations of the metal-OH complexes. Similarly, the $logf_{O_2}$ values of these fluids decrease with decreasing temperature, which results in a decrease in the metal-C complexes. The $logf_{O_2}$ values are controlled by equilibrium with diamond and the mixture of organic and inorganic C-species in the fluids.

(6) The Al-bisilicate complex, $Al(OH)_3OSi(OH)_3^-$, becomes by far the most important Al-complex at upper mantle conditions in the Cl-free fluids investigated in the present study. It has a very limited pressure dependence and a strong temperature dependence.

(7) Mg speciation is generally dominated by the mixed complex $MgOSi(OH)_2(HCO_3)^+$ in both the eclogitic and peridotitic fluids. As a result, the Mg and Si solubilities are strongly influenced by the oxygen fugacity of the system. In contrast, $Mg(OH)_2^0$ is a Mg-species that is largely influenced by the pH and becomes equal to the $MgOSi(OH)_2(HCO_3)^+$ under some conditions.

(8) $CaOSi(OH)_3^+$ is the main Ca species in eclogitic fluids and $Ca(HCOO)^+$ in peridotitic fluids depending on the pH and $logf_{O_2}$ values.

(9) $FeOSi(OH)_3^+$ is the main Fe-species in eclogitic fluids at 5.0 GPa and at low $logf_{O_2}$, but $Fe(HCOO)^+$ is the main Fe species in eclogitic fluids at 4.0 GPa and at high $logf_{O_2}$ and in the peridotitic fluids.

In summary, the solubility of the major rock-forming elements in upper mantle fluids is greatly enhanced at extreme conditions because of the stability of complexes that appear to involve silicate, hydroxide, formate, and bicarbonate species. The results of the present study provide a quantitative, thermodynamic basis for helping to interpret experimental studies of solubility and speciation, as well as enabling the modeling of important processes in the upper mantle including subduction zone mass transfer (Connolly and Galvez, 2018), metasomatism of the sublithospheric cratonic mantle and the fluid-rock interactions involved in the precipitation of diamond (Huang, 2017).

ACKNOWLEDGEMENTS

This research was supported by grants from the Alfred P. Sloan Foundation through the Deep Carbon Observatory (Extreme Physics and Chemistry program), a community-building Officer Grant from the Alfred P. Sloan Foundation, NSF grants EAR-1624325 and ACI-1550346, and the W.M. Keck Foundation (The Co-Evolution of the Geo- and Biosphere) Grant #10583-02. We are grateful for the help and support of the Johns Hopkins University, and the Geophysical Laboratory of the Carnegie Institution of Washington. We especially thank Ronit Kessel for discussions about her experimental results, and kind instruction on experimental techniques. We thank Y. Fei for providing experimental facilities in Geophysical Laboratory to study experimental solubility techniques. We acknowledge helpful discussions with X. Chu, I. Daniel, J. M. Ferry, M. Ghiorso, J. Hao, J. Huang, H. Hu, C. E. Manning, O. Navon, E. L. Shock. We thank Daniel Viete (Johns Hopkins University) for reading the manuscript and many helpful suggestions. Finally, we wish to acknowledge the extremely helpful reviews from C. E. Manning and J. C. Vrijmoed, and from Associate Editor Wolfgang Bach.

APPENDIX A. MODEL SOLID SOLUTION COMPOSITIONS OF K-FREE ECLOGITE, K-BEARING PERIDOTITE AND K-FREE PERIDOTITE (KESSEL ET AL., 2005; DVIR ET AL., 2011; AND KESSEL ET AL., 2015).

K-free Eclogite		4.0 GPa		5.0 GPa			
Minerals		700 °C[i]	800 °C	700 °C[i]	800 °C	900 °C	1000 °C
Garnet	Grossular	0.258	0.258	0.271	0.271	0.307	0.325
	Pyrope	0.371	0.371	0.333	0.333	0.356	0.354
	Almandine	0.371	0.371	0.396	0.396	0.336	0.321
Clinopyroxene	Jadeite	0.442	0.442	0.530	0.530	0.534	0.513
	Diopside	0.432	0.432	0.370	0.370	0.360	0.381
	Hedenbergite	0.126	0.126	0.100	0.100	0.106	0.106

K-bearing Peridotite		4.0 GPa		5.0 GPa	
Minerals		850 °C	900 °C	850 °C	1000 °C
Olivine	Forsterite	0.927	0.927	0.930	0.933
	Fayalite	0.073	0.073	0.070	0.067
Garnet	Grossular	0.188	0.175	0.185	0.136
	Pyrope	0.685	0.683	0.663	0.735
	Almandine	0.127	0.142	0.152	0.129

APPENDIX A (*continued*)

K-bearing Peridotite		4.0 GPa		5.0 GPa	
Minerals		850 °C	900 °C	850 °C	1000 °C
Clinopyroxene	Enstatite-Cl[ii]	0.170	0.108	0.167	0.142
	Diopside	0.763	0.829	0.768	0.793
	Hedenbergite	0.068	0.063	0.064	0.064
Orthopyroxene	Enstatite	0.930	0.929	0.932	0.938
	Ferrosilite	0.070	0.071	0.068	0.062

K-free Peridotite		4.0 GPa			5.0 GPa
Minerals		700 °C_1	700 °C_2	800 °C	800 °C
Olivine	Forsterite	0.904	0.898	0.902	0.909
	Fayalite	0.096	0.102	0.098	0.091
Chlorite	Clinochlore	0.940	0.935	ND[iii]	0.194 (Grs)[iv]
	Chamosite	0.060	0.065	ND[iii]	0.618 (Prp)[iv]
					0.188 (Alm)[iv]
Clinopyroxene	Enstatite-Cl[ii]	0.394	0.420	0.288	0.343
	Diopside	0.500	0.466	0.615	0.573
	Hedenbergite	0.106	0.114	0.098	0.085
Orthopyroxene	Enstatite	0.914	0.916	0.925	0.922
	Ferrosilite	0.086	0.084	0.075	0.078

i. Mineral compositions KFE at 700 °C and 4 GPa & 5 GPa are taken from 800 °C at the same pressure when not reported to have been measured.

ii. Enstatite-Cl is a clinopyroxene endmember with a composition of $Mg_2Si_2O_6$.

iii. ND = Not detected.

iv. Garnet replaced chlorite to be the stable phase. Grs = Grossular; Prp = Pyrope; Alm = Almandine.

APPENDIX B. EXPERIMENTALLY MEASURED FLUID COMPOSITIONS (KESSEL ET AL., 2005; DVIR ET AL., 2011; AND KESSEL ET AL., 2015) IN EQUILIBRIUM WITH KFE (K-FREE ECLOGITE), KFP (K-FREE PERIDOTITE), AND KBP (K-BEARING PERIDOTITE) EXPRESSED IN MOLALITY UNITS.

KFE	4.0 GPa		5.0 GPa			
Solubility	700	800	700	800	900	1000
Si	1.30	1.84	0.57	2.29	5.87	11.23
Al	0.21	0.34	0.09	0.40	0.43	1.21
Fe	0.07	0.05	0.05	0.10	0.09	0.21
Mg	0.23	0.20	0.09	0.24	0.16	0.35
Ca	0.32	0.31	0.19	0.12	0.50	1.04
Na	0.54	0.64	0.31	0.65	0.86	1.41
H2O	0.09	0.08	0.09	0.08	0.07	0.05
	4.0 GPa		5.0 GPa			
Uncertainties	700	800	700	800	900	1000
Si	0.859	0.201	0.098	0.452	0.746	1.17
Al	0.215	0.030	0.046	0.121	0.048	0.10
Fe	0.071	0.034	0.025	0.064	0.024	0.01
Mg	0.237	0.051	0.024	0.096	0.018	0.02
Ca	0.309	0.319	0.169	0.153	0.080	0.58
Na	0.331	0.106	0.024	0.121	0.061	0.06

KFP	4.0 GPa		5.0 GPa
Solubility	700	800	800
Si	0.69	2.96	5.57
Al	0.02	0.62	0.54
Fe	0.13	0.85	0.43
Mg	1.23	5.29	4.32
Ca	0.09	0.07	0.03
Na	0.03	0.24	0.10
H2O	0.09	0.07	0.06
	4.0 GPa		5.0 GPa
Uncertainties	700	800	800
Si	0.065	0.254	0.181
Al	0.004	0.023	0.114
Fe	0.009	0.123	0.081
Mg	0.118	0.456	0.386
Ca	0.010	0.067	0.014
Na	0.011	0.053	0.066

KBP	4.0 GPa		5.0 GPa	
Solubility	850	900	850	1000
Si	1.41	2.48	2.76	3.81
Al	0.14	0.55	0.40	0.45
Fe	0.13	0.37	0.27	0.69
Mg	0.99	1.77	1.68	3.31
Ca	0.02	0.01	0.75	0.74
Na	2.31	2.48	1.33	1.67
K	1.19	1.19	1.09	0.88
H2O	0.07867	0.0709	0.0709	0.063
	4.0 GPa		5.0 GPa	
Uncertainties	850	900	850	1000
Si	0.419	0.230	0.681	0.486
Al	0.020	0.036	0.094	0.056
Fe	0.142	0.133	0.065	0.073
Mg	0.180	0.147	0.385	0.272
Ca	0.020	0.013	0.332	0.093
Na	0.234	0.660	0.164	0.220
K	0.078	0.249	0.189	0.172

APPENDIX C. BEST FIT COMPUTED MODEL FLUID COMPOSITIONS (FIGS. 2–6) IN EQUILIBRIUM WITH KFE (K-FREE ECLOGITE), KFP (K-FREE PERIDOTITE), AND KBP (K-BEARING PERIDOTITE) EXPRESSED IN MOLALITY UNITS AS WELL AS THE MODEL VALUES OF $logf_{O_2}$, ΔQFM, pH, AND a_{H_2O}. NUMBERS IN ITALICS FOR NA AND K IN THE PERIDOTITES WERE FIXED IN THE MODEL AT THE EXPERIMENTAL VALUES (SEE TEXT AND APPENDIX A).

K-free eclogite	4.0 GPa		5.0 GPa			
	700	800	700	800	900	1000
Na	0.22	0.46	0.33	0.55	0.95	1.48
Ca	0.14	0.15	0.091	0.19	0.49	0.99
Mg	0.27	0.14	0.078	0.14	0.18	0.37
Al	0.22	0.33	0.093	0.33	0.49	1.1
Si	1.68	2.5	1.27	2.42	5.2	10.9
Fe	0.050	0.14	0.049	0.10	0.15	0.21
C	0.64	1.7	0.31	0.58	1.2	3.0
$logf_{O_2}$	−15.8	−14.4	−15.8	−13.60	−12.0	−10.4
ΔQFM	−2.5	−3.2	−3.3	−3.1	−3.2	−3.0
pH	4.62	4.74	4.38	4.45	4.57	4.81
a_{H_2O}	0.96	0.93	0.97	0.94	0.90	0.83

K-free peridotite	4.0 GPa		5.0 GPa
	700	800	800
Na	*0.036*	*0.24*	*0.10*
Ca	0.091	0.21	0.67
Mg	2.0	3.8	4.4
Al	0.035	0.47	0.38
Si	1.7	4.2	5.1
Fe	0.11	0.78	0.28
C	3.5	13.0	8.4
$logf_{O_2}$	−14.8	−12.6	−12.1
ΔQFM	−1.5	−1.4	−1.6
pH	5.23	5.34	5.18
a_{H_2O}	0.92	0.79	0.83

K-bearing peridotite	4.0 GPa		5.0 GPa	
	850	900	850	1000
Na	*2.30*	*2.48*	*1.33*	*1.67*
K	*1.19*	*1.19*	*1.05*	*0.88*
Ca	0.16	0.38	0.74	0.90
Mg	0.87	1.8	2.0	2.8
Al	0.18	0.31	0.30	0.28
Si	1.1	2.2	2.5	3.7
Fe	0.11	0.43	0.30	0.65
C	4.8	12.0	5.8	18.0
$logf_{O_2}$	−12.6	−11.5	−11.7	−9.5
ΔQFM	−2.3	−2.0	−2.1	−2.1
pH	5.39	5.41	5.21	5.23
a_{H_2O}	0.86	0.78	0.84	0.71

APPENDIX D

$$H_2O + CO_{2,aq} = H_2CO_{3,aq}$$

Name	ΔG_f^o cal mol^{-1}	ΔH_f^o cal mol^{-1}	S^o cal mol^{-1} K^{-1}	V^o cm^3 mol^{-1}	C_p cal mol^{-1} K^{-1}	$a_1 \times 10$ cal mol^{-1} bar^{-1}	$a_2 \times 10^{-2}$ cal mol^{-1}	a_3 cal K mol^{-1} bar^{-1}	$a_4 \times 10^{-4}$ cal K mol^{-1}	c_1 cal mol^{-1} K^{-1}	$c_2 \times 10^{-4}$ cal K mol^{-1}	$\omega \times 10^{-5}$ cal mol^{-1}	Z
$CO_{2.aq}$	−92250	−98900	28.100	32.8	52.1	7.7900	3.1400	2.2100	−2.9100	37.0000	6.5000	−0.2000	0
$H_2CO_{3,aq}$	−145400	−164229	43.000	46.0	86.5	10.3102	5.5332	0.1986	−3.0077	54.0971	14.5855	−0.3000	0

Log K		**Pressure (GPa)**									
		1.0	**1.5**	**2.0**	**2.5**	**3.0**	**3.5**	**4.0**	**4.5**	**5.0**	**5.5**	**6.0**
Temperature (°C)	**300**	−0.76	−0.55	−0.37	−0.21	−0.07	0.05	0.16	0.26	0.34	0.42	0.48
	350	−0.64	−0.44	−0.26	−0.11	0.02	0.14	0.25	0.34	0.42	0.49	0.55
	400	−0.54	−0.34	−0.17	−0.02	0.11	0.22	0.32	0.41	0.49	0.56	0.62
	450	−0.45	−0.25	−0.08	0.06	0.19	0.30	0.39	0.48	0.56	0.63	0.69
	500	−0.36	−0.17	−0.01	0.13	0.26	0.37	0.46	0.55	0.62	0.69	0.75
	550	−0.28	−0.09	0.07	0.21	0.33	0.43	0.53	0.61	0.69	0.75	0.82
	600	−0.20	−0.02	0.14	0.27	0.39	0.50	0.59	0.67	0.75	0.81	0.88
	650	−0.13	0.05	0.21	0.34	0.46	0.56	0.65	0.74	0.81	0.88	0.93
	700	−0.07	0.11	0.26	0.40	0.51	0.62	0.71	0.79	0.87	0.93	0.99
	750	−0.01	0.17	0.32	0.45	0.57	0.67	0.76	0.84	0.92	0.98	1.04
	800	0.04	0.22	0.37	0.50	0.62	0.71	0.81	0.89	0.96	1.03	1.08
	850	0.09	0.27	0.42	0.55	0.66	0.76	0.85	0.93	1.01	1.07	1.13
	900	0.15	0.32	0.47	0.59	0.71	0.81	0.89	0.97	1.04	1.10	1.17
	950	0.19	0.37	0.51	0.64	0.75	0.85	0.93	1.01	1.08	1.15	1.21
	1000	0.24	0.41	0.56	0.68	0.79	0.89	0.98	1.05	1.12	1.19	1.25
	1050	0.29	0.46	0.60	0.73	0.84	0.93	1.02	1.10	1.17	1.23	1.29
	1100	0.34	0.51	0.65	0.78	0.89	0.98	1.07	1.14	1.22	1.28	1.34

$$AlO_2(SiO_2)^- + 4H^+ = Al^{3+} + 2H_2O + SiO_{2,aq} \text{ (Dehydrated)}$$

$$Al(OH)_3OSi(OH)_3^- + 4H^+ = Al^{3+} + 3H_2O + Si(OH)_4^0 \text{ (Hydrated)}$$

Name	ΔG_f^o cal mol^{-1}	ΔH_f^o cal mol^{-1}	S^o cal mol^{-1} K^{-1}	V^o cm^3 mol^{-1}	C_p cal mol^{-1} K^{-1}	$a_1 \times 10$ cal mol^{-1} bar^{-1}	$a_2 \times 10^{-2}$ cal mol^{-1}	a_3 cal K mol^{-1} bar^{-1}	$a_4 \times 10^{-4}$ cal K mol^{-1}	c_1 cal mol^{-1} K^{-1}	$c_2 \times 10^{-4}$ cal K mol^{-1}	$\omega \times 10^{-5}$ cal mol^{-1}	Z
$AlO_2(SiO_2)^-$	−403500	−440456	4.000	34.8	32.0	9.0313	4.3155	1.2196	−2.9574	39.3711	3.4838	1.5685	−1
H+	0	0	0.000	0.0	0.0	0.0000	0.0000	0.0000	0.0000	0.0000	0.0000	0.0000	1
Al^{3+}	−115609	−126834	−77.700	−44.4	−31.0	−3.3802	−17.0071	14.5185	−2.0758	10.7000	−8.0600	2.7530	3
$SiO_{2,aq}$	−199557	−213937	5.300	18.0	27.7	4.8998	1.4090	4.4066	−2.8372	25.7171	2.6079	0.3600	0

Log K		Pressure (GPa)										
		1.0	1.5	2.0	2.5	3.0	3.5	4.0	4.5	5.0	5.5	6.0
Temperature (°C)	300	6.7755	7.0691	7.3339	7.5954	7.8631	8.1410	8.4305	8.7324	9.0465	9.3726	9.7103
	350	5.7063	5.9889	6.2397	6.4856	6.7363	6.9961	7.2664	7.5478	7.8405	8.1441	8.4583
	400	4.8132	5.0873	5.3255	5.5567	5.7915	6.0341	6.2863	6.5486	6.8213	7.1040	7.3966
	450	4.0557	4.3244	4.5518	4.7699	4.9900	5.2168	5.4522	5.6970	5.9512	6.2148	6.4876
	500	3.4027	3.6690	3.8875	4.0940	4.3009	4.5134	4.7335	4.9621	5.1995	5.4457	5.7003
	550	2.8304	3.0975	3.3090	3.5054	3.7005	3.8999	4.1060	4.3200	4.5420	4.7722	5.0103
	600	2.3236	2.5943	2.8007	2.9885	3.1732	3.3609	3.5545	3.7551	3.9632	4.1789	4.4019
	650	1.8732	2.1504	2.3534	2.5342	2.7098	2.8872	3.0696	3.2583	3.4538	3.6563	3.8658
	700	1.4715	1.7577	1.9591	2.1342	2.3020	2.4704	2.6427	2.8207	3.0049	3.1956	3.3929
	750	1.1111	1.4085	1.6097	1.7803	1.9415	2.1020	2.2654	2.4338	2.6078	2.7879	2.9740
	800	0.7850	1.0955	1.2978	1.4651	1.6207	1.7741	1.9297	2.0894	2.2542	2.4246	2.6007
	850	0.4871	0.8122	1.0167	1.1815	1.3323	1.4797	1.6282	1.7801	1.9367	2.0984	2.2653
	900	0.2118	0.5528	0.7603	0.9234	1.0703	1.2123	1.3545	1.4995	1.6486	1.8023	1.9610
	950	−0.0455	0.3122	0.5233	0.6855	0.8291	0.9664	1.1030	1.2417	1.3840	1.5304	1.6815
	1000	−0.2890	0.0857	0.3011	0.4628	0.6036	0.7368	0.8684	1.0015	1.1376	1.2774	1.4215
	1050	−0.5224	−0.1304	0.0895	0.2512	0.3897	0.5192	0.6463	0.7742	0.9047	1.0385	1.1763
	1100	−0.7487	−0.3399	−0.1152	0.0467	0.1833	0.3096	0.4326	0.5559	0.6811	0.8094	0.9413

$$Ca(HCO_3)^+ = Ca^{2+} + HCO_3^-$$

Name	ΔG_f^o cal mol^{-1}	ΔH_f^o cal mol^{-1}	S^o cal mol^{-1} K^{-1}	V^o cm^3 mol^{-1}	C_p cal mol^{-1} K^{-1}	$a_1 \times 10$ cal mol^{-1} bar^{-1}	$a_2 \times 10^{-2}$ cal mol^{-1}	a_3 cal K mol^{-1} bar^{-1}	$a_4 \times 10^{-4}$ cal K mol^{-1}	c_1 cal mol^{-1} K^{-1}	$c_2 \times 10^{-4}$ cal K mol^{-1}	$\omega \times 10^{-5}$ cal mol^{-1}	Z
$Ca(HCO_3)^+$	−273830	−294350	26.000	30.0	51.0	7.4225	2.7838	2.5039	−2.8941	37.5110	7.3541	0.1580	1
Ca^{2+}	−132120	−129800	−13.500	−18.4	−7.5	−0.2450	−7.2520	5.0000	−2.4800	9.0000	−2.5200	1.2366	2
HCO_3^-	−140282	−164898	23.530	24.2	−8.5	7.6500	0.9200	0.6000	−2.8200	11.0000	−3.8000	1.2733	−1

Log K		Pressure (GPa)										
		1.0	1.5	2.0	2.5	3.0	3.5	4.0	4.5	5.0	5.5	6.0
Temperature (°C)	300	−2.3759	−2.0530	−1.8281	−1.6579	−1.5224	−1.4110	−1.3172	−1.2367	−1.1668	−1.1053	−1.0508
	350	−2.8085	−2.4675	−2.2332	−2.0572	−1.9177	−1.8031	−1.7066	−1.6238	−1.5518	−1.4883	−1.4319
	400	−3.2262	−2.8637	−2.6185	−2.4358	−2.2917	−2.1737	−2.0745	−1.9895	−1.9154	−1.8502	−1.7921
	450	−3.6323	−3.2449	−2.9873	−2.7971	−2.6479	−2.5262	−2.4242	−2.3368	−2.2607	−2.1938	−2.1341
	500	−4.0291	−3.6137	−3.3422	−3.1437	−2.9890	−2.8633	−2.7582	−2.6684	−2.5903	−2.5215	−2.4603
	550	−4.4185	−3.9721	−3.6855	−3.4780	−3.3173	−3.1873	−3.0789	−2.9864	−2.9062	−2.8356	−2.7728
	600	−4.8018	−4.3218	−4.0189	−3.8017	−3.6346	−3.5000	−3.3880	−3.2928	−3.2103	−3.1378	−3.0734
	650	−5.1800	−4.6640	−4.3437	−4.1163	−3.9423	−3.8029	−3.6873	−3.5891	−3.5043	−3.4298	−3.3637
	700	−5.5537	−4.9995	−4.6610	−4.4229	−4.2418	−4.0973	−3.9779	−3.8767	−3.7894	−3.7129	−3.6451
	750	−5.9232	−5.3292	−4.9718	−4.7225	−4.5342	−4.3843	−4.2609	−4.1567	−4.0668	−3.9882	−3.9186
	800	−6.2888	−5.6536	−5.2767	−5.0161	−4.8201	−4.6649	−4.5374	−4.4300	−4.3375	−4.2567	−4.1852
	850	−6.6504	−5.9730	−5.5764	−5.3041	−5.1005	−4.9398	−4.8082	−4.6974	−4.6023	−4.5193	−4.4460
	900	−7.0079	−6.2879	−5.8712	−5.5873	−5.3759	−5.2096	−5.0738	−4.9598	−4.8620	−4.7768	−4.7015
	950	−7.3609	−6.5982	−6.1616	−5.8659	−5.6468	−5.4750	−5.3350	−5.2176	−5.1172	−5.0297	−4.9525
	1000	−7.7090	−6.9041	−6.4477	−6.1404	−5.9137	−5.7364	−5.5922	−5.4715	−5.3684	−5.2787	−5.1996
	1050	−8.0518	−7.2056	−6.7298	−6.4111	−6.1768	−5.9941	−5.8458	−5.7219	−5.6161	−5.5242	−5.4433
	1100	−8.3888	−7.5025	−7.0079	−6.6782	−6.4366	−6.2486	−6.0963	−5.9692	−5.8608	−5.7668	−5.6840

$$Ca(HCOO)^- = Ca^{2+} + HCOO^-$$

Name	ΔG_f^o cal mol^{-1}	ΔH_f^o cal mol^{-1}	S^o cal mol^{-1} K^{-1}	V^o cm^3 mol^{-1}	C_p cal mol^{-1} K^{-1}	$a_1 \times 10$ cal mol^{-1} bar^{-1}	$a_2 \times 10^{-2}$ cal mol^{-1}	a_3 cal K mol^{-1} bar^{-1}	$a_4 \times 10^{-4}$ cal K mol^{-1}	c_1 cal mol^{-1} K^{-1}	$c_2 \times 10^{-4}$ cal K mol^{-1}	$\omega \times 10^{-5}$ cal mol^{-1}	Z
Ca $(HCOO)^+$	−217930	−232236	11.000	17.5	68.0	5.1038	0.5762	4.3550	−2.8028	49.5668	10.8170	0.3851	1
Ca^{2+}	−132120	−129800	−13.500	−18.4	−7.5	−0.2450	−7.2520	5.0000	−2.4800	9.0000	−2.5200	1.2366	2
$HCOO^-$	−83862	−101680	21.700	26.2	−20.2	5.2684	7.6836	3.4706	−3.0966	17.0000	−12.4000	1.3003	−1

Log K		**Pressure (GPa)**										
		1.0	**1.5**	**2.0**	**2.5**	**3.0**	**3.5**	**4.0**	**4.5**	**5.0**	**5.5**	**6.0**
Temperature (°C)	**300**	−2.2837	−2.0854	−1.9511	−1.8514	−1.7733	−1.7099	−1.6571	−1.6123	−1.5737	−1.5400	−1.5104
	350	−2.6295	−2.4063	−2.2570	−2.1468	−2.0606	−1.9905	−1.9318	−1.8819	−1.8385	−1.8005	−1.7668
	400	−2.9801	−2.7302	−2.5657	−2.4451	−2.3511	−2.2748	−2.2110	−2.1565	−2.1091	−2.0674	−2.0303
	450	−3.3338	−3.0552	−2.8748	−2.7438	−2.6422	−2.5599	−2.4912	−2.4325	−2.3816	−2.3366	−2.2966
	500	−3.6893	−3.3799	−3.1830	−3.0414	−2.9321	−2.8440	−2.7706	−2.7080	−2.6536	−2.6057	−2.5630
	550	−4.0458	−3.7036	−3.4895	−3.3370	−3.2201	−3.1261	−3.0481	−2.9817	−2.9241	−2.8734	−2.8281
	600	−4.4028	−4.0259	−3.7939	−3.6302	−3.5056	−3.4058	−3.3232	−3.2530	−3.1922	−3.1388	−3.0912
	650	−4.7597	−4.3464	−4.0960	−3.9209	−3.7883	−3.6827	−3.5955	−3.5216	−3.4577	−3.4016	−3.3516
	700	−5.1162	−4.6648	−4.3955	−4.2088	−4.0682	−3.9567	−3.8649	−3.7873	−3.7203	−3.6616	−3.6094
	750	−5.4718	−4.9811	−4.6924	−4.4939	−4.3453	−4.2278	−4.1315	−4.0502	−3.9802	−3.9188	−3.8644
	800	−5.8259	−5.2951	−4.9867	−4.7763	−4.6196	−4.4962	−4.3952	−4.3103	−4.2372	−4.1733	−4.1167
	850	−6.1782	−5.6065	−5.2783	−5.0560	−4.8912	−4.7619	−4.6564	−4.5677	−4.4917	−4.4252	−4.3664
	900	−6.5281	−5.9153	−5.5673	−5.3331	−5.1602	−5.0250	−4.9149	−4.8227	−4.7436	−4.6747	−4.6137
	950	−6.8750	−6.2212	−5.8535	−5.6075	−5.4266	−5.2856	−5.1711	−5.0753	−4.9933	−4.9219	−4.8588
	1000	−7.2182	−6.5240	−6.1369	−5.8793	−5.6906	−5.5439	−5.4250	−5.3256	−5.2408	−5.1669	−5.1017
	1050	−7.5572	−6.8236	−6.4176	−6.1486	−5.9523	−5.7999	−5.6767	−5.5740	−5.4863	−5.4101	−5.3428
	1100	−7.8913	−7.1196	−6.6953	−6.4153	−6.2116	−6.0538	−5.9265	−5.8204	−5.7299	−5.6514	−5.5822

$$Ca(HSiO_3)^+ + H^+ = Ca^{2+} + H_2O + SiO_{2,aq}(\text{Dehydrated})$$

$$CaOSi(OH)_3^+ + H^+ = Ca^{2+} + Si(OH)_4^0(\text{Hydrated})$$

Name	ΔG_f^o cal mol^{-1}	ΔH_f^o cal mol^{-1}	S^o cal mol^{-1} K^{-1}	V^o cm^3 mol^{-1}	C_p cal mol^{-1} K^{-1}	$a_1 \times 10$ cal mol^{-1} bar^{-1}	$a_2 \times 10^{-2}$ cal mol^{-1}	a_3 cal K mol^{-1} bar^{-1}	$a_4 \times 10^{-4}$ cal K mol^{-1}	c_1 cal mol^{-1} K^{-1}	$c_2 \times 10^{-4}$ cal K mol^{-1}	$\omega \times 10^{-5}$ cal mol^{-1}	Z
Ca $(HSiO_3)^+$	−376299	−397525	16.800	36.0	72.0	8.6546	3.9569	1.5203	−2.9426	51.1018	11.6318	0.2973	1
H^+	0	0	0.000	0.0	0.0	0.0000	0.0000	0.0000	0.0000	0.0000	0.0000	0.0000	1
Ca^{2+}	−132120	−129800	−13.500	−18.4	−7.5	−0.2450	−7.2520	5.0000	−2.4800	9.0000	−2.5200	1.2366	2
$SiO_{2,aq}$	−199557	−213937	5.300	18.0	27.7	4.8998	1.4090	4.4066	−2.8372	25.7171	2.6079	0.3600	0

Log K		Pressure (GPa)										
		1.0	**1.5**	**2.0**	**2.5**	**3.0**	**3.5**	**4.0**	**4.5**	**5.0**	**5.5**	**6.0**
Temperature (°C)	**300**	4.0349	4.2842	4.5034	4.7123	4.9191	5.1273	5.3388	5.5545	5.7747	5.9998	6.2296
	350	3.4426	3.6865	3.8965	4.0945	4.2890	4.4841	4.6817	4.8828	5.0878	5.2970	5.5104
	400	2.9219	3.1635	3.3663	3.5548	3.7387	3.9222	4.1074	4.2954	4.4869	4.6820	4.8809
	450	2.4570	2.6990	2.8964	3.0772	3.2519	3.4252	3.5994	3.7760	3.9554	4.1380	4.3240
	500	2.0351	2.2803	2.4742	2.6486	2.8154	2.9798	3.1444	3.3107	3.4794	3.6509	3.8254
	550	1.6468	1.8976	2.0896	2.2589	2.4190	2.5756	2.7318	2.8890	3.0481	3.2097	3.3738
	600	1.2860	1.5448	1.7363	1.9018	2.0562	2.2062	2.3549	2.5040	2.6547	2.8073	2.9623
	650	0.9494	1.2185	1.4107	1.5735	1.7234	1.8676	2.0098	2.1519	2.2950	2.4398	2.5865
	700	0.6344	0.9155	1.1098	1.2708	1.4170	1.5563	1.6929	1.8288	1.9653	2.1030	2.2424
	750	0.3379	0.6326	0.8300	0.9901	1.1334	1.2687	1.4004	1.5308	1.6614	1.7929	1.9257
	800	0.0571	0.3669	0.5683	0.7282	0.8692	1.0011	1.1286	1.2542	1.3795	1.5054	1.6324
	850	−0.2105	0.1154	0.3214	0.4818	0.6212	0.7502	0.8740	0.9955	1.1161	1.2370	1.3587
	900	−0.4671	−0.1244	0.0869	0.2482	0.3865	0.5132	0.6338	0.7515	0.8680	0.9844	1.1014
	950	−0.7148	−0.3547	−0.1378	0.0249	0.1625	0.2872	0.4051	0.5195	0.6323	0.7447	0.8573
	1000	−0.9552	−0.5776	−0.3547	−0.1903	−0.0532	0.0699	0.1855	0.2970	0.4065	0.5152	0.6239
	1050	−1.1898	−0.7948	−0.5659	−0.3996	−0.2626	−0.1407	−0.0273	0.0817	0.1882	0.2936	0.3988
	1100	−1.4199	−1.0079	−0.7729	−0.6046	−0.4675	−0.3468	−0.2351	−0.1285	−0.0247	0.0778	0.1797

$$\boldsymbol{Fe(HCOO)^{-} = Fe^{2+} + HCOO^{-}}$$

Name	ΔG_f^o cal mol^{-1}	ΔH_f^o cal mol^{-1}	S^o cal mol^{-1} K^{-1}	V^o cm^3 mol^{-1}	C_p cal mol^{-1} K^{-1}	$a_1 \times 10$ cal mol^{-1} bar^{-1}	$a_2 \times 10^{-2}$ cal mol^{-1}	a_3 cal K mol^{-1} bar^{-1}	$a_4 \times 10^{-4}$ cal K mol^{-1}	c_1 cal mol^{-1} K^{-1}	$c_2 \times 10^{-4}$ cal K mol^{-1}	$\omega \times 10^{-5}$ cal mol^{-1}	Z
$Fe(HCOO)^+$	−111800	−112263	59.000	27.0	30.0	6.6001	2.0008	3.1604	−2.8617	20.5995	3.0764	−0.3418	1
Fe^{2+}	−21870	−22050	−25.300	−22.2	−7.9	−1.0416	−9.0072	9.6653	−2.4066	14.9634	−4.6439	1.4574	2
$HCOO^-$	−83862	−101680	21.700	26.2	−20.2	5.2684	7.6836	3.4706	−3.0966	17.0000	−12.4000	1.3003	−1

Log K		Pressure (GPa)										
		1.0	**1.5**	**2.0**	**2.5**	**3.0**	**3.5**	**4.0**	**4.5**	**5.0**	**5.5**	**6.0**
Temperature (°C)	**300**	−7.5354	−6.8068	−6.1790	−5.6063	−5.0682	−4.5537	−4.0564	−3.5720	−3.0977	−2.6315	−2.1719
	350	−8.0638	−7.3317	−6.7142	−6.1578	−5.6393	−5.1462	−4.6715	−4.2105	−3.7602	−3.3185	−2.8837
	400	−8.5359	−7.7935	−7.1817	−6.6378	−6.1353	−5.6604	−5.2051	−4.7645	−4.3352	−3.9150	−3.5020
	450	−8.9660	−8.2070	−7.5966	−7.0618	−6.5721	−6.1123	−5.6736	−5.2506	−4.8396	−4.4381	−4.0442
	500	−9.3647	−8.5832	−7.9705	−7.4415	−6.9619	−6.5146	−6.0899	−5.6820	−5.2868	−4.9017	−4.5246
	550	−9.7397	−8.9304	−8.3119	−7.7860	−7.3140	−6.8769	−6.4641	−6.0690	−5.6875	−5.3166	−4.9542
	600	−10.0968	−9.2547	−8.6275	−8.1024	−7.6358	−7.2068	−6.8039	−6.4199	−6.0502	−5.6918	−5.3423
	650	−10.4400	−9.5610	−8.9225	−8.3960	−7.9330	−7.5105	−7.1157	−6.7411	−6.3817	−6.0341	−5.6959
	700	−10.7726	−9.8529	−9.2008	−8.6712	−8.2102	−7.7926	−7.4045	−7.0379	−6.6873	−6.3492	−6.0209
	750	−11.0966	−10.1331	−9.4656	−8.9313	−8.4709	−8.0569	−7.6744	−7.3145	−6.9716	−6.6417	−6.3222
	800	−11.4137	−10.4037	−9.7193	−9.1791	−8.7182	−8.3067	−7.9286	−7.5744	−7.2380	−6.9154	−6.6036
	850	−11.7246	−10.6664	−9.9638	−9.4167	−8.9543	−8.5444	−8.1698	−7.8204	−7.4897	−7.1733	−6.8684
	900	−12.0299	−10.9223	−10.2007	−9.6458	−9.1812	−8.7721	−8.4002	−8.0548	−7.7289	−7.4182	−7.1193
	950	−12.3299	−11.1722	−10.4311	−9.8679	−9.4004	−8.9914	−8.6216	−8.2795	−7.9579	−7.6520	−7.3585
	1000	−12.6245	−11.4168	−10.6559	−10.0840	−9.6131	−9.2038	−8.8356	−8.4962	−8.1783	−7.8767	−7.5880
	1050	−12.9133	−11.6565	−10.8758	−10.2950	−9.8204	−9.4105	−9.0433	−8.7063	−8.3915	−8.0937	−7.8093
	1100	−13.1959	−11.8914	−11.0913	−10.5016	−10.0232	−9.6122	−9.2458	−8.9108	−8.5988	−8.3044	−8.0238

$Fe(HSiO_3)^+ + H^+ = Fe^{2+} + H_2O + SiO_{2,aq}$(Dehydrated)

$FeOSi(OH)_3^+ + H^+ = Fe^{2+} + Si(OH)_4^0$(Hydrated)

Name	ΔG_f^o cal mol^{-1}	ΔH_f^o cal mol^{-1}	S^o cal mol^{-1} K^{-1}	V^o cm^3 mol^{-1}	C_p cal mol^{-1} K^{-1}	$a_1 \times 10$ cal mol^{-1} bar^{-1}	$a_2 \times 10^{-2}$ cal mol^{-1}	a_3 cal K mol^{-1} bar^{-1}	$a_4 \times 10^{-4}$ cal K mol^{-1}	c_1 cal mol^{-1} K^{-1}	$c_2 \times 10^{-4}$ cal K mol^{-1}	$\omega \times 10^{-5}$ cal mol^{-1}	Z
$Fe(HSiO_3)^+$	−277500	−298539	14.000	38.2	77.0	9.1022	4.3830	1.1630	−2.9602	54.4228	12.6503	0.3397	1
H^+	0	0	0.000	0.0	0.0	0.0000	0.0000	0.0000	0.0000	0.0000	0.0000	0.0000	1
Fe^{2+}	−21870	−22050	−25.300	−22.2	−7.9	−1.0416	−9.0072	9.6653	−2.4066	14.9634	−4.6439	1.4574	2
$SiO_{2,aq}$	−199557	−213937	5.300	18.0	27.7	4.8998	1.4090	4.4066	−2.8372	25.7171	2.6079	0.3600	0

Log K		**Pressure (GPa)**										
		1.0	**1.5**	**2.0**	**2.5**	**3.0**	**3.5**	**4.0**	**4.5**	**5.0**	**5.5**	**6.0**
Temperature (°C)	**300**	−0.6883	−0.1859	0.2744	0.7177	1.1544	1.5894	2.0253	2.4637	2.9053	3.3506	3.7997
	350	−1.0422	−0.5589	−0.1219	0.2962	0.7065	1.1142	1.5222	1.9318	2.3441	2.7595	3.1782
	400	−1.3600	−0.8911	−0.4737	−0.0775	0.3094	0.6929	1.0758	1.4599	1.8460	2.2347	2.6263
	450	−1.6503	−1.1911	−0.7899	−0.4127	−0.0462	0.3158	0.6765	1.0378	1.4006	1.7656	2.1330
	500	−1.9201	−1.4664	−1.0784	−0.7174	−0.3688	−0.0257	0.3153	0.6563	0.9984	1.3421	1.6880
	550	−2.1751	−1.7231	−1.3454	−0.9982	−0.6652	−0.3388	−0.0152	0.3077	0.6311	0.9559	1.2824
	600	−2.4180	−1.9642	−1.5944	−1.2588	−0.9393	−0.6277	−0.3196	−0.0128	0.2940	0.6018	0.9110
	650	−2.6498	−2.1910	−1.8268	−1.5009	−1.1931	−0.8943	−0.6000	−0.3076	−0.0155	0.2770	0.5707
	700	−2.8712	−2.4047	−2.0441	−1.7261	−1.4284	−1.1409	−0.8588	−0.5792	−0.3004	−0.0215	0.2582
	750	−3.0837	−2.6071	−2.2484	−1.9368	−1.6477	−1.3702	−1.0989	−0.8306	−0.5638	−0.2971	−0.0300
	800	−3.2887	−2.8000	−2.4417	−2.1352	−1.8535	−1.5848	−1.3231	−1.0651	−0.8089	−0.5533	−0.2976
	850	−3.4878	−2.9852	−2.6262	−2.3237	−2.0483	−1.7873	−1.5341	−1.2854	−1.0389	−0.7933	−0.5479
	900	−3.6822	−3.1646	−2.8038	−2.5044	−2.2344	−1.9801	−1.7347	−1.4942	−1.2564	−1.0199	−0.7839
	950	−3.8732	−3.3397	−2.9763	−2.6791	−2.4138	−2.1655	−1.9269	−1.6939	−1.4640	−1.2358	−1.0084
	1000	−4.0617	−3.5118	−3.1452	−2.8497	−2.5883	−2.3454	−2.1130	−1.8867	−1.6641	−1.4434	−1.2238
	1050	−4.2487	−3.6823	−3.3121	−3.0177	−2.7598	−2.5216	−2.2947	−2.0746	−1.8586	−1.6449	−1.4325
	1100	−4.4349	−3.8523	−3.4783	−3.1846	−2.9297	−2.6957	−2.4739	−2.2595	−2.0495	−1.8421	−1.6363

$H_2O + SiO_{2,aq} = HSiO_3^- + H^+$(Dehydrated)

$Si(OH)_4^0 = SiO(OH)_3^- + H^+$(Hydrated)

Name	ΔG_f^o cal mol^{-1}	ΔH_f^o cal mol^{-1}	S^o cal mol^{-1} K^{-1}	V^o cm^3 mol^{-1}	C_p cal mol^{-1} K^{-1}	$a_1 \times 10$ cal mol^{-1} bar^{-1}	$a_2 \times 10^{-2}$ cal mol^{-1}	a_3 cal K mol^{-1} bar^{-1}	$a_4 \times 10^{-4}$ cal K mol^{-1}	c_1 cal mol^{-1} K^{-1}	$c_2 \times 10^{-4}$ cal K mol^{-1}	$\omega \times 10^{-5}$ cal mol^{-1}	Z
$SiO_{2,aq}$	−199557	−213937	5.300	18.0	27.7	4.8998	1.4090	4.4066	−2.8372	25.7171	2.6079	0.3600	0
H^+	0	0	0.000	0.0	0.0	0.0000	0.0000	0.0000	0.0000	0.0000	0.0000	0.0000	1
$HSiO_3^-$	−242855	−276479	−3.500	21.2	16.0	6.4445	1.8526	3.2847	−2.8556	31.0405	0.2246	1.6821	−1

Log K		Pressure (GPa)										
		1.0	1.5	2.0	2.5	3.0	3.5	4.0	4.5	5.0	5.5	6.0
Temperature (°C)	300	−7.0651	−6.5194	−6.0500	−5.6297	−5.2448	−4.8874	−4.5521	−4.2355	−3.9348	−3.6481	−3.3737
	350	−7.0895	−6.5510	−6.0949	−5.6902	−5.3217	−4.9808	−4.6620	−4.3615	−4.0766	−3.8052	−3.5457
	400	−7.1389	−6.6023	−6.1553	−5.7623	−5.4068	−5.0792	−4.7739	−4.4867	−4.2149	−3.9563	−3.7093
	450	−7.2076	−6.6684	−6.2271	−5.8429	−5.4975	−5.1808	−4.8864	−4.6102	−4.3493	−4.1015	−3.8650
	500	−7.2908	−6.7452	−6.3067	−5.9289	−5.5914	−5.2833	−4.9979	−4.7309	−4.4791	−4.2403	−4.0127
	550	−7.3846	−6.8294	−6.3914	−6.0178	−5.6864	−5.3852	−5.1072	−4.8477	−4.6035	−4.3723	−4.1522
	600	−7.4874	−6.9198	−6.4803	−6.1094	−5.7825	−5.4869	−5.2149	−4.9617	−4.7240	−4.4992	−4.2855
	650	−7.5992	−7.0169	−6.5744	−6.2048	−5.8813	−5.5901	−5.3231	−5.0752	−4.8429	−4.6236	−4.4155
	700	−7.7196	−7.1207	−6.6738	−6.3045	−5.9834	−5.6957	−5.4328	−5.1894	−4.9618	−4.7473	−4.5440
	750	−7.8476	−7.2305	−6.7782	−6.4082	−6.0887	−5.8037	−5.5442	−5.3046	−5.0810	−4.8706	−4.6715
	800	−7.9816	−7.3449	−6.8864	−6.5150	−6.1963	−5.9135	−5.6568	−5.4204	−5.2002	−4.9934	−4.7980
	850	−8.1200	−7.4627	−6.9972	−6.6239	−6.3056	−6.0243	−5.7699	−5.5362	−5.3190	−5.1153	−4.9230
	900	−8.2609	−7.5825	−7.1095	−6.7338	−6.4153	−6.1351	−5.8826	−5.6512	−5.4365	−5.2356	−5.0462
	950	−8.4027	−7.7029	−7.2221	−6.8435	−6.5246	−6.2452	−5.9941	−5.7647	−5.5522	−5.3537	−5.1668
	1000	−8.5437	−7.8224	−7.3337	−6.9520	−6.6324	−6.3534	−6.1036	−5.8758	−5.6653	−5.4689	−5.2842
	1050	−8.6823	−7.9399	−7.4432	−7.0583	−6.7377	−6.4590	−6.2101	−5.9837	−5.7749	−5.5804	−5.3977
	1100	−8.8171	−8.0541	−7.5494	−7.1613	−6.8396	−6.5610	−6.3129	−6.0877	−5.8804	−5.6876	−5.5067

$$MgO_{aq} + 2H^{+} = Mg^{2+} + H_2O(\text{Dehydrated})$$

$$Mg(OH)_{2,aq} + 2H^{+} = Mg^{2+} + 2H_2O(\text{Hydrated})$$

Name	ΔG_f^o cal mol^{-1}	ΔH_f^o cal mol^{-1}	S^o cal mol^{-1} K^{-1}	V^o cm^3 mol^{-1}	C_p cal mol^{-1} K^{-1}	$a_1 \times 10$ cal mol^{-1} bar^{-1}	$a_2 \times 10^{-2}$ cal mol^{-1}	a_3 cal K mol^{-1} bar^{-1}	$a_4 \times 10^{-4}$ cal K mol^{-1}	c_1 cal mol^{-1} K^{-1}	$c_2 \times 10^{-4}$ cal K mol^{-1}	$\omega \times 10^{-5}$ cal mol^{-1}	Z
MgO_{aq}	−137500	−139804	24.600	6.2	−24.5	2.8684	−1.5521	6.1396	−2.7148	−5.4281	−8.0253	0.3000	0
H^+	0	0	0.000	0.0	0.0	0.0000	0.0000	0.0000	0.0000	0.0000	0.0000	0.0000	1
Mg^{2+}	−108505	−111367	−33.000	−21.5	−5.3	−0.8217	−8.5990	8.3900	−2.3900	20.8000	−5.8920	1.5372	2

Log K		Pressure (GPa)										
		1.0	1.5	2.0	2.5	3.0	3.5	4.0	4.5	5.0	5.5	6.0
Temperature (°C)	300	8.2759	8.4466	8.6002	8.7515	8.9056	9.0647	9.2298	9.4012	9.5788	9.7626	9.9523
	350	7.3682	7.5362	7.6825	7.8240	7.9667	8.1132	8.2647	8.4216	8.5840	8.7518	8.9249
	400	6.6368	6.8051	6.9462	7.0798	7.2132	7.3492	7.4892	7.6339	7.7833	7.9376	8.0966
	450	6.0398	6.2110	6.3489	6.4764	6.6020	6.7292	6.8595	6.9937	7.1321	7.2748	7.4217
	500	5.5461	5.7227	5.8589	5.9818	6.1011	6.2207	6.3427	6.4679	6.5967	6.7294	6.8659
	550	5.1325	5.3166	5.4527	5.5722	5.6863	5.7996	5.9144	6.0318	6.1523	6.2761	6.4034
	600	4.7827	4.9766	5.1137	5.2310	5.3409	5.4489	5.5575	5.6681	5.7814	5.8975	6.0167
	650	4.4859	4.6913	4.8308	4.9467	5.0534	5.1570	5.2605	5.3652	5.4721	5.5815	5.6936
	700	4.2333	4.4519	4.5948	4.7103	4.8146	4.9146	5.0136	5.1133	5.2146	5.3181	5.4240
	750	4.0173	4.2505	4.3977	4.5135	4.6161	4.7131	4.8084	4.9038	5.0003	5.0986	5.1990
	800	3.8315	4.0804	4.2327	4.3494	4.4509	4.5456	4.6377	4.7293	4.8217	4.9154	5.0109
	850	3.6704	3.9360	4.0939	4.2121	4.3129	4.4059	4.4953	4.5837	4.6723	4.7620	4.8531
	900	3.5294	3.8124	3.9763	4.0964	4.1971	4.2886	4.3758	4.4614	4.5468	4.6329	4.7202
	950	3.4047	3.7054	3.8758	3.9981	4.0989	4.1894	4.2748	4.3579	4.4405	4.5233	4.6071
	1000	3.2932	3.6116	3.7886	3.9134	4.0147	4.1043	4.1882	4.2692	4.3492	4.4293	4.5100
	1050	3.1919	3.5280	3.7116	3.8391	3.9410	4.0301	4.1126	4.1919	4.2697	4.3472	4.4251
	1100	3.0988	3.4520	3.6422	3.7724	3.8750	3.9638	4.0453	4.1229	4.1987	4.2739	4.3493

$$Mg(SiO_2)HCO_3^+ = Mg^{2+} + SiO_{2,aq} + HCO_3^-\text{(Dehydrated)}$$

$$MgOSi(OH)_2(HCO_3)^+ + H_2O = Mg^{2+} + Si(OH)_4^0 + HCO_3^-\text{(Hydrated)}$$

Name	ΔG_f^o cal mol^{-1}	ΔH_f^o cal mol^{-1}	S^o cal mol^{-1} K^{-1}	V^o cm^3 mol^{-1}	C_p cal mol^{-1} K^{-1}	$a_1 \times 10$ cal mol^{-1} bar^{-1}	$a_2 \times 10^{-2}$ cal mol^{-1}	a_3 cal K mol^{-1} bar^{-1}	$a_4 \times 10^{-4}$ cal K mol^{-1}	c_1 cal mol^{-1} K^{-1}	$c_2 \times 10^{-4}$ cal K mol^{-1}	$\omega \times 10^{-5}$ cal mol^{-1}	Z
Mg (SiO_2) HCO_3^+	−454300	−479123	48.000	53.5	78.5	11.8266	6.9770	−1.0120	−3.0674	50.5582	12.9559	−0.1752	1
Mg^{2+}	−108505	−111367	–33.000	−21.5	−5.3	−0.8217	−8.5990	8.3900	−2.3900	20.8000	−5.8920	1.5372	2
$SiO_{2,aq}$	−199557	−213937	5.300	18.0	27.7	4.8998	1.4090	4.4066	−2.8372	25.7171	2.6079	0.3600	0
HCO_3^-	−140282	−164898	23.530	24.2	−8.5	7.6500	0.9200	0.6000	−2.8200	11.0000	−3.8000	1.2733	−1

Log K		**Pressure (GPa)**									
		1.0	**1.5**	**2.0**	**2.5**	**3.0**	**3.5**	**4.0**	**4.5**	**5.0**	**5.5**	**6.0**
Temperature (°C)	**300**	−6.8106	−6.3831	−6.0975	−5.8910	−5.7350	−5.6138	−5.5181	−5.4418	−5.3807	−5.3320	−5.2933
	350	−7.2719	−6.8104	−6.5028	−6.2791	−6.1082	−5.9733	−5.8646	−5.7758	−5.7024	−5.6415	−5.5907
	400	−7.6954	−7.1974	−6.8681	−6.6286	−6.4448	−6.2986	−6.1795	−6.0808	−5.9979	−5.9278	−5.8680
	450	−8.0915	−7.5538	−7.2023	−6.9476	−6.7518	−6.5956	−6.4676	−6.3607	−6.2701	−6.1926	−6.1257
	500	−8.4676	−7.8869	−7.5123	−7.2423	−7.0351	−6.8695	−6.7335	−6.6195	−6.5223	−6.4386	−6.3658
	550	−8.8294	−8.2021	−7.8034	−7.5179	−7.2994	−7.1250	−6.9815	−6.8609	−6.7579	−6.6687	−6.5907
	600	−9.1806	−8.5037	−8.0797	−7.7783	−7.5486	−7.3654	−7.2148	−7.0881	−6.9796	−6.8855	−6.8030
	650	−9.5243	−8.7946	−8.3443	−8.0268	−7.7857	−7.5939	−7.4363	−7.3037	−7.1901	−7.0915	−7.0047
	700	−9.8624	−9.0773	−8.5998	−8.2657	−8.0131	−7.8127	−7.6483	−7.5100	−7.3915	−7.2885	−7.1979
	750	−10.1963	−9.3534	−8.8481	−8.4970	−8.2329	−8.0239	−7.8527	−7.7088	−7.5856	−7.4784	−7.3840
	800	−10.5267	−9.6244	−9.0905	−8.7224	−8.4467	−8.2291	−8.0511	−7.9017	−7.7738	−7.6626	−7.5647
	850	−10.8539	−9.8911	−9.3283	−8.9430	−8.6556	−8.4294	−8.2448	−8.0900	−7.9575	−7.8424	−7.7410
	900	−11.1781	−10.1541	−9.5623	−9.1597	−8.8607	−8.6260	−8.4348	−8.2746	−8.1377	−8.0187	−7.9140
	950	−11.4990	−10.4138	−9.7931	−9.3734	−9.0628	−8.8197	−8.6220	−8.4566	−8.3153	−8.1926	−8.0846
	1000	−11.8160	−10.6704	−10.0212	−9.5846	−9.2626	−9.0113	−8.8071	−8.6366	−8.4910	−8.3647	−8.2535
	1050	−12.1287	−10.9240	−10.2468	−9.7936	−9.4606	−9.2012	−8.9908	−8.8153	−8.6656	−8.5357	−8.4214
	1100	−12.4361	−11.1743	−10.4701	−10.0010	−9.6572	−9.3899	−9.1735	−8.9931	−8.8394	−8.7060	−8.5888

$$NaHCO_{3,aq} = Na^+ + HCO_3^-$$

Name	ΔG_f^o cal mol^{-1}	ΔH_f^o cal mol^{-1}	S^o cal mol^{-1} K^{-1}	V^o cm^3 mol^{-1}	C_p cal mol^{-1} K^{-1}	$a_1 \times 10$ cal mol^{-1} bar^{-1}	$a_2 \times 10^{-2}$ cal mol^{-1}	a_3 cal K mol^{-1} bar^{-1}	$a_4 \times 10^{-4}$ cal K mol^{-1}	c_1 cal mol^{-1} K^{-1}	$c_2 \times 10^{-4}$ cal K mol^{-1}	$\omega \times 10^{-5}$ cal mol^{-1}	Z
$NaHCO_{3,aq}$	−203100	−219552	32.000	39.0	62.0	9.4783	4.7412	0.8627	−2.9750	49.8727	9.5948	0.8000	0
Na^+	−62591	−57433	13.960	−1.1	9.1	1.8390	−2.2850	3.2560	−2.7260	18.1800	−2.9810	0.3306	1
HCO_3^-	−140282	−164898	23.530	24.2	−8.5	7.6500	0.9200	0.6000	−2.8200	11.0000	−3.8000	1.2733	−1

Log K		Pressure (GPa)										
		1.0	**1.5**	**2.0**	**2.5**	**3.0**	**3.5**	**4.0**	**4.5**	**5.0**	**5.5**	**6.0**
Temperature (°C)	**300**	−0.2447	−0.1036	−0.0073	0.0637	0.1183	0.1616	0.1964	0.2249	0.2482	0.2675	0.2834
	350	−0.4925	−0.3472	−0.2485	−0.1758	−0.1196	−0.0747	−0.0382	−0.0081	0.0171	0.0382	0.0560
	400	−0.7403	−0.5894	−0.4879	−0.4133	−0.3555	−0.3092	−0.2714	−0.2399	−0.2134	−0.1908	−0.1716
	450	−0.9867	−0.8289	−0.7240	−0.6472	−0.5878	−0.5402	−0.5011	−0.4685	−0.4408	−0.4172	−0.3968
	500	−1.2307	−1.0648	−0.9560	−0.8768	−0.8157	−0.7667	−0.7265	−0.6928	−0.6641	−0.6395	−0.6181
	550	−1.4720	−1.2968	−1.1835	−1.1017	−1.0388	−0.9884	−0.9470	−0.9122	−0.8826	−0.8571	−0.8349
	600	−1.7102	−1.5247	−1.4065	−1.3218	−1.2569	−1.2051	−1.1625	−1.1267	−1.0962	−1.0699	−1.0469
	650	−1.9451	−1.7484	−1.6249	−1.5371	−1.4702	−1.4168	−1.3730	−1.3362	−1.3048	−1.2776	−1.2539
	700	−2.1768	−1.9679	−1.8389	−1.7478	−1.6786	−1.6237	−1.5786	−1.5408	−1.5085	−1.4805	−1.4561
	750	−2.4050	−2.1834	−2.0485	−1.9540	−1.8825	−1.8259	−1.7795	−1.7407	−1.7075	−1.6788	−1.6536
	800	−2.6298	−2.3949	−2.2539	−2.1558	−2.0820	−2.0237	−1.9760	−1.9361	−1.9020	−1.8725	−1.8467
	850	−2.8511	−2.6026	−2.4552	−2.3535	−2.2773	−2.2172	−2.1682	−2.1272	−2.0922	−2.0619	−2.0354
	900	−3.0688	−2.8063	−2.6526	−2.5472	−2.4685	−2.4067	−2.3564	−2.3143	−2.2784	−2.2474	−2.2202
	950	−3.2828	−3.0064	−2.8462	−2.7371	−2.6560	−2.5924	−2.5407	−2.4976	−2.4608	−2.4290	−2.4011
	1000	−3.4930	−3.2028	−3.0362	−2.9234	−2.8399	−2.7745	−2.7215	−2.6773	−2.6396	−2.6071	−2.5785
	1050	−3.6993	−3.3955	−3.2227	−3.1062	−3.0203	−2.9532	−2.8989	−2.8536	−2.8151	−2.7818	−2.7526
	1100	−3.9015	−3.5846	−3.4057	−3.2856	−3.1974	−3.1286	−3.0730	−3.0267	−2.9873	−2.9533	−2.9235

$\boldsymbol{Si_3O_{6,aq}} = 3\boldsymbol{SiO_{2,aq}}$(Dehydrated)

$\boldsymbol{Si_3O_2(OH)_8^0} + 2\boldsymbol{H_2O} = 3\boldsymbol{Si(OH)_4^0}$(Hydrated)

Name	ΔG_f^o cal mol^{-1}	ΔH_f^o cal mol^{-1}	S^o cal mol^{-1} K^{-1}	V^o cm^3 mol^{-1}	C_p cal mol^{-1} K^{-1}	$a_1 \times 10$ cal mol^{-1} bar^{-1}	$a_2 \times 10^{-2}$ cal mol^{-1}	a_3 cal K mol^{-1} bar^{-1}	$a_4 \times 10^{-4}$ cal K mol^{-1}	c_1 cal mol^{-1} K^{-1}	$c_2 \times 10^{-4}$ cal K mol^{-1}	$\omega \times 10^{-5}$ cal mol^{-1}	Z
$Si_3O_{6,aq}$	−590200	−656130	13.000	67.7	119.0	15.1481	10.1393	−3.6636	−3.1982	85.1208	21.2057	1.0000	0
$SiO_{2,aq}$	−199557	−213937	5.300	18.0	27.7	4.8998	1.4090	4.4066	−2.8372	25.7171	2.6079	0.3600	0

Log K		Pressure (GPa)										
		1.0	**1.5**	**2.0**	**2.5**	**3.0**	**3.5**	**4.0**	**4.5**	**5.0**	**5.5**	**6.0**
Temperature (°C)	**300**	3.3283	3.4228	3.4911	3.5439	3.5865	3.6218	3.6516	3.6773	3.6995	3.7190	3.7362
	350	2.9487	3.0457	3.1185	3.1772	3.2266	3.2693	3.3070	3.3409	3.3718	3.4001	3.4264
	400	2.6109	2.7083	2.7833	2.8451	2.8982	2.9452	2.9876	3.0265	3.0626	3.0963	3.1282
	450	2.3076	2.4046	2.4802	2.5435	2.5986	2.6480	2.6931	2.7350	2.7742	2.8113	2.8466
	500	2.0334	2.1294	2.2049	2.2686	2.3246	2.3752	2.4218	2.4653	2.5063	2.5454	2.5827
	550	1.7837	1.8785	1.9534	2.0169	2.0731	2.1242	2.1715	2.2158	2.2578	2.2979	2.3364
	600	1.5549	1.6484	1.7224	1.7855	1.8414	1.8925	1.9399	1.9845	2.0269	2.0675	2.1066
	650	1.3440	1.4363	1.5094	1.5717	1.6271	1.6779	1.7251	1.7696	1.8120	1.8527	1.8920
	700	1.1487	1.2399	1.3119	1.3734	1.4282	1.4784	1.5251	1.5694	1.6115	1.6520	1.6912
	750	0.9670	1.0572	1.1282	1.1887	1.2428	1.2923	1.3385	1.3823	1.4240	1.4642	1.5030
	800	0.7972	0.8866	0.9565	1.0162	1.0694	1.1182	1.1638	1.2069	1.2482	1.2878	1.3263
	850	0.6380	0.7267	0.7957	0.8544	0.9067	0.9548	0.9996	1.0422	1.0828	1.1219	1.1598
	900	0.4882	0.5763	0.6444	0.7022	0.7537	0.8009	0.8451	0.8869	0.9269	0.9655	1.0028
	950	0.3469	0.4344	0.5017	0.5586	0.6093	0.6557	0.6992	0.7403	0.7797	0.8176	0.8543
	1000	0.2132	0.3003	0.3667	0.4228	0.4727	0.5184	0.5611	0.6015	0.6402	0.6774	0.7135
	1050	0.0864	0.1731	0.2388	0.2941	0.3431	0.3881	0.4300	0.4698	0.5078	0.5444	0.5799
	1100	−0.0342	0.0522	0.1172	0.1717	0.2200	0.2642	0.3054	0.3445	0.3818	0.4178	0.4527

REFERENCES

Adam J., Locmelis M., Afonso J. C., Rushmer T. and Fiorentini M. L. (2014) The capacity of hydrous fluids to transport and fractionate incompatible elements and metals within the Earth's mantle. *Geochem. Geophys. Geosyst.* **15**, 2241–2253.

Ammannati E., Jacob D. E., Avanzinelli R., Foley S. F. and Conticelli S. (2016) Low Ni olivine in silica-undersaturated ultrapotassic igneous rocks as evidence for carbonate metasomatism in the mantle. *Earth Planet. Sci. Lett.* **444**, 64–74.

Andersen T., O'Reilly S. Y. and Griffin W. (1984) The trapped fluid phase in upper mantle xenoliths from Victoria, Australia: implications for mantle metasomatism. *Contrib. Miner. Petrol.* **88**, 72–85.

Arcis H., Zimmerman G. and Tremaine P. (2014) Ion-pair formation in aqueous strontium chloride and strontium hydroxide solutions under hydrothermal conditions by AC conductivity measurements. *PCCP* **16**, 17688–17704.

Berman R. G. (1988) Internally-consistent thermodynamic data for minerals in the system Na_2O-K_2O-CaO-MgO-FeO-Fe_2O_3-Al_2O_3-SiO_2-TiO_2-H_2O-CO_2. *J. Petrol.* **29**, 445–522.

Becker K. H., Cemiç L. and Langer K. E. O. E. (1983) Solubility of corundum in supercritical water. *Geochim. Cosmochim. Acta* **47**, 1573–1578.

Busey R. and Mesmer R. (1977) Ionization equilibriums of silicic acid and polysilicate formation in aqueous sodium chloride solutions to 300. degree. *C. Inorganic Chemistry* **16**, 2444–2450.

Carlson R. W., Pearson D. G. and James D. E. (2005) Physical, chemical, and chronological characteristics of continental mantle. *Rev. Geophys.* **43**, 1–24.

Connolly J. A. and Galvez M. E. (2018) Electrolytic fluid speciation by Gibbs energy minimization and implications for subduction zone mass transfer. *Earth Planet. Sci. Lett.* **501**, 90–102.

Cruz M. F. and Manning C. E. (2015) Experimental determination of quartz solubility and melting in the system SiO_2-H_2O-NaCl at 15–20 kbar and 900–1,100 °C: implications for silica polymerization and the formation of supercritical fluids. *Contrib. Miner. Petrol.* **170**, 1–17.

Dasgupta R. (2013) Ingassing, storage, and outgassing of terrestrial carbon through geologic time. *Rev. Mineral. Geochem.* **75**, 183–229.

Dawson J. (1984) Contrasting types of upper mantle metasomatism?. In *Kimberlites II: the mantle and crust-mantle relationships* (ed. J. Kornprobst). Elsevier Amsterdam.

Debret B. and Sverjensky D. A. (2017) Highly oxidising fluids generated during serpentinite breakdown in subduction zones. *Nature Scientific Reports* **7**, 10351. https://doi.org/10.1038/s41598-017-09626-y.

Deng L., Liu Y., Zong K., Zhu L., Xu R., Hu Z. and Gao S. (2017) Trace element and Sr isotope records of multi-episode carbonatite metasomatism on the eastern margin of the North China Craton. *Geochem. Geophys. Geosyst.* **18**, 220–237.

Duan Z. and Zhang Z. (2006) Equation of state of the H_2O, CO_2, and H_2O–CO_2 systems up to 10 GPa and 2573.15 K: molecular dynamics simulations with ab initio potential surface. *Geochim. Cosmochim. Acta* **70**, 2311–2324.

Dvir O. and Kessel R. (2017) The effect of CO_2 on the water-saturated solidus of K-poor peridotite between 4 and 6 GPa. *Geochim. Cosmochim. Acta* **206**, 184–200.

Dvir O., Pettke T., Fumagalli P. and Kessel R. (2011) Fluids in the peridotite–water system up to 6 GPa and 800°C: new experimental constrains on dehydration reactions. *Contrib. Miner. Petrol.* **161**, 829–844.

Elazar O., Frost D., Navon O. and Kessel R. (2019) Melting of hydrous carbonated eclogite at 4–6 GPa and 900–1,200°C: implications for the generation of diamond-forming fluids. *Geochim. Cosmochim. Acta*. https://doi.org/10.1016/j.gca.2019.03.025 (in press).

Facq S., Daniel I., Montagnac G., Cardon H. and Sverjensky D. A. (2014) In situ Raman study and thermodynamic model of aqueous carbonate speciation in equilibrium with aragonite under subduction zone conditions. *Geochim. Cosmochim. Acta* **132**, 375–390.

Facq S., Daniel I., Montagnac G., Cardon H. and Sverjensky D. A. (2016) Carbon speciation in saline solutions in equilibrium with aragonite at high pressure. *Chem. Geol.* **431**, 44–53.

Frantz J., Dubessy J. and Mysen B. (1994) Ion-pairing in aqueous MgSO4 solutions along an isochore to 500 C and 11 kbar using Raman spectroscopy in conjunction with the diamond-anvil cell. *Chem. Geol.* **116**, 181–188.

Frezzotti M., Selverstone J., Sharp Z. and Compagnoni R. (2011) Carbonate dissolution during subduction revealed by diamond-bearing rocks from the Alps. *Nat. Geosci.* **4**, 703.

Frezzotti M. L. and Ferrando S. (2015) The chemical behavior of fluids released during deep subduction based on fluid inclusions. *Am. Miner.* **100**, 352–377.

Frost D. J. and McCammon C. A. (2008) The redox state of Earth's mantle. *Ann. Rev. Earth Planetary Sci.* **36**, 389–420.

Galvez M. E., Connolly J. A. and Manning C. E. (2016) Implications for metal and volatile cycles from the pH of subduction zone fluids. *Nature* **539**, 420.

Garber J. M., Maurya S., Hernandez J. A., Duncan M. S., Zeng L., Zhang H. L., Faul U., McCammon C., Montagner J. P. and Moresi L. (2018) Multidisciplinary constraints on the abundance of diamond and eclogite in the cratonic lithosphere. *Geochem. Geophys. Geosyst.* **19**, 2062–2086.

Gréau Y., Huang J.-X., Griffin W. L., Renac C., Alard O. and O'Reilly S. Y. (2011) Type I eclogites from Roberts Victor kimberlites: products of extensive mantle metasomatism. *Geochim. Cosmochim. Acta* **75**, 6927–6954.

Harte B. (1983) *Mantle peridotites and processes the kimberlites sample*. Shiva, Nantwich.

Helgeson H. C., Kirkham D. H. and Flowers G. C. (1981) Theoretical prediction of the thermodynamic behavior of aqueous electrolytes by high pressures and temperatures; IV, Calculation of activity coefficients, osmotic coefficients, and apparent molal and standard and relative partial molal properties to 600 degrees C and 5kb. *Am. J. Sci.* **281**, 1249–1516.

Hermann J., Zheng Y.-F. and Rubatto D. (2013) Deep fluids in subducted continental crust. *Elements* **9**, 281–287.

Huang F. (2017) *Evolution of aqueous fluids, hydrocarbons, and diamond formation in the upper mantle*. Department of Earth and Planetary Sciences. Johns Hopkins University, Baltimore, MD.

Huang F., Daniel I., Cardon H., Montagnac G. and Sverjensky D. A. (2017) Immiscible hydrocarbon fluids in the deep carbon cycle. *Nat. Commun.*, 8.

Hunt J. D., Kavner A., Schauble E. A., Snyder D. and Manning C. E. (2011) Polymerization of aqueous silica in H_2O–K_2O solutions at 25–200 °C and 1bar to 20 kbar. *Chem. Geol.* **283**, 161–170.

Hunt J. D. and Manning C. E. (2012) A thermodynamic model for the system near the upper critical end point based on quartz solubility experiments at 500–1100 C and 5–20 kbar. *Geochim. Cosmochim. Acta* **86**, 196–213.

Jahn S. and Schmidt C. (2010) Speciation in aqueous $MgSO_4$ fluids at high pressures and high temperatures from ab initio molec-

ular dynamics and raman spectroscopy. *J. Phys. Chem. B* **114**, 15565–15572.

Keller, T., Katz, R.F., Hirschmann, M.M., 2016. The fate of volatiles in mid-ocean ridge magmatism. arXiv preprint arXiv:1608.03841.

Kessel R., Pettke T. and Fumagalli P. (2015) Melting of metasomatized peridotite at 4–6 GPa and up to 1200° C: an experimental approach. *Contrib. Miner. Petrol.* **169**, 1–19.

Kessel R., Ulmer P., Pettke T., Schmidt M. and Thompson A. (2005) The water–basalt system at 4 to 6 GPa: phase relations and second critical endpoint in a K-free eclogite at 700 to 1400 C. *Earth Planet. Sci. Lett.* **237**, 873–892.

Li H.-Y., Zhou Z., Ryan J. G., Wei G.-J. and Xu Y.-G. (2016) Boron isotopes reveal multiple metasomatic events in the mantle beneath the eastern North China Craton. *Geochimica et Cosmochim. Acta* **194**, 77–90.

Li Y. (2017) Immiscible C-H-O fluids formed at subduction zone conditions. *Geochem. Pespect. Lett.* **3**, 12–21.

Louvel, M., Sanchez-Valle, C., Malfait, W.J., Cardon, H., Testemale, D., Hazemann, J.-L., 2014. Fluids in the crust. Constraints on the mobilization of Zr in magmatic-hydrothermal processes in subduction zones from in situ fluid-melt partitioning experiments.

Louvel M., Sanchez-Valle C., Malfait W. J., Testemale D. and Hazemann J.-L. (2013) Zr complexation in high pressure fluids and silicate melts and implications for the mobilization of HFSE in subduction zones. *Geochim. Cosmochim. Acta* **104**, 281–299.

Manning C. E. (1994) The solubility of quartz in H_2O in the lower crust and upper mantle. *Geochim. Cosmochim. Acta*, 58.

Manning C. E. (2004) The chemistry of subduction-zone fluids. *Earth Planet. Sci. Lett.* **223**, 1–16.

Manning C. E. (2007) Solubility of corundum + kyanite in H2O at 700°C and 10 kbar: evidence for Al-Si complexing at high pressure and temperature. *Geofluids* **7**, 258–269.

Manning C. E. (2013) Thermodynamic modeling of fluid-rock Interaction at mid-crustal to upper-mantle conditions. *Rev. Mineral. Geochem.* **76**, 135–164.

Manning C. E., Antignano A. and Lin H. A. (2010) Premelting polymerization of crustal and mantle fluids, as indicated by the solubility of albite + paragonite + quartz in H2O at 1 GPa and 350–620 °C. *Earth Planet. Sci. Lett.* **292**, 325–336.

Martinez I., Sanchez-Valle C., Daniel I. and Reynard B. (2004) High-pressure and high-temperature Raman spectroscopy of carbonate ions in aqueous solution. *Chem. Geol.* **207**, 47–58.

Menzies M. and Hawkesworth C. (1986) *Mantle metasomatism*. Academic Press Inc Orlando, FL, USA, United States.

Menzies M. and Murthy V. R. (1980) Mantle metasomatism as a precursor to the genesis of alkaline magmas-isotopic evidence. *Am. J. Sci* **280**, 622–638.

Mikhail S., Barry P. H. and Sverjensky D. A. (2017) The relationship between mantle pH and the deep nitrogen cycle. *Geochim. Cosmochim. Acta* **209**, 149–160.

Mikhail S. and Sverjensky D. A. (2014) Nitrogen speciation in upper mantle fluids and the origin of Earth's nitrogen-rich atmosphere. *Nat. Geosci.* **7**, 816–819.

Mysen B. O. (2010) Speciation and mixing behavior of silica-saturated aqueous fluid at high temperature and pressure. *Am. Miner.* **95**, 1807–1816.

Mysen B., Mibe K., Chou I. M. and Bassett W. (2013) Structure and equilibria among silicate species in aqueous fluids in the upper mantle: Experimental SiO_2–H_2O and MgO–SiO_2–H_2O data recorded in situ to 900 °C and 5.4 GPa. *J. Geophys. Res. Solid Earth* **118**, 6076–6085.

Mysen B. O. and Yamashita S. (2010) Speciation of reduced C-O–H volatiles in coexisting fluids and silicate melts determined in-situ to∼ 1.4 GPa and 800° C. *Geochim. Cosmochim. Acta* **74**, 4577–4588.

Newton R. C. and Manning C. E. (2000) Quartz solubility in H_2O-NaCl and H_2O-CO_2 solutions at deep crust-upper mantle pressures and temperatures: 2–15 kbar and 500–900 °C. *Geochim. Cosmochim. Acta* **64**, 2993–3005.

Newton R. C. and Manning C. E. (2002a) Experimental determination of calcite solubility in H2O-NaCl solutions at deep crust/upper mantle pressures and temperatures: Implications for metasomatic processes in shear zones. *Am. Miner.* **87**, 1401–1409.

Newton R. C. and Manning C. E. (2002b) Solubility of enstatite + forsterite in H_2O at deep crust/upper mantle conditions: 4 to 15 kbar and 700 to 900 °C. *Geochim. Cosmochim. Acta* **66**, 4165–4176.

Newton R. C. and Manning C. E. (2006) Solubilities of corundum, wollastonite and quartz in H_2O-NaCl solutions at 800 C and 10kbar: interaction of simple minerals with brines at high pressure and temperature. *Geochim. Cosmochim. Acta* **70**, 5571–5582.

Newton R. C. and Manning C. E. (2010) Role of saline fluids in deep-crustal and upper-mantle metasomatism: insights from experimental studies. *Geofluids* **10**, 58–72.

Oelkers E. H. and Helgeson H. C. (1990) Triple-ion anions and polynuclear complexing in supercritical electrolyte solutions. *Geochim. Cosmochim. Acta* **54**, 727–738.

Oelkers E. H. and Helgeson H. (1991) Calculation of activity coefficients and degrees of formation of neutral ion pairs in supercritical electrolyte solutions. *Geochim. Cosmochim. Acta* **55**, 1235–1251.

O'Reilly S. Y. and Griffin W. (1988) Mantle metasomatism beneath western Victoria, Australia: I. Metasomatic processes in Cr-diopside lherzolites. *Geochim. Cosmochim. Acta* **52**, 433–447.

O'Reilly S. Y. and Griffin W. (2013) Mantle metasomatism, Metasomatism and the chemical transformation of rock. *Springer*, 471–533.

Padrón-Navarta J. A., Lopez Sanchez-Vizcaino V., Garrido C. J. and Gómez-Pugnaire M. T. (2011) Metamorphic record of high-pressure dehydration of antigorite serpentinite to chlorite harzburgite in a subduction setting (Cerro del Almirez, Nevado-Filábride Complex, Southern Spain). *J. Petrol.* **52**, 2047–2078.

Pan D. and Galli G. A. (2016) The fate of carbon dioxide in water-rich fluids in the Earth's mantle. *Sci. Adv.* **2**, e1601278.

Pan D., Spanu L., Harrison B., Sverjensky D. A. and Galli G. (2013) Dielectric properties of water under extreme conditions and transport of carbonates in the deep Earth. *Proc. Natl. Acad. Sci.* **110**, 6646–6650.

Pearson D. G. and Wittig N. (2014) *The formation and evolution of cratonic mantle lithosphere – evidence from mantle xenoliths, treatise on geochemistry*, second ed. Elsevier, Oxford, pp. 255–292.

Pilet S., Baker M. B. and Stolper E. M. (2008) Metasomatized lithosphere and the origin of alkaline lavas. *Science* **320**, 916–919.

Plyasunov A. V. and Shock E. L. (2001) Correlation strategy for determining the parameters of the revised Helgeson-Kirkham-Flowers model for aqueous nonelectrolytes. *Geochim. Cosmochim. Acta* **65**, 3879–3900.

Regier M. E., Mišković A., Ickert R. B., Pearson D. G., Stachel T., Stern R. A. and Kopylova M. (2018) An oxygen isotope test for the origin of Archean mantle roots. *Geochem. Perspect. Lett.* **9**, 6–10.

Salvi S., Pokrovski G. S. and Schott J. (1998) Experimental investigation of aluminum-silica aqueous complexing at 300 C. *Chem. Geol.* **151**, 51–67.

Santschi P. H. and Schindler P. W. (1974) Complex formation in the ternary systems Ca^{II}–H_4 SiO_4–H_2O and Mg^{II}–H_4SiO_4–H_2O. *J. Chem. Soc., Dalton Trans.*, 181–184.

Schmidt C. (2014) Raman spectroscopic determination of carbon speciation and quartz solubility in H_2O+Na_2CO_3 and H_2O +$NaHCO_3$ fluids to 600°C and 1.53 GPa. *Geochim. Cosmochim. Acta*.

Schmidt C. and Manning C. E. (2017) Pressure-induced ion pairing in $MgSO_4$ solutions: Implications for the oceans of icy worlds. *Geochem. Perspect. Lett.* **3**, 66–74.

Seward T. (1974) Determination of the first ionization constant of silicic acid from quartz solubility in borate buffer solutions to 350 C. *Geochim. Cosmochim. Acta* **38**, 1651–1664.

Shirey S. B., Cartigny P., Frost D. J., Keshav S., Nestola F., Nimis P., Pearson D. G., Sobolev N. V. and Walter M. J. (2013) Diamonds and the geology of mantle carbon. *Rev. Mineral. Geochem.* **75**, 355–421.

Shock E. L. and Helgeson H. C. (1988) Calculation of the thermodynamic and transport properties of aqueous species at high pressures and temperatures: Correlation algorithms for ionic species and equation of state predictions to 5 kb and 1000 C. *Geochim. Cosmochim. Acta* **52**, 2009–2036.

Shock E. L. and Helgeson H. C. (1990) Calculation of the thermodynamic and transport properties of aqueous species at high pressures and temperatures: Standard partial molal properties of organic species. *Geochim. Cosmochim. Acta* **54**, 915–945.

Shock E. L., Helgeson H. C. and Sverjensky D. A. (1989) Calculation of the thermodynamic and transport properties of aqueous species at high pressures and temperatures: Standard partial molal properties of inorganic neutral species. *Geochim. Cosmochim. Acta* **53**, 2157–2183.

Shock E. L., Oelkers E. H., Johnson J. W., Sverjensky D. A. and Helgeson H. C. (1992) Calculation of the thermodynamic properties of aqueous species at high pressures and temperatures. Effective electrostatic radii, dissociation constants and standard partial molal properties to 1000 °C and 5 kbar. *J. Chem. Soc. Faraday Trans.* **88**, 803–826.

Shock E. L., Sassani D. C., Willis M. and Sverjensky D. A. (1997) Inorganic species in geologic fluids: correlations among standard molal thermodynamic properties of aqueous ions and hydroxide complexes. *Geochim. Cosmochim. Acta* **61**, 907–950.

Simon N. S., Carlson R. W., Pearson D. G. and Davies G. R. (2007) The origin and evolution of the Kaapvaal cratonic lithospheric mantle. *J. Petrol.* **48**, 589–625.

Spiekermann G., Steele-MacInnis M., Kowalski P. M., Schmidt C. and Jahn S. (2012) Vibrational mode frequencies of H_4SiO_4, D_4SiO_4, $H_6Si_2O_7$, and $H_6Si_3O_9$ in aqueous environment, obtained from ab initio molecular dynamics. *J. Chem. Phys.* **137**, 164506–164511.

Stachel T. and Harris J. W. (2008) The origin of cratonic diamonds — Constraints from mineral inclusions. *Ore Geol. Rev.* **34**, 5–32.

Sverjensky D. A. (2019) Thermodynamic modelling of fluids from surficial to mantle conditions. *J. Geol. Soc.* **176**(2), 348–374.

Sverjensky D. A., Harrison B. and Azzolini D. (2014a) Water in the deep Earth: The dielectric constant and the solubilities of quartz and corundum to 60 kb and 1200 °C. *Geochim. Cosmochim. Acta* **129**, 125–145.

Sverjensky D. A., Hemley J. J. and Dangelo W. M. (1991) Thermodynamic assessment of hydrothermal alkali feldspar-mica-aluminosilicate equilibria. *Geochim. Cosmochim. Acta* **55**, 989–1004.

Sverjensky D. A. and Huang F. (2015) Diamond formation due to a pH drop during fluid-rock interactions. *Nat. Commun.* **6**.

Sverjensky D. A., Shock E. L. and Helgeson H. C. (1997) Prediction of the thermodynamic properties of aqueous metal complexes to 1000 °C and 5 kb. *Geochim. Cosmochim. Acta* **61**, 1359–1412.

Sverjensky D. A., Stagno V. and Huang F. (2014b) Important role for organic carbon in subduction-zone fluids in the deep carbon cycle. *Nat. Geosci.* **7**, 909–913.

Tagirov B. and Schott J. (2001) Aluminum speciation in crustal fluids revisited. *Geochim. Cosmochim. Acta* **65**, 3965–3992.

Tanger J. C. and Helgeson H. C. (1988) Calculation of the thermodynamic and transport properties of aqueous species at high pressures and temperatures; revised equations of state for the standard partial molal properties of ions and electrolytes. *Am. J. Sci.* **288**, 19–98.

Tiraboschi C., Tumiati S., Sverjensky D., Pettke T., Ulmer P. and Poli S. (2018) Experimental determination of magnesia and silica solubilities in graphite-saturated and redox-buffered high-pressure COH fluids in equilibrium with forsterite+ enstatite and magnesite+ enstatite. *Contrib. Miner. Petrol.* **173**, 2.

Tomlinson E. L., Jones A. P. and Harris J. W. (2006) Co-existing fluid and silicate inclusions in mantle diamond. *Earth Planet. Sci. Lett.* **250**, 581–595.

Tropper P. and Manning C. E. (2007) The solubility of corundum in H2O at high pressure and temperature and its implications for Al mobility in the deep crust and upper mantle. *Chemical Geology* **240**, 54–60.

Tsay A., Zajacz Z., Ulmer P., Waelle M. and Sanchez-Valle C. (2016) A new experimental approach to study fluid–rock equilibria at the slab-mantle interface based on the synthetic fluid inclusion technique. *Am. Miner.* **101**, 2199–2209.

Tsay A., Zajacz Z., Ulmer P. and Sanchez-Valle C. (2017) Mobility of major and trace elements in the eclogite-fluid system and element fluxes upon slab dehydration. *Geochim. Cosmochim. Acta* **198**, 70–91.

Tumiati S., Tiraboschi C., Pettke C., Recchia S., Ulmer P., Sverjensky D. A., Miozzi F. and Poli S. (2017) Silicate dissolution boosts the CO_2 concentrations in subduction fluids. *Nat. Commun.*, 8.

Von Damm K. (1990) Seafloor hydrothermal activity: black smoker chemistry and chimneys. *Annu. Rev. Earth Planet. Sci.* **18**, 173–204.

Wang H., van Hunen J. and Pearson D. G. (2015) The thinning of subcontinental lithosphere: The roles of plume impact and metasomatic weakening. *Geochem. Geophys. Geosyst.* **16**, 1156–1171.

Wang Z., Kusky T. M. and Capitanio F. A. (2016) Lithosphere thinning induced by slab penetration into a hydrous mantle transition zone. *Geophys. Res. Lett.*.

Watenphul A., Schmidt C. and Jahn S. (2014) Cr (III) solubility in aqueous fluids at high pressures and temperatures. *Geochim. Cosmochim. Acta* **126**, 212–227.

Weiss Y., Class C., Goldstein S. L. and Hanyu T. (2016) Key new pieces of the HIMU puzzle from olivines and diamond inclusions. *Nature* **537**, 666–670.

Weiss Y., McNeill J., Pearson D. G., Nowell G. M. and Ottley C. J. (2015) Highly saline fluids from a subducting slab as the source for fluid-rich diamonds. *Nature* **524**, 339–342.

Wissbrun K. F., French D. M. and Patterson, Jr, A. (1954) The true ionization constant of carbonic acid in aqueous solution from 5 to 45. *J. Phys. Chem.* **58**, 693–695.

Wohlers A. and Manning C. E. (2009) Solubility of corundum in aqueous KOH solutions at 700 °C and 1 GPa. *Chem. Geol.* **262**, 310–317.

Wolery T. J. (1992) *EQ3NR, a computer program for geochemical aqueous speciation-solubility calculations: theoretical manual, user's guide, and related documentation (version 7.0)*. Lawrence Livermore National Laboratory, Livermore, CA.

Zhang C. and Duan Z. (2009) A model for C-O–H fluid in the Earth's mantle. *Geochim. Cosmochim. Acta* **73**, 2089–2102.

Zotov N. and Keppler H. (2000) In-situ Raman spectra of dissolved silica species in aqueous fluids to 900 °C and 14 kbar. *Am. Miner.* **85**, 600–604.

Zotov N. and Keppler H. (2002) Silica speciation in aqueous fluids at high pressures and high temperatures. *Chem. Geol.* **184**, 71–82.

Associate editor: Wolfgang Bach